



# **IN-SITU INFRARED SPECTROSCOPIC STUDIES OF PALLADIUM THIN FILMS DURING CO<sub>2</sub> ELECTRO-REDUCTION**

Vignesh Balasubramanian

*“The earth provides enough to satisfy everybody’s need  
but not everyone’s greed”*  
**M Gandhi**

# IN-SITU INFRARED SPECTROSCOPIC STUDIES OF PALLADIUM THIN FILMS DURING CO<sub>2</sub> ELECTRO-REDUCTION

By

Vignesh Balasubramanian

in partial fulfilment of the requirements for the degree of

**Master of Science**  
in Material Science and Engineering

at the Delft University of Technology,  
to be defended publicly on Thursday October 25, 2018 at 14:00 PM.

Daily Supervisor: Dr. Recep Kas

Supervisor: Prof. Dr. Wilson Smith & Prof. Dr. Amarante Böttger

Thesis committee:

- Prof. Dr. Wilson Smith      TU Delft
- Prof. Dr. Amarante Böttger      TU Delft
- Prof. Dr. Bernard Dam      TU Delft
- Prof. Dr. Ruud Kortlever      TU Delft

## Abstract

---

An exponential growth in CO<sub>2</sub> concentration over the past few decades has led to an accelerated impact of climate change on planet earth. In a bid to curb these emissions, people across the globe are slowly transitioning towards renewable energy sources with battery technology aiding this growth. Given that battery technology is still in its nascent stage, the “Electrochemical reduction of CO<sub>2</sub>” could be a viable solution supporting it without decelerating the momentum gained towards renewable development. Although plausible, the direct reduction of CO<sub>2</sub> to liquid fuels entails huge energy expenditure thus requiring the implementation of catalysts. Unique in its ability, palladium reversibly reduces CO<sub>2</sub> to formic acid making it an interesting candidate for the reduction reaction. In addition to the production of formic acid, palladium is also known to produce carbon monoxide (CO) which completely deactivates the surface preventing further reactions from occurring.

Thus the aim of the current study is focused on analysing the electrochemical reduction of CO<sub>2</sub> on palladium thin films using surface enhanced infrared absorption spectroscopy to better understand the deactivation mechanisms of CO on the palladium thin film. The smoothness of the as-sputtered 15 nm palladium thin film with a RMS roughness of 0.511 nm and partially coalesced islands were ascertained, thus requiring surface activation to introduce the enhancement mechanism. Experimental analysis of CO<sub>2</sub> reduction on the palladium thin film was performed to unearth significant insights through the combination of electrochemical analysis techniques with surface enhanced infrared absorption spectroscopy. Results obtained through implementation of these methodologies provided substantial information not only on the influence of the palladium-hydrogen system on the electrochemical reduction of CO<sub>2</sub> but also on the impact of alkali metal cations on the palladium-hydrogen system and the CO<sub>2</sub> reduction reaction over the sputtered palladium thin film. CO formation, accumulation and desorption coupled with hydrogen evolution and desorption were some of the few avenues that were enumerated upon during the experimental investigation. The identity of CO chemisorbed on the palladium thin film along with bicarbonate direct/indirect reduction to form CO was confirmed through the utilization of N<sub>2</sub> saturated C<sup>13</sup> NaHCO<sub>3</sub> solution. In addition to the analysis of the reduction reaction, emphasis on the oxidation of CO was also provided suggesting the formation of dense CO structures with the existence of strong CO dipole – dipole coupling on the palladium surface.

# Table of Contents

---

<b>ABSTRACT</b>	<b>IV</b>
<b>TABLE OF CONTENTS</b>	<b>V</b>
<b>TABLE OF FIGURES</b>	<b>VIII</b>
<b>LIST OF TABLES</b>	<b>XII</b>
<b>NOMENCLATURE</b>	<b>XIII</b>
<b>ACKNOWLEDGEMENT</b>	<b>XIV</b>
<b>I INTRODUCTION</b>	<b>1</b>
1.1 MOTIVATION FOR THE THESIS	3
1.2 RESEARCH OBJECTIVES	4
1.3 REPORT OUTLINE	4
<b>II LITERATURE STUDY</b>	<b>5</b>
2.1 MAGNETRON SPUTTERING	5
2.2 PALLADIUM – THE METAL	8
2.3 CO ADSORPTION ON PALLADIUM	11
2.4 CO <sub>2</sub> REDUCTION REACTION ON THE PALLADIUM THIN FILM	13
2.5 SURFACE ENHANCED INFRARED ABSORPTION SPECTROSCOPY	19

<b>III MATERIALS AND METHODOLOGY</b>	<b>26</b>
3.1 CLEANING THE CELL	26
3.2 PALLADIUM THIN FILM PREPARATION AND CHARACTERIZATION	27
3.2.1 <i>Thin film Preparation</i>	27
3.2.2 <i>Electrochemical Surface area characterization</i>	28
3.2.3 <i>Atomic Force Microscopy</i>	29
3.3 ELECTROCHEMICAL AND IN-SITU SURFACE ENHANCED INFRARED ABSORPTION SPECTROSCOPY	30
3.3.1 <i>Reduction of CO<sub>2</sub> on a palladium thin film under 0.1M KHCO<sub>3</sub></i>	32
3.3.2 <i>Cationic effect on the palladium thin film affecting the CO<sub>2</sub> reduction reaction</i>	33
3.3.3 <i>Identification of the CO formation on the palladium surface</i>	34
<b>IV RESULTS</b>	<b>35</b>
4.1 PALLADIUM THIN FILM CHARACTERIZATION	35
4.1.1 <i>Electrochemical Surface area characterization</i>	35
4.1.2 <i>Atomic Force Microscopy</i>	37
4.1 REDUCTION OF CO <sub>2</sub> ON THE PALLADIUM THIN FILM UNDER 0.1M KHCO <sub>3</sub>	38
4.2 CATIONIC EFFECT ON THE PALLADIUM THIN FILM AFFECTING THE CO <sub>2</sub> REDUCTION REACTION	56

# In-Situ Infrared Spectroscopic Studies Of Palladium Thin films during CO<sub>2</sub> Electro-Reduction

---

4.3	IDENTIFICATION OF CO FORMED ON THE PALLADIUM SURFACE -----	64
<b>V</b>	<b>DISCUSSION-----</b>	<b>68</b>
5.1	PALLADIUM THIN FILM -----	68
5.2	ELECTROCHEMICAL REDUCTION OF CO <sub>2</sub> UNDER 0.1M POTASSIUM BICARBONATE -	69
5.3	CATIONIC EFFECT ON THE PALLADIUM THIN FILM AFFECTING THE CO <sub>2</sub> REDUCTION REACTION -----	76
5.4	IDENTIFICATION OF CO FORMED ON THE PALLADIUM SURFACE -----	80
<b>VI</b>	<b>CONCLUSION AND FUTURE RECOMMENDATIONS -----</b>	<b>81</b>
6.1	CONCLUSION -----	81
6.2	FUTURE RECOMMENDATIONS -----	83
<b>VII</b>	<b>BIBLIOGRAPHY -----</b>	<b>85</b>
<b>APPENDIX</b>	<b>-----</b>	<b>90</b>



## Table of Figures

---

FIGURE 1. 1- TIMELINE DEPICTING THE VARIATIONS OBSERVED IN THE ATMOSPHERIC CO <sub>2</sub> LEVELS [1] -----	1
FIGURE 1. 2- (A) DIAGRAMMATIC REPRESENTATION OF A POTENTIALLY VIABLE CO <sub>2</sub> LIFE CYCLE [9] (B) SCHEMATIC ILLUSTRATION OF THE ACTIVATION ENERGY FOR A PARTICULAR REACTION IN THE PRESENCE AND ABSENCE OF A CATALYST [10] -----	2
FIGURE 1.3- (A) SCHEMATIC DIAGRAM OF THE ELECTROCHEMICAL REDUCTION REACTION OF CO <sub>2</sub> INTO FUELS [11] AND (B) PALLADIUM CUBE [12]-----	3
FIGURE 2. 1 - SCHEMATIC REPRESENTATION OF THE MAGNETRON SPUTTERING PROCESS [18] -----	5
FIGURE 2. 2- DIAGRAMMATIC REPRESENTATION OF THORNTON’S STRUCTURAL ZONE MODEL FOR THIN FILM MATERIALS BY SPUTTER DEPOSITION [21] -----	7
FIGURE 2. 3- (A) A CYCLIC VOLTAMMOGRAM COMPARING THE ELECTROCHEMICAL BEHAVIOR OF A PALLADIUM WIRE AND PALLADIUM THIN FILM IN A 0.5M H <sub>2</sub> SO <sup>4</sup> SOLUTION [24] AND (B) CYCLIC VOLTAMMOGRAM DEPICTING THE EFFECT OF THICKNESS ON THE ELECTROCHEMICAL BEHAVIOR OF PALLADIUM [25]-----	8
FIGURE 2. 4 - (A) ILLUSTRATION OF THE FCC CRYSTAL STRUCTURE OF PALLADIUM [30] AND (B) PHASE DIAGRAM OF THE PALLADIUM-HYDROGEN SYSTEM [31] -----	10
FIGURE 2. 5 - SCHEMATIC REPRESENTATIONS OF CO ON PALLADIUM AT THE (A) A-TOP SITE, (B) BRIDGE SITE AND (C) HOLLOW SITE -----	11
FIGURE 2. 6– THE DIFFERENT SITES AVAILABLE ON Pd(210) SURFACE [35]-----	12
FIGURE 2. 7 - STANDARD REDOX POTENTIALS FOR THE VARIOUS CO <sub>2</sub> BY PRODUCTS [41] -	14
FIGURE 2. 8 - OVERVIEW OF THE FARADIC EFFICIENCIES OBTAINED FOR (A) CO AND (B) FORMATE OVER A NUMBER OF COMMONLY STUDIED CATALYSTS [15] -----	15
FIGURE 2. 9 - (A) SCHEMATIC DIAGRAM DEPICTING THE VARIOUS VIBRATIONAL MOTIONS [53] AND (B) SCHEMATIC DESCRIPTION OF AN FTIR SPECTROMETER [54] -----	19
FIGURE 2. 10 - DIAGRAMMATIC REPRESENTATION OF THE (A) SEIRAS PROCESS AND (B) PERPENDICULAR DIPOLE MOMENT BEING ENHANCED WHILE THE PARALLEL DIPOLE MOMENT GETS CANCELLED BY ITS MIRROR IMAGE [56]-----	21
FIGURE 3. 1 - (A) DIGRAMATIC REPRESENTATION OF THE ELECTROCHEMICAL-IR CELL AND (B) THE VARIOUS COMPONENTS OF THE ELECTROCHEMICAL-IR CELL -----	27
FIGURE 3. 2- MAGNETRON SPUTTERING SYSTEM UTILIZED FOR THE DEPOSITION OF PALLADIUM ON THE SILICON IRE [63] -----	28
FIGURE 3. 3– EXAMPLE OF A PALLADIUM OXIDE REDUCTION PEAK USED FOR SURFACE AREA DETERMINATION [64]-----	28
FIGURE 3. 4 - (A) BRUKER ATOMIC FORCE MICROSCOPIC SETUP AND (B) SCHEMATIC REPRESENTATION OF THE ATOMIC FORCE MICROSCOPE IN CONTACT MODE [65] -----	29
FIGURE 3. 5 - (A) BRUKER VERTEX 70 IR SPECTROMETER WITH THE SEIRA SPECTROSCOPIC CELL AND (B) A CLOSE-UP OF THE FULLY FUNCTIONAL SETUP-----	31



# In-Situ Infrared Spectroscopic Studies Of Palladium Thin films during CO<sub>2</sub> Electro-Reduction

FIGURE 4. 1 – (A) CYCLIC VOLTAMMOGRAM OF THE ACTIVATED PALLADIUM THIN FILM BETWEEN 0.35 V AND 1.4 V IN CO <sub>2</sub> SATURATED 0.1M KHCO <sub>3</sub> SOLUTION AND (B) OXIDE REDUCTION PEAK BETWEEN 0.35 V AND 1.0 V AS OBSERVED IN (A) HIGHLIGHTED FOR SURFACE AREA CALCULATIONS -----	36
FIGURE 4. 2 - AFM IMAGES OF THE 15NM AS-SPUTTERED PALLADIUM THIN FILM IN (A) 2-D AND (B) 3-D OVER 500×500 NM-----	37
FIGURE 4. 3 - AFM IMAGES OF THE 15NM AS-SPUTTERED PALLADIUM THIN FILM IN (A) 2-D AND (B) 3-D OVER 100×100 NM-----	37
FIGURE 4. 4 - SURFACE PROFILE OF THE AS-SPUTTERED PALLADIUM THIN FILM FROM ALONG THE WHITE LINE DEFINED ON THE 500NM × 500NM AFM IMAGE -----	38
FIGURE 4. 5 - SURFACE PROFILE OF THE AS-SPUTTERED PALLADIUM THIN FILM FROM ALONG THE WHITE LINE DEFINED ON THE 100NM × 100NM AFM IMAGE -----	38
FIGURE 4. 6 - IR SPECTRA RECORDED BETWEEN 1000 CM <sup>-1</sup> AND 3000 CM <sup>-1</sup> AT -0.8 V FOR CO <sub>2</sub> SATURATED 0.1M KHCO <sub>3</sub> SOLUTION ON THE 15 NM PALLADIUM THIN FILM (A) BEFORE BASELINE CORRECTION AND (B) AFTER BASELINE CORRECTION ALONG WITH AN INSET BETWEEN 1800 CM <sup>-1</sup> AND 2400 CM <sup>-1</sup> -----	39
FIGURE 4. 7 – (A) DYNAMIC CA STUDY BETWEEN 0V AND -0.8V UNDER CO <sub>2</sub> WITH A HOLD TIME OF 10 SEC AT EACH POTENTIAL (1) CURRENT DENSITY VS. E <sub>RHE</sub> (V), (2) IR SPECTRA PLOTTED BETWEEN 0V AND -0.8V FROM 1800 CM <sup>-1</sup> AND 2300 CM <sup>-1</sup> WITH A LEAST COUNT OF 0.1V AND (3) WAVENUMBER (CM <sup>-1</sup> ) VS. E <sub>RHE</sub> (V) AND (B) DESORPTION PROFILE FOR THE DYNAMIC CA STUDY AT 1.2V (1) CURRENT DENSITY VS. TIME(SEC), (2) IR SPECTRA PLOTTED BETWEEN 0 AND 50 FROM 1800 CM <sup>-1</sup> AND 2300 CM <sup>-1</sup> WITH A LEAST COUNT OF 5 AND (3) WAVENUMBER (CM <sup>-1</sup> ) VS. TIME (SEC) -----	41
FIGURE 4. 8 - IR SPECTRA RECORDED DURING N <sub>2</sub> BUBBLING OF THE CO <sub>2</sub> SATURATED 0.1M KHCO <sub>3</sub> SOLUTION FOR 5 MIN AFTER THE DYNAMIC CA STUDY RECORDED BETWEEN 1 AND 301 FROM 1800 CM <sup>-1</sup> AND 2300 CM <sup>-1</sup> WITH A LEAST COUNT OF 150 -----	42
FIGURE 4. 9 – (A) -0.3 V CA STUDY UNDER CO <sub>2</sub> FOR A PERIOD OF 5 MIN (1) CURRENT DENSITY VS. TIME (SEC), (2) IR SPECTRA PLOTTED BETWEEN 0.462 AND 46.2 SEC FROM 1800 CM <sup>-1</sup> AND 2300 CM <sup>-1</sup> , (3) IR SPECTRA PLOTTED BETWEEN 0.462 AND 300 SEC FROM 1800 CM <sup>-1</sup> AND 2300 CM <sup>-1</sup> AND (4) WAVENUMBER (CM <sup>-1</sup> ) VS. TIME (SEC) AND (B) DESORPTION PROFILE FOR THE -0.3 V CA STUDY AT 1.2V (1) CURRENT DENSITY VS. TIME(SEC) AND (2) IR SPECTRA PLOTTED BETWEEN 0.462 AND 4.62 FROM 1800 CM <sup>-1</sup> AND 2300 CM <sup>-1</sup> -----	43
FIGURE 4. 10 - (A) -0.5 V CA STUDY UNDER CO <sub>2</sub> FOR A PERIOD OF 5 MIN (1) CURRENT DENSITY VS. TIME (SEC), (2) IR SPECTRA PLOTTED BETWEEN 0.462 AND 300 SEC FROM 1800 CM <sup>-1</sup> AND 2300 CM <sup>-1</sup> AND (3) WAVENUMBER (CM <sup>-1</sup> ) VS. TIME (SEC) AND (B) DESORPTION PROFILE FOR THE -0.5 V CA STUDY AT 1.2V (1) CURRENT DENSITY VS. TIME (SEC), (2) IR SPECTRA PLOTTED BETWEEN 0.462 AND 6 SEC FROM 1800 CM <sup>-1</sup> AND 2300 CM <sup>-1</sup> AND (3) WAVENUMBER(CM <sup>-1</sup> ) VS. TIME (SEC)-----	44
FIGURE 4. 11 - (A) 10 MVPERS CV STUDY UNDER CO <sub>2</sub> BETWEEN -0.8 V AND 1.2 V WITH 0 V AS THE MID-POINT (1) CURRENT DENSITY VS. E <sub>RHE</sub> (V), (2) IR SPECTRA PLOTTED FROM 0 V TO -0.8 V TO 0V FROM 1800 CM <sup>-1</sup> AND 2300 CM <sup>-1</sup> WITH A LEAST COUNT OF 0.1 V AND (3) IR SPECTRA PLOTTED FROM -0.2 V TO 1.2 V TO 1.1 V FROM 1800 CM <sup>-1</sup> AND 2300 CM <sup>-1</sup> WITH A LEAST COUNT OF 0.1 V AND (B)WAVENUMBER(CM <sup>-1</sup> ) VS. E <sub>RHE</sub> FOR THE 10 MVPERS CV STUDY (1) -0.2 V TO -0.8 V, (2) -0.8 V TO 0 V AND (3) -0.2 V TO 1.0 V-----	46
FIGURE 4. 12 - (A) 2 MVPERS CV STUDY UNDER CO <sub>2</sub> BETWEEN -0.8 V AND 1.2 V WITH 0 V AS THE MID-POINT (1) CURRENT DENSITY VS. E <sub>RHE</sub> (V), (2) IR SPECTRA PLOTTED FROM 0 V TO -0.8 V TO 0 V FROM 1800 CM <sup>-1</sup> AND 2300 CM <sup>-1</sup> WITH A LEAST COUNT OF 0.1 V	

## In-Situ Infrared Spectroscopic Studies Of Palladium Thin films during CO<sub>2</sub> Electro-Reduction

- AND (3) IR SPECTRA PLOTTED FROM -0.2 V TO 1.2 V TO 1.1 V FROM 1800  $\text{cm}^{-1}$  AND 2300  $\text{cm}^{-1}$  WITH A LEAST COUNT OF 0.1 V AND (B) WAVENUMBER ( $\text{cm}^{-1}$ ) VS.  $E_{\text{RHE}}$  FOR THE 2 MVPERS CV STUDY (1) -0.2 V TO -0.8 V, (2) -0.8 V TO 0 V AND (3) -0.2 V TO 1.0 V-----48
- FIGURE 4. 13 - (A) DYNAMIC CA STUDY UNDER  $\text{N}_2$  BETWEEN 0 V AND -0.8 V WITH A HOLD TIME OF 10 SEC AT EACH POTENTIAL (1) CURRENT DENSITY VS.  $E_{\text{RHE}}$  (V) AND (2) IR SPECTRA PLOTTED BETWEEN 0 V AND -0.8 V FROM 1800  $\text{cm}^{-1}$  AND 2300  $\text{cm}^{-1}$  WITH A LEAST COUNT OF 0.1 V AND (B) -0.3 V CA STUDY UNDER  $\text{N}_2$  FOR A PERIOD OF 5 MIN (1) CURRENT DENSITY VS. TIME (SEC) AND (2) IR SPECTRA PLOTTED BETWEEN 0.462 SEC AND 300 SEC FROM 1800  $\text{cm}^{-1}$  AND 2300  $\text{cm}^{-1}$  -----49
- FIGURE 4. 14 -0.5V CA STUDY UNDER  $\text{N}_2$  FOR A PERIOD OF 5 MIN (1) CURRENT DENSITY VS. TIME (SEC) AND (2) IR SPECTRA PLOTTED BETWEEN 0.462 AND 300 SEC FROM 1800  $\text{cm}^{-1}$  AND 2300  $\text{cm}^{-1}$ -----50
- FIGURE 4. 15 - (A) 10 MVPERS CV STUDY UNDER  $\text{N}_2$  BETWEEN -0.8 V AND 1.2 V WITH 0 V AS THE MID-POINT (1) CURRENT DENSITY VS.  $E_{\text{RHE}}$  (V), (2) IR SPECTRA PLOTTED FROM 0 V TO -0.8 V TO 0 V FROM 1800  $\text{cm}^{-1}$  AND 2300  $\text{cm}^{-1}$  WITH A LEAST COUNT OF 0.1 V AND (3) IR SPECTRA PLOTTED FROM -0.2 V TO 1.2 V TO 1.1 V FROM 1800  $\text{cm}^{-1}$  AND 2300  $\text{cm}^{-1}$  WITH A LEAST COUNT OF 0.1 V AND (B) WAVENUMBER ( $\text{cm}^{-1}$ ) VS.  $E_{\text{RHE}}$  (V) FOR THE 10 MVPERS CV STUDY UNDER  $\text{N}_2$  (1) -0.7 V TO 0 V, (2) -0.2 V TO 1.1 V ----51
- FIGURE 4. 16 - (A) 2 MVPERS CV STUDY UNDER  $\text{N}_2$  BETWEEN -0.8 V AND 1.2 V WITH 0 V AS THE MID-POINT (1) CURRENT DENSITY VS.  $E_{\text{RHE}}$  (V), (2) IR SPECTRA PLOTTED FROM 0 V TO -0.8 V TO 0 V FROM 1800  $\text{cm}^{-1}$  AND 2300  $\text{cm}^{-1}$  WITH A LEAST COUNT OF 0.1 V AND (3) IR SPECTRA PLOTTED FROM -0.2 V TO 1.2 V TO 1.1 V FROM 1800  $\text{cm}^{-1}$  AND 2300  $\text{cm}^{-1}$  WITH A LEAST COUNT OF 0.1 V AND (B) WAVENUMBER ( $\text{cm}^{-1}$ ) VS.  $E_{\text{RHE}}$  (V) FOR THE 2 MVPERS CV STUDY UNDER  $\text{N}_2$  (1) -0.2 V TO -0.8 V, (2) -0.8 V TO 0 V AND (3) -0.2 V TO 1.0 V-----53
- FIGURE 4. 17 - (A) CURRENT DENSITY VS. TIME (SEC) FOR THE 5 MIN REDUCTION STUDY AT -0.8 V AND 5 MIN DESORPTION STUDY AT 0.8 V, 0.9 V, 1.0 V, 1.1 V AND 1.2 V AND (B) IR SPECTRA RECORDED DURING THE 5 MIN REDUCTION STUDY AT -0.8 V AND THE DESORPTION STUDY UNTIL THE END OF THE 5<sup>TH</sup> MIN OR THE COMPLETE OXIDATION OF CO AT 0.8 V, 0.9 V, 1.0 V, 1.1 V AND 1.2 V.-----55
- FIGURE 4. 18 – WAVENUMBER ( $\text{cm}^{-1}$ ) VS. TIME (SEC) FOR THE 5 MIN REDUCTION STUDY AT (1) 0.8 V AND THE 5 MIN DESORPTION STUDY AT (2) 0.8 V, (3) 0.9 V, (4) 1.0 V, (5) 1.1 V AND (6) 1.2 V -----56
- FIGURE 4. 19- DYNAMIC CA STUDY UNDER  $\text{CO}_2$  BETWEEN 0 V AND -0.8 V WITH A HOLD TIME OF 10 SEC AT EACH POTENTIAL CONDUCTED UNDER 0.1M BICARBONATE SOLUTION WITH LITHIUM, SODIUM, POTASSIUM AND CESIUM AS THE CATION (1) CURRENT DENSITY VS.  $E_{\text{RHE}}$  (V) AND (2) WAVENUMBER ( $\text{cm}^{-1}$ ) VS.  $E_{\text{RHE}}$  (V) AND (B) IR SPECTRA PLOTTED BETWEEN 0 V AND -0.8 V FROM 1800  $\text{cm}^{-1}$  AND 2300  $\text{cm}^{-1}$  WITH A LEAST COUNT OF 0.1 V UNDER LITHIUM, SODIUM, POTASSIUM AND CESIUM.-----57
- FIGURE 4. 20 - DESORPTION PROFILE FOR THE DYNAMIC CA STUDY AT 1.2V UNDER  $\text{CO}_2$  FOR LITHIUM, SODIUM, POTASSIUM AND CESIUM (1) CURRENT DENSITY VS. TIME (SEC) AND (2) WAVENUMBER ( $\text{cm}^{-1}$ ) VS. TIME (SEC)-----58
- FIGURE 4. 21 - (A) -0.3 V CA STUDY CONDUCTED FOR LITHIUM, SODIUM, POTASSIUM AND CESIUM UNDER  $\text{CO}_2$  FOR A PERIOD OF 5 MIN (1) CURRENT DENSITY VS. TIME (SEC) AND (4) WAVENUMBER ( $\text{cm}^{-1}$ ) VS. TIME (SEC) AND (B) DESORPTION PROFILE FOR THE -0.3 V CA STUDY AT 1.2 V CONDUCTED FOR LITHIUM, POTASSIUM AND CESIUM (1) CURRENT DENSITY VS. TIME (SEC) AND (2) WAVENUMBER ( $\text{cm}^{-1}$ ) VS. TIME (SEC) ---60

- FIGURE 4. 22 - (A) -0.5 V CA STUDY CONDUCTED FOR LITHIUM, SODIUM, POTASSIUM AND CESIUM UNDER CO<sub>2</sub> FOR A PERIOD OF 5 MIN (1) CURRENT DENSITY VS. TIME (SEC) AND (4) WAVENUMBER (CM<sup>-1</sup>) VS. TIME (SEC) AND (B) DESORPTION PROFILE FOR THE -0.5 V CA STUDY AT 1.2 V CONDUCTED FOR LITHIUM, POTASSIUM AND CESIUM (1) CURRENT DENSITY VS. TIME (SEC) AND (2) WAVENUMBER (CM<sup>-1</sup>) VS. TIME (SEC) ---61
- FIGURE 4. 23 - (A) 10 mVPERS CV STUDY PERFORMED UNDER CO<sub>2</sub> FOR LITHIUM, SODIUM, POTASSIUM AND CESIUM (1) CURRENT DENSITY VS. E<sub>RHE</sub>(V), AND WAVENUMBER (CM<sup>-1</sup>) VS. E<sub>RHE</sub>(V) BETWEEN (2) -0.2/-0.3/-0.5 V AND -0.8 V, (3) -0.8 V AND 0 V AND (4) -0.2 V AND 0.8/1.0/1.1 V AND (B) 2 mVPERS CV STUDY PERFORMED UNDER CO<sub>2</sub> FOR LITHIUM, SODIUM, POTASSIUM AND CESIUM (1) CURRENT DENSITY VS. E<sub>RHE</sub>(V), AND WAVENUMBER (CM<sup>-1</sup>) VS. E<sub>RHE</sub>(V) BETWEEN (2) -0.3/-0.4 V AND -0.8 V, (3) -0.8 V AND 0 V AND (4) -0.2 V AND 0.9/1.0 V-----63
- FIGURE 4. 24 - (A) 2 mVPERS CV STUDY PERFORMED UNDER CO<sub>2</sub> SATURATED 0.1 M NAHC<sup>13</sup>O<sub>3</sub> (1) CURRENT DENSITY VS. E<sub>RHE</sub>(V), (2) IR SPECTRA PLOTTED FROM 0 V TO -0.8 V BACK TO 0 V WITH A LEAST COUNT OF 0.1 V AND WAVENUMBER (CM<sup>-1</sup>) VS. E<sub>RHE</sub>(V) BETWEEN (3) -0.3 V/-0.4 V AND -0.8 V AND (4) -0.8 V AND 0V (B) ) 2 mVPERS CV STUDY PERFORMED UNDER CO<sub>2</sub> SATURATED 0.1M NAHCO<sub>3</sub> (1) CURRENT DENSITY VS. E<sub>RHE</sub>(V), (2) IR SPECTRA PLOTTED FROM 0 V TO -0.8 V BACK TO 0 V WITH A LEAST COUNT OF 0.1 V AND WAVENUMBER (CM<sup>-1</sup>) VS. E<sub>RHE</sub>(V) BETWEEN (3) -0.3 V/-0.4 V AND -0.8 V AND (4) -0.8 V AND 0 V-----65
- FIGURE 4. 25 - IR SPECTRA RECORDED DURING CO<sub>2</sub> BUBBLING OF THE N<sub>2</sub> SATURATED 0.1M NAHC<sup>13</sup>O<sub>3</sub> SOLUTION FOR A PERIOD OF 5 MIN AFTER THE 2 mVPERS CV STUDY RECORDED BETWEEN 1800 CM<sup>-1</sup> AND 2300 CM<sup>-1</sup> -----66

- FIGURE 5. 1 – STEPS DEPICTING THE CO<sub>2</sub> REDUCTION MECHANISM ON THE 15 NM PALLADIUM THIN FILM (1) REDUCTION OF H<sub>2</sub>O TO ADSORB HYDROGEN, (2) H COMPLETELY ADSORBED AND ABSORBED TO FORM B-PdH<sub>x</sub>, (3) EVOLUTION OF H GIVING RISE TO LOW H SURFACE COVERAGE AND B-PdH<sub>x</sub>@Pd, (4) THE ADSORPTION AND REDUCTION OF CO<sub>2</sub> TO FORM COOH<sup>\*</sup>, (5) SIMULTANEOUS PROTON AND ELECTRON TRANSFER TOWARDS THE COOH<sup>\*</sup> AND (6) FORMATION OF CO WITH H<sub>2</sub>O AS THE BY-PRODUCT-----70
- FIGURE 5. 2- CV STUDY CONDUCTED AT (A) 10 mVPERS AND (B) 2 mVPERS UNDER THE CO<sub>2</sub> SATURATED 0.1M KHCO<sub>3</sub>-----72
- FIGURE 5. 3- CO OXIDATION REGIME FOR THE 4 ALKALI ION ELECTROLYTES UNDER THE 10 mVPERS AND 2 mVPERS CV STUDY -----79




## List of Tables

---

TABLE 2. 1- DIFFERENT TYPES OF ATR CRYSTALS AVAILABLE FOR INFRARED SPECTROSCOPIC STUDIES [56] -----	22
TABLE 2. 2- LITERATURE VALUES FOR IR SPECTRA'S OF SPECIES THAT WOULD BE OBSERVED DURING THE SEIRA SPECTROSCOPIC STUDY -----	25
TABLE 3. 1- INFORMATION REGARDING THE ELECTROLYTES IMPLEMENTED DURING THE STUDY -----	32
TABLE 4. 1- SLOPE CALCULATED FOR THE PEAK CENTER SHIFT ACROSS THE 4 REGIONS IDENTIFIED IN THE WAVENUMBER (CM <sup>-1</sup> ) VS. E <sub>RHE</sub> (V) PLOT FOR LITHIUM, SODIUM, POTASSIUM AND CESIUM -----	64

## Nomenclature

---

- 1 a – Lattice Parameter
- 2 c – Speed of Light
- 3 CO<sub>2</sub> – Carbon Dioxide
- 4 CO – Carbon Monoxide
- 5 COOH – Formate
- 6 CO<sub>3</sub><sup>-</sup> - Carbonate ion
- 7 d - Diameter
- 8 DC – Direct Current
- 9 HCO<sub>3</sub><sup>-</sup> - Bicarbonate ion
- 10 H<sub>2</sub>CO<sub>3</sub> – Carbonic Acid
- 11 H - Hydrogen
- 12 HCOO - Carboxyl
- 13 K – Spring Constant
- 14 m - mass
- 15 N<sub>2</sub> – Nitrogen
- 16 q – Charge of One Electron =  $1.602 \times 10^{-19}$  C
- 17 RF – Radio Frequency
- 18  $\Pi$  – Pi
- 19  $\mu$  - Reduced Mass
- 20  $\nu$  – Wavenumber
- 21  - Start
- 22  - Continue
- 23  - Finish
- 24 \* - active site on the catalyst

## Acknowledgement

---

As I near the end of my 2 year remarkable and challenging voyage at the “*Technische Universiteit Delft*”, there a few people I would like to thank for being a constant source of support and encouragement. I would like to begin by thanking my 3 pillars of strength, **my parents and elder sister**, without whom I wouldn't have survived the tough moments in this beautiful country. All that I have achieved, not only over these 2 years, is due to their love and support, for which I am ever so grateful.

I would like to express my deep gratitude to my daily supervisor/ friend **Dr. Recep Kas** for not only his valuable suggestions and insights during the research work, but also for his brilliant sense of humour; making these 8 months a truly memorable experience. I would also like to extend my gratitude to **Dr. Wilson Smith** and **Dr. Amarante Bottger** for their valuable and constructive suggestions during the planning and development stages of the master thesis. I would also like to thank **Hugo** and all the members of the **MECS GROUP** for their support and amazing taste in music; making every moment in that lab a joyous one.

Finally, I would like to thank **Anjana, Prasath, Siddarth, Srinivasan, Vineet ,Vishal** and **all my close friends** in Delft, India and the United States of America for standing by me through thick and thin, making these 2 years truly momentous.

October 2018  
Delft, Netherlands





# I Introduction

---

Rising sea levels, global temperature rise, glacial retreat, and unseasonal and extreme weather forecasts. These are few of the many terminologies utilized to unequivocally describe the phenomenon coined by researchers across the world as “**Climate Change**”. Climate change is considered to be a major threat to the survival of mankind since the beginning of the 21<sup>st</sup> century. The emission of greenhouse gases, a majority of it being CO<sub>2</sub>, is well documented through studies as being the primary contributor towards climate change. The alarming rise in CO<sub>2</sub> levels, from 180-300 ppm over the past 800,000 years [1] [2] to 400 ppm in 2013 with an unprecedented 145% increase in CO<sub>2</sub> levels since before the industrial revolution, has forced mankind to develop and execute strategies to drastically cut down on CO<sub>2</sub> emissions and preserve mother nature for the future generations. [3] [4]

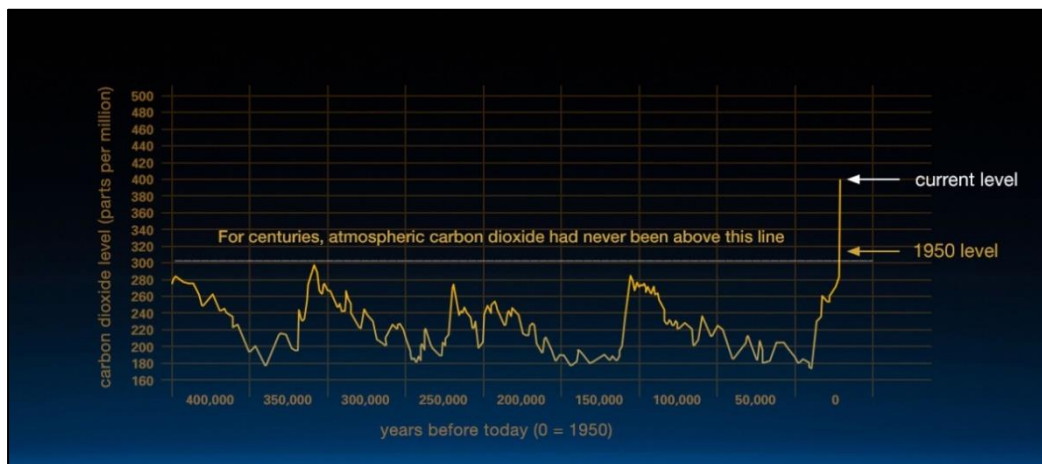


**Figure 1. 1- Timeline depicting the variations observed in the atmospheric CO<sub>2</sub> levels [1]**

One such initiative that has enabled the unification of the world to fight against climate change was the “**Paris Climate Accord**”. The Paris Climate Accord brought together representatives from across 175 countries aiming to “***Strengthen the global response to the threat of climate change by keeping a global temperature rise this century well below 2 degrees Celsius above pre-industrial levels and to pursue efforts to limit the temperature increase even further to 1.5 degrees Celsius***”. [5] Given that close to 60% of the total global greenhouse gas emissions originate from CO<sub>2</sub> emitted by the energy sector, an avenue has been created for governments, academicians and scientists to collaborate with an ultimate aim of creating innovative and green solutions for a cleaner and brighter future. [6]

Since the late 20<sup>th</sup> and early 21<sup>st</sup> century, the imminent threat of climate change has been the cornerstone for galvanizing the scientific community towards developing renewable energy solutions. This initiative is aimed at not only replacing current conventional energy sources and energy production techniques, but also towards drastically cutting down on the CO<sub>2</sub> emissions associated with those processes. Studies conducted by the “**International Renewable Energy Agency**” report a 140% growth in global renewable energy capacity as of 2017 [7], with forecasts by the “**International Energy Agency**” suggesting a 43 % global increase in capacity by 2022 [8]. This unprecedented but imperious growth in the renewable energy sector across the globe, although welcomed, has brought along a major obstacle requiring urgent scientific attention. Seasonal variations observed across the earth’s surface causes intermittent peak performances of a variety of renewable energy solutions, restricting their complete integration into the electrical grid. Therefore, a need has arisen to develop energy conversion and storage solutions to meet the yearlong energy demands of the modern world.

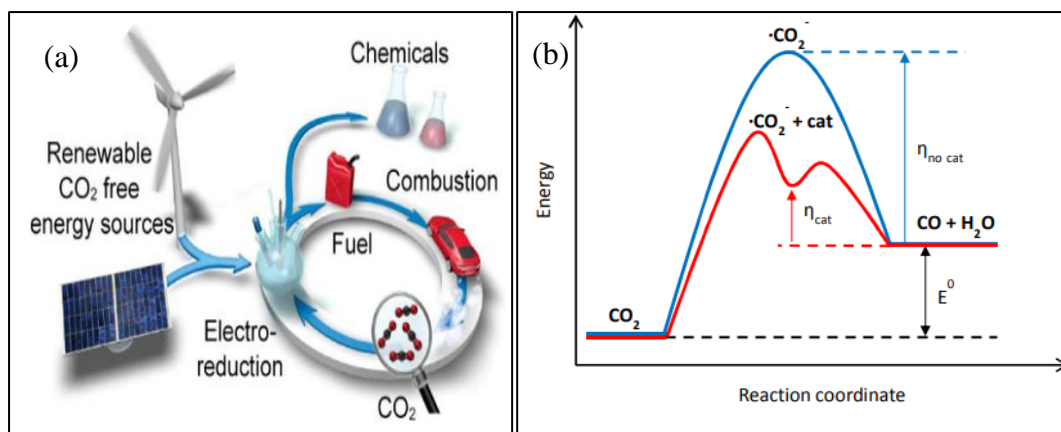
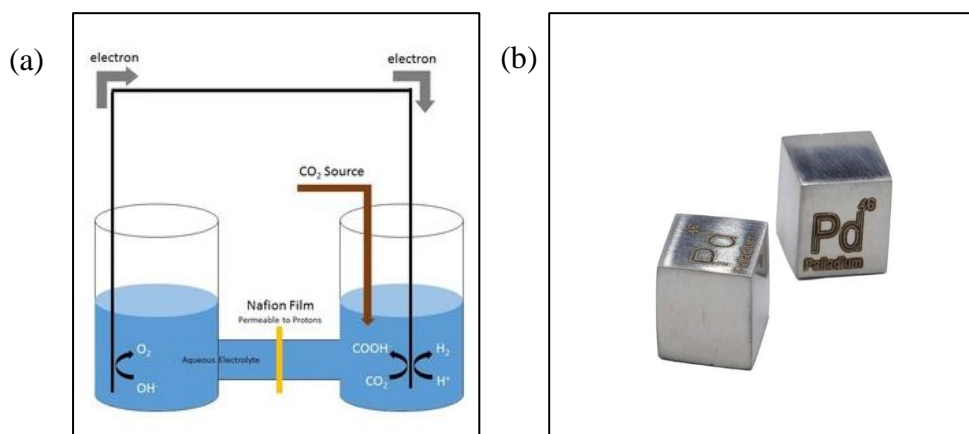


Figure 1. 2- (a) Diagrammatic representation of a potentially viable CO<sub>2</sub> life cycle [9] (b) Schematic illustration of the activation energy for a particular reaction in the presence and absence of a catalyst [10]

One such innovative solution that is creating ripples in the scientific community is the “**Electrochemical Reduction of CO<sub>2</sub>**”. Taking inspiration from mother nature, scientists have and are continuing to work on devices that enable the conversion of atmospheric CO<sub>2</sub> and excess energy into chemical products with high calorific value leading to robust storage and transportation solutions. Although advantageous, the thermodynamic stability of CO<sub>2</sub> impedes its progress requiring alternative pathways in order to create a sustainable process. The use of transition elements as catalysts was therefore introduced, improving not only the efficiency but also the selectivity of the electrochemical reduction reaction. In pursuit of identifying the ideal catalyst material, numerous publications were referred to with “**Palladium**” being chosen due to the uniqueness it embodies.

## 1.1 Motivation for the Thesis

The necessity for large scale energy conversion devices with the ability to convert CO<sub>2</sub> to liquid hydrocarbon requires the optimization of a few essential parameters in order to attain economic feasibility. The choice of catalyst is one such parameter that is of at most importance as it impacts the selectivity and efficiency of the reduction reaction.



**Figure 1.3- (a) Schematic diagram of the electrochemical reduction reaction of CO<sub>2</sub> into fuels [11] and (b) Palladium cube [12]**

Number 46 on the periodic table with an atomic weight of 106.42 AMU and density of 11.9 g/cm<sup>3</sup>, palladium plays a key role in the catalysis of industrially significant reactions spanning from petroleum cracking to ICE (Internal Combustion Engine) exhaust conversion reactions. In addition to the above mentioned areas, the face centered cubic material is currently being studied for its innate ability to catalyze the reduction of CO<sub>2</sub>. During the electrochemical reduction of CO<sub>2</sub>, palladium is known to selectively produce formic acid and carbon monoxide through the formation of HCOO<sup>-</sup> and COOH<sup>-</sup> intermediates, while simultaneously evolving hydrogen [13]. Formic acid is known to be an industrially significant chemical that is frequently used in the production of leather, rubber and energy (Direct Formic Acid Fuel Cell). In addition to the production of formic acid, the metal is also known for its unique ability to reversibly reduce formic acid thus enabling its production at low cathodic over-potentials. [14] The selectivity and reduced over potential associated with the formation of formic acid stems from palladium's unique ability to adsorb and absorb hydrogen. In addition to the formation of hydrides, numerous studies have also documented the positive effect large surface areas and high index facets have towards the formation of formic acid along with the suppression of carbon monoxide [15] [16]. Although seeming advantageous, the formation of carbon monoxide acts as a poison causing not only the inhibition of formic acid but also the complete deactivation of the palladium catalyst surface. [17] Given the application spectrum of palladium coupled with its resource criticality, one must be able to efficiently

maximize the formic acid yield during CO<sub>2</sub> reduction through the inhibition of carbon monoxide.

## 1.2 Research Objectives

Therefore with the objective set on reducing CO poisoning on the palladium surface, significant insight into the mechanisms involved during the production and accumulation of CO is necessitated. **Surface Enhanced Infrared Absorption Spectroscopy** (SEIRAS) is a unique technique that enables real time in-situ analysis of the reduction reaction occurring on the metal surface, thus providing key insights on the species involved at the electrode-electrolyte interface. SEIRAS is an innovative technique that utilizes the metal's ability to amplify IR signals generated by molecules on and within close proximity of the surface. Through its implementation, in combination with various electrochemical processes, a real opportunity is created to contribute towards the ever-growing field of carbon sequestration. Therefore based on the main objective, the following goals will be accomplished over the course of the master thesis -:

- Surface characterization of the palladium thin film
- Qualitative analysis of the CO<sub>2</sub> reduction reaction on palladium thin films under CO<sub>2</sub> and N<sub>2</sub> saturated potassium bicarbonate solution under varying potentials by using infrared spectroscopy.
- Qualitative analysis of the cationic effect on palladium thin films during the CO<sub>2</sub> reduction reaction under varying potentials by using infrared spectroscopy.
- Analysis of the CO poisoning effect on the palladium thin films along with the determination of possible solutions towards reducing its formation.

## 1.3 Report Outline

The report in totality consists of 6 chapters, which includes the introduction. Following the introduction in chapter 1, the report will dwell into the various theoretical concepts and literature's published related to the topic in chapter 2. Chapter 3 will discuss the experimental procedures employed during the study followed by presentation of the results in chapter 4. Chapter 5 will analyze the data obtained during the study with Chapter 6 presenting the concluding remarks and possible recommendations for future works.

## II Literature Study

---

An essential aspect of the study is to understand the basic principles governing the underlying phenomena associated with the reduction of CO<sub>2</sub>. Therefore the aim of the chapter is to focus on introducing the reader to basic theories and concepts that would be encountered during the study.

### 2.1 Magnetron Sputtering

Sputter deposition unlike chemical deposition is a non-equilibrium and facile process of generating thin film materials. The deposition process works on the ability to produce thin films through ion bombardment of the target metal in either an inert or reactive atmosphere. There are 2 different power sources that can be utilized for the sputter deposition process (1) DC power supply and (2) RF power supply. As DC power is frequently used for metallic targets, it will also be used for the sputter deposition process in this study. Parameters such as nature of the substrate, substrate-target distance, deposition rate, and gas pressure greatly control the morphology of the thin film generated through this process. The schematic description on the working of the magnetron sputtering system is depicted in figure 2.1.

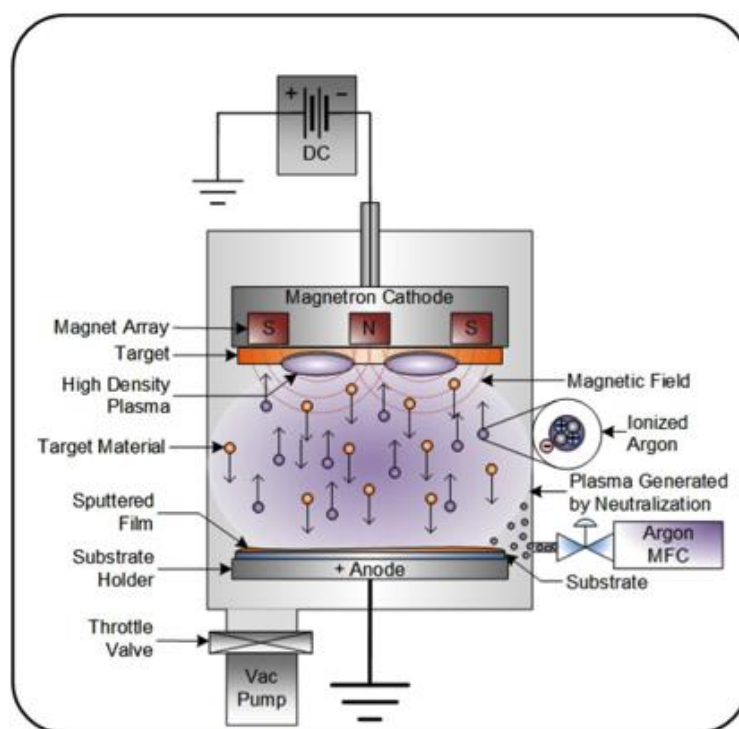


Figure 2. 1 - Schematic representation of the magnetron sputtering process [18]

A variant to the conventional sputtering setup, the base of the target consists of magnets arranged appropriately to create a closed path magnetic field on the surface side of the target. The electric field generated between the target (cathode) and the substrate (anode) will cause collisions between the electrons flowing and inert gas particles, igniting the plasma (ionized atom such as Ar<sup>+</sup>) which is essential for the sputter deposition process. As magnetron sputtering is employed, a high electron density close to the cathode is maintained enabling increased collisions and therefore lower gas pressures for ignition of the plasma. The target being cathodically charged accelerates the ionized particles towards it, dislodging particles mostly (inert) from the surface of the target through cascading collisions. The momentum gained from the inelastic collisions enable the target particles to diffuse towards and deposit on the surface of the substrate forming the thin film. During the collision between the ionized particle and the target, secondary electrons are also emitted alongside the target particles, facilitating the maintenance of the ignited plasma. In addition to the above mentioned advantages of the magnetron process, it also generates higher ion current and higher deposition rates, therefore reducing the impurity content in the deposited thin film. [18] [19] [20]

Following the brief description provided on the working principles of the magnetron sputtering technique, a short introduction on thin films produced by sputter deposition is provided to acquaint the reader to simple concepts regarding the subject.

Interest around the implementation of thin film materials is growing rapidly with the material finding applications across numerous fields, ranging from the semiconductor industry to the chemical industry. To facilitate commercial implementation of such materials, various scientific researchers and organizations have and continue to conduct intensive research to study the growth and the associated structural and functional properties of these materials. As most of the thin film properties tend to emerge from its morphology and microstructure, a better understanding of the mechanisms involved during the growth phase becomes essential. As we all know, there are 5 different kinds of stages associated with the growth of a thin film material namely:

1. Nucleation
2. Island growth
3. Island impingement
4. Island coalescence
5. Grain coarsening

Each of these stages can be affected by variations introduced in one or many of the sputtering parameters which are:



1. Substrate temperature
2. Sputtering pressure
3. Impurities
4. Deposition rate
5. Alloying elements

Out of all the parameters listed above the substrate temperature, sputter gas pressure and deposition rate tends to play a crucial role in determining the morphology and microstructure of the growing film. In the year 1974 **J.A.Thornton** postulated the structure zone model that characterizes the thin film growth patterns into 4 zones namely:

1. Zone 1
2. Zone T
3. Zone 2
4. Zone 3

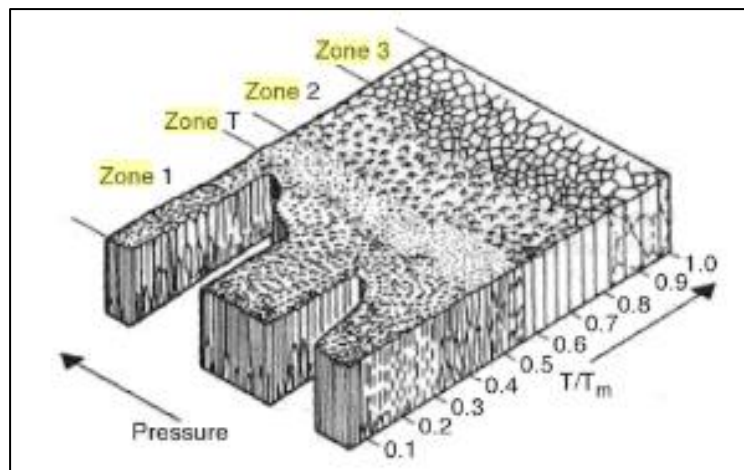


**Figure 2. 2- Diagrammatic representation of Thornton's structural zone model for thin film materials by sputter deposition [21]**

The zone 1 film growth occurs at low  $T_s/T_m$  (Substrate temperature/melting temperature) with the formation of polycrystalline or amorphous columnar structures having large defects and open boundaries. The main reason for the formation of columnar structures is the shadowing effect which is created by the lack of surface diffusion observed in this regime. Zone T which occurs at slightly higher  $T_s/T_m$  values is a transition region that includes the growth of columnar structures but eliminates the vacant regions separating the columns, thus forming a continuous densely packed but multi grain structure. The film at this stage tends to show mechanical properties similar to that of the bulk material.

As the  $T_s/T_m$  value increases, the activation energy required for surface diffusion is achieved leading to the formation of Zone 2 films that are still polycrystalline in nature.



But unlike in zone 1 and zone T, Zone 2 favors the growth of low energy grains over high energy grains but still showcases tightly packed columnar structures. Even after nucleation, only the low energy grains will survive and grow giving rise to epitaxial grains with a faceted surface. At substrate temperatures close to the melting point of the metal, bulk self-diffusion in combination with surface diffusion takes over giving rise to zone 3 films with large low energy equiaxed grains and smooth surfaces. Thornton was also able to experimentally determine the effects of the sputter gas pressure in combination with varying substrate temperatures, indicating a downward shift in the zones with increasing pressure. [22] [23] [21]

### 2.2 Palladium – The Metal

Palladium as previously stated, is a unique element with the ability to reversibly convert CO<sub>2</sub> into formic acid through the implementation of electrochemical techniques. This reversible trait that exists within the system initiates the reduction at lower potentials, thus promoting its use as a CO<sub>2</sub> reduction catalyst. Although occurring at lower potentials in comparison to commonly studied transition metals, palladium still requires external stimulus in order to activate the reduction reaction. As the study will be focused upon electrochemically examining the reduction reaction over the palladium surface, insight into its electrochemical behaviour would be beneficial towards elucidating the results recorded during the study. Figure 2.3(a) depicts a cyclic voltammogram comparing a palladium wire to a 200 nm thick palladium deposit placed in a 0.5M H<sub>2</sub>SO<sub>4</sub> solution. [24]

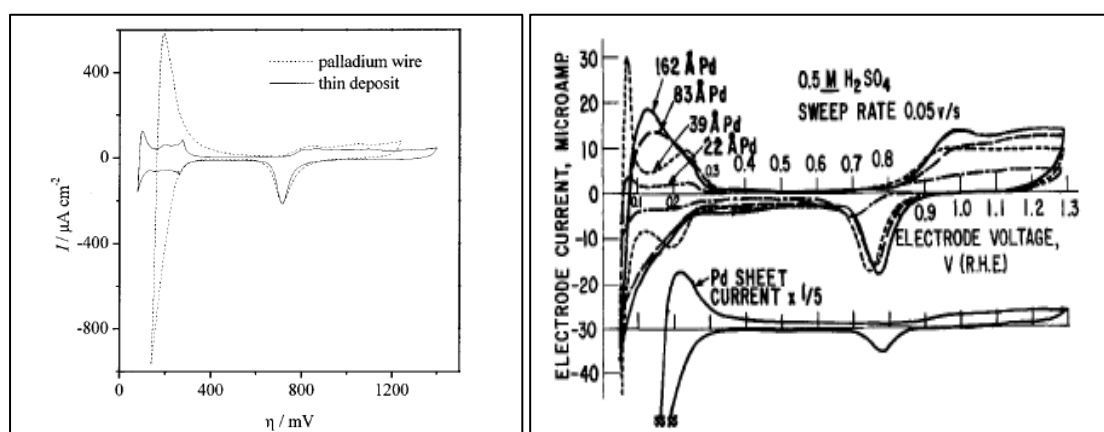
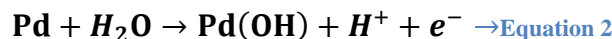
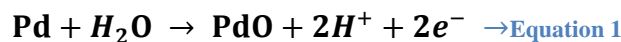


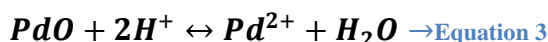
Figure 2. 3- (a) A Cyclic voltammogram comparing the electrochemical behavior of a palladium wire and palladium thin film in a 0.5M H<sub>2</sub>SO<sub>4</sub> solution [24] and (b) Cyclic voltammogram depicting the effect of thickness on the electrochemical behavior of palladium [25]

Although there exists minor differences in each of the CV's, the underlying process governing them still remains the same. As the potential moves anodically, beginning from the double layer region (0.35 V to 0.75 V), there is an increase in the current density at about 0.8 V marking the initiation of the oxidation reaction. This initiation on the

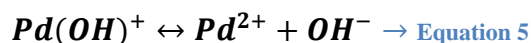
palladium surface brings about the formation of PdO and intermediate Pd(OH), as can be seen from equation 1 and 2.



As the potential increases, the surface oxide formation continues to increase with a peak maximum at 0.9 V-1.0 V followed by a plateau until 1.4V. In the regime between 1.0 V and 1.4 V, the palladium starts dissolving into the solution existing as Pd<sup>2+</sup> thermodynamically from 1.0 V. As the potential proceeds to 1.2 V, the oxidation state of palladium increases from +2 to +4, with the oxide transforming from PdO to PdO<sub>2</sub>. The anodic dissolution of palladium into the solution has been theorized to occur from 2 different sources, namely:



OR



At about 1.4 V, the current density slowly starts increasing, with an exponential increase observed to begin close to about 1.45 V caused due to the initiation of the oxygen evolution reaction. As we go cathodically from 1.4 V, the reactions occurring during the anodic cycle invert with a peak maximum observed close to 0.6 V. This peak observed around 0.6 V is associated to the reduction of oxides in addition to the precipitation of Pd<sup>2+</sup> dissolved ions. Below the double layer region, palladium begins to adsorb and absorb hydrogen with the anodic cycle inducing their desorption. [26] [27]. During the hydrogen cathodic regime, the absorbed hydrogen creates 2 different states in which palladium exist:

❖ α palladium

❖ β palladium hydride.

The formation of PdH<sub>x</sub> is said to be the X-factor that enables palladium to catalytically reduce CO<sub>2</sub>, with a maximum possible x value of 0.67. During this transformation, the

crystal structure still remains the same experiencing only an increase in its lattice parameters. Another interesting aspect that requires enumeration is the electrochemical behavior of palladium under varying electrolyte pH. Increasing the pH of the solution from acidic to alkaline has seen to produce significant effects on the palladium sample. This transformation in pH from 0 to 14 demonstrates an increased affinity and binding energy towards hydrogen and oxygen coupled with its decreasing propensity towards dissolution [28]. The increasing pH of the electrolyte has the tendency to shift the initiation potential for hydrogen desorption and palladium oxidation towards higher and lower potentials respectively, with the two peaks almost overlapping at highly alkaline electrolytes. [29]

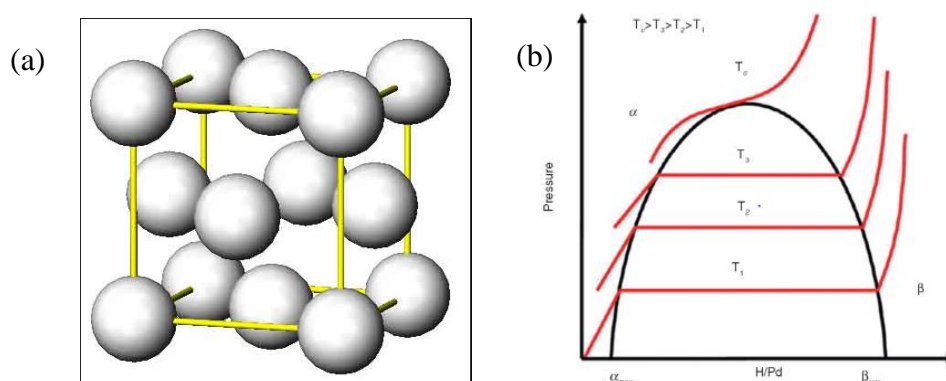


**Figure 2. 4 - (a) Illustration of the FCC crystal structure of palladium [30] and (b) Phase diagram of the palladium-hydrogen system [31]**

An integral part of palladium is its interplay with hydrogen. Palladium has the ability to absorb close to 900 times its volume of hydrogen, undergoing transformations based on hydrogen's concentration. The hydrogen absorbed occupies the octahedral interstitial positions within the F.C.C lattice forming palladium hydride. Figure 2.4(b) represents the phase diagram for hydrogen in bulk palladium at different temperatures and pressures. The diagram clearly depicts the existence of 2 forms,  $\alpha$  and  $\beta$  palladium hydride, along with three regions  $\alpha$ ,  $\alpha+\beta$  and  $\beta$  palladium hydride. The initiation of each of the 3 transformation zones are controlled by the temperature and pressure conditions maintained, as depicted in figure 2.4(b). The 2 forms of palladium observed during the course of the absorption process only bring about an increase in the lattice constant of the unit cell without initiating any phase transformation of the system.

While electrochemical processes are essential towards understanding the surface dynamics of the reaction, size variations also tend to impact reactions catalyzed by palladium. Observing figure 2.3 the amount of hydrogen adsorbed/absorbed is reliant on the amount of palladium, with hydrogen absorption being lower in thin films as compared to bulk palladium. This attribute of palladium is critical during the reduction of CO<sub>2</sub> as it enables rapid transformations between the two forms of palladium hydride. In addition to

the above mentioned characteristics of palladium thin films, they also tend to exhibit pseudomorphic behaviours with shifts in the initiation potentials of hydrogen adsorption, absorption and oxide reduction. [25] [32]. An example with regards to the pseudomorphic behaviour is given figure 2.3(b) with regards to the varying thicknesses. The increase in thickness of the palladium thin film causes not only the immediate onset of oxide reduction, but also the delayed initiation of H adsorption.

### 2.3 CO adsorption on Palladium

The presence of carbon monoxide (CO) around the palladium surface has an innate tendency to deactivate the catalyst, thus reducing its performance over a period of time. Therefore, the first step in determining possible solutions for the reduction of carbon monoxide poisoning is to understand the process of its adsorption. This sub-chapter will briefly describe the adsorption of CO on the various facets of the palladium surface.

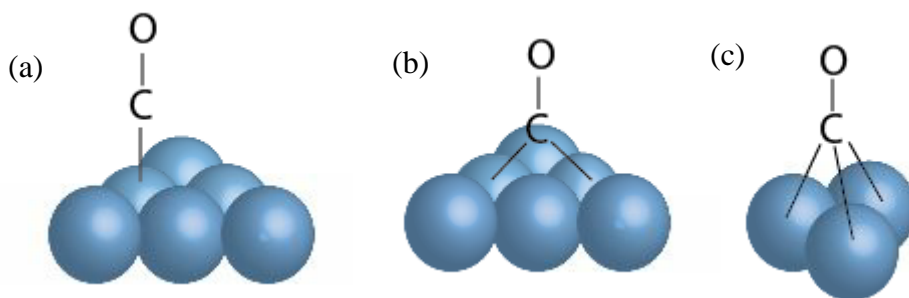


**Figure 2. 5 - Schematic representations of CO on palladium at the (a) A-Top site, (b) Bridge site and (c) Hollow site**

Beginning with the lowest miller index, the Pd(111) surface has one of the most complex CO adsorption mechanisms. The CO under ultra-high vacuum (UHV) displays a transformation in its adsorption from hollow sites at low coverage's, to bridge sites at intermediate coverage's; finally culminating at a combination of atop and hollow sites at the maximum possible surface coverage. Based on the low energy electron diffraction spectroscopic (LEEDS) measurements, the plane at low surface coverage's shows a  $(\sqrt{3} \times \sqrt{3})R30^\circ$  structure, a compressed  $C(4 \times 2)$  structure at intermediate coverage's and a  $(2 \times 2)$  structure at the maximum possible surface coverage. The system is observed to move from a disordered state at low coverage's, to one with order as the surface coverage increases. The system shows compression and early signs of repulsion at coverage's close to 0.4 due to the close packed structure of the plane. The data obtained by studies from thermal desorption spectroscopy of the CO covered Pd (111) surface illustrates similar conclusions as of those mentioned above. In addition, they also discuss the strength of the adsorbed species with the system showing desorption as well as site transformation as the temperature rises. Under those conditions the plane depicts

strong chemisorption for the hollow sites formed initially (desorption at 500K), but weakens when it preferentially forms on the a-top and hollow sites at higher coverage's (desorption at 170K). [33] [34]

The adsorption mechanism observed on Pd(100) and Pd(210) under UHV are much more straightforward, with the CO only occupying bridge sites irrespective of the surface coverage. The only noticeable change with the increasing surface coverage is the transformation from a disordered state to a highly ordered state. This transition is coupled with the change in its structure, from  $C(4 \times 2)R45^\circ$  until a coverage of 0.5 to  $C(2\sqrt{2} \times \sqrt{2})R45^\circ$  above it. As the coverage increases beyond 0.6, the molecular orbitals of the neighboring CO bonded atoms begin to interact, leading to the formation of strong repulsive forces. **A.M.Bradshaw et.al** [34] observed that upon drastically increasing the pressure and therefore the coverage of CO on Pd (100), adsorption tends to occur on energetically unfavorable sites through the formation of linear bonds. [34]

The adsorption of CO on Pd (210) is quite unique in comparison to the other sites. Figure 2.6 is a schematic diagram depicting the adsorption sites on the Pd(210) plane. At low coverage's, the CO is observed to occupy the C site with the molecule chemisorbed at an inclination away from the surface normal. Upon increasing the CO coverage, the molecule is also seen occupying the B sites. Temperature programmed desorption (TPD) studies have shown that CO adsorbed on B sites tend to form weaker bonds with the substrate in comparison to the C sites, thus reducing the motivation to bond on the B site. The structure initially assembles in a  $(1 \times 1)$  configuration; transforming to a  $(1 \times 2)$  configuration as the coverage increases. Unique in its involvement, the first as well as the second layer of Pd(210) participates in the chemisorption process [35]. Although only limited information is available on Pd(112), the fact that the surface is a mixture of Pd(100) and Pd(111) suggests chemisorption to occur on both bridge as well as hollow sites. The chemisorbed CO molecules on Pd(112) showcase short range order but long range disorder [36].

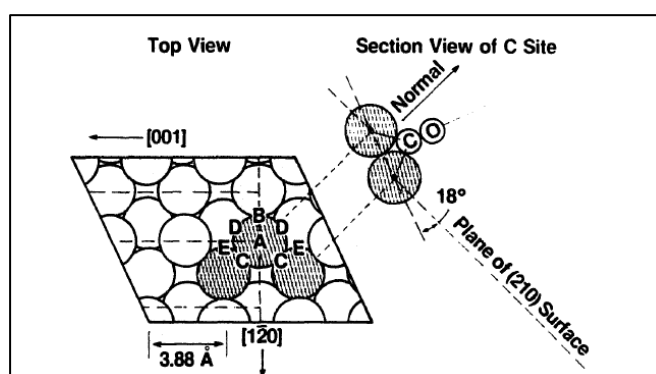


Figure 2. 6– The different sites available on Pd(210) surface [35]

The common observation in all of the above mentioned palladium surfaces were that the activation energy for the adsorption process was found to decrease with an increase in the CO coverage. The basic chemistry behind the adsorption of CO is described by the Blyholder model. According to the model, the CO molecule donates electrons from its  $\sigma$  orbital to the metal forming strong  $\sigma$  bonds while the metal simultaneously back donates electrons from its d orbital to the CO  $2\Pi^*$  orbital. The greater the back donation, stronger is the C-palladium bond which in turn weakens the  $C\equiv O$  molecular bond. But as the coverage increases, the repulsive forces between the chemisorbed atoms become stronger; forcing a reduction in the electron back donation and therefore a reduction in the binding energy. The electron back donation theory also works for the adsorption strength and therefore partially correlates with the IR vibrational frequency of the respective bonding types (atop, bridge and hollow). Therefore, this effect of the activation energy is found irrespective of the plane on which the chemisorption process occurs. Another significant observation from CO adsorption on the various palladium facets was that the CO would initially occupy the edge, corner or steeped sites but with increasing coverage would begin occupying the terrace sites as well. [37] [36]

Studies related to the co-adsorption of CO and H<sub>2</sub> on Pd were also reviewed to a certain degree to provide better perspective on their interaction during the electrochemical study. Palladium with large surface hydrogen coverage (H<sub>2</sub> scenario) demonstrates competitive adsorption with CO at low CO coverage's, with CO beginning to replace the adsorbed hydrogen as the CO surface concentration increases. This substitution occurring between CO and H doesn't affect the hydrogen absorbed by palladium, thus retaining the phase prior to the CO chemisorption. Thermal desorption studies (TDS) have revealed that at high CO coverage's, CO and adsorbed hydrogen tend to desorb simultaneously as hydrogen recombination necessitates the availability of active surface sites. Such results are also visible for surfaces that were initially covered with CO, but the hydrogen desorbed from the surface is minimal in comparison to the H<sub>2</sub> scenario. [38] [39] [40]

### 2.4 CO<sub>2</sub> reduction reaction on the palladium thin film

The potential societal impact of the electrochemical reduction of CO<sub>2</sub> has made it one of the most sought after research topics in the 21<sup>st</sup> century. The linear covalently bonded CO<sub>2</sub> has a high thermodynamic stability, requiring external energy to facilitate its reduction into useful carbon based products. These products formed depend greatly on the applied potentials and catalyst's implemented during the reduction reaction.

Reaction	E (V) vs. SHE
$2\text{H}^+ + 2\text{e}^- \rightarrow \text{H}_2$	-0.41
$\text{CO}_2 + 2\text{H}^+ + 2\text{e}^- \rightarrow \text{HCOOH}$	-0.61
$\text{CO}_2 + 2\text{H}^+ + 2\text{e}^- \rightarrow \text{CO} + \text{H}_2\text{O}$	-0.53
$\text{CO}_2 + 4\text{H}^+ + 4\text{e}^- \rightarrow \text{C} + 2\text{H}_2\text{O}$	-0.20
$\text{CO}_2 + 4\text{H}^+ + 4\text{e}^- \rightarrow \text{HCHO} + \text{H}_2\text{O}$	-0.48
$\text{CO}_2 + 6\text{H}^+ + 6\text{e}^- \rightarrow \text{CH}_3\text{OH} + \text{H}_2\text{O}$	-0.38
$\text{CO}_2 + 8\text{H}^+ + 8\text{e}^- \rightarrow \text{CH}_4 + 2\text{H}_2\text{O}$	-0.24

Figure 2. 7 - Standard redox potentials for the various CO<sub>2</sub> by products [41]

The thermodynamic potentials for the reduction of CO<sub>2</sub> and hydrogen, as given in figure 2.7, indicates a decrease in its values as the complexity of the product formed increases. Although theoretically plausible, the formation of these reduction products is inhibited due the increased selectivity towards the evolution of hydrogen. In addition to the competitive reaction environment, the assimilation of electrons as the value of n (number of electrons) increases, for the n-electron reaction pathway, further amplifies the difficulty encountered during the direct reduction of CO<sub>2</sub>. Therefore the utilization of catalysts is one way to go about, enabling the creation of intermediates that drastically reduces the potential required for the formation of particular by-products. The most commonly studied metallic catalysts can be divided into 3 sub categories based on the by-products they prefer to form:

- Formate selectivity -: lead, tin, indium and palladium
- CO selectivity – : Gold, silver, zinc and palladium
- Hydrogen selectivity -: Nickel, iron, platinum and palladium
- Hydrocarbon selectivity -: Copper

Keeping in mind that the goal of the study is to identify mechanisms associated with the formation and growth of CO on the palladium thin film, a thorough analysis of all the existing information is necessitated in order to achieve an informed analysis of the data secured.

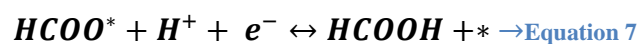


# In-Situ Infrared Spectroscopic Studies Of Palladium Thin films during CO<sub>2</sub> Electro-Reduction

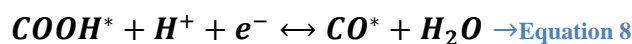
	catalysts	electrolyte	potential (V vs RHE)	FE <sub>CO</sub> (%)	j <sub>CO</sub> (mA cm <sup>-2</sup> )	j <sub>CO</sub> (mA mg <sup>-1</sup> )
(a)	Pd foil <sup>20</sup>	0.1 M KHCO <sub>3</sub>	-0.8	28.3	1.4	N.R. <sup>a</sup>
	Pd NPs <sup>21</sup>	1 M KHCO <sub>3</sub>	-0.7	93.4	22.9	57.5
	Pd NPs <sup>22</sup>	0.1 M KHCO <sub>3</sub>	-0.89	91.2	8.9	23.9
	Pd/C <sup>23</sup>	0.5 M NaHCO <sub>3</sub>	-0.6	~40	0.3	N.R.
	mesoporous PdCu <sup>24</sup>	0.1 M KHCO <sub>3</sub>	-0.8	80	~0.8	N.R.
	PdCu NPs <sup>25</sup>	0.1 M KHCO <sub>3</sub>	-0.89	86	6.9	24.5
	Au NPs <sup>26</sup>	0.5 M KHCO <sub>3</sub>	-0.67	90	N.R.	~8
	Au nanowire <sup>27</sup>	0.5 M KHCO <sub>3</sub>	-0.35	94	4.2	1.84
	oxide-derived Au <sup>28</sup>	0.5 M KHCO <sub>3</sub>	-0.4	>98	10	N.R.
	nanoporous Ag <sup>29</sup>	0.5 M KHCO <sub>3</sub>	-0.6	~92	18	N.R.
	Ag NPs <sup>30</sup>	0.5 M KHCO <sub>3</sub>	-0.75	84.4	3.5	~40
	Zn dendrite <sup>31</sup>	0.5 M NaHCO <sub>3</sub>	-1.1	79	~17	N.R.
	Cu hollow fiber <sup>32</sup>	0.3 M KHCO <sub>3</sub>	-0.4	72	~10	N.R.
	CuIn <sup>33</sup>	0.1 M KHCO <sub>3</sub>	-0.6	85	~0.6	N.R.
	CuSn <sup>34</sup>	0.1 M KHCO <sub>3</sub>	-0.6	~90	~1	N.R.
	rGO-PEI-MoS <sub>2</sub> <sup>35</sup>	0.5 M NaHCO <sub>3</sub>	-0.65	85.1	4.8	21.7
	Ni-N-C <sup>36</sup>	0.1 M KHCO <sub>3</sub>	-0.75	~85	~10	~9
	graphene foam <sup>37</sup>	0.1 M KHCO <sub>3</sub>	-0.58	~85	~1.8	N.R.
<sup>a</sup> N.R.: not reported.						
	catalyst	electrolyte	potential <sup>a,b</sup>	FE <sub>formate</sub> (%)	j <sub>formate</sub> (mA cm <sup>-2</sup> )	j <sub>formate</sub> (mA mg <sup>-1</sup> )
(b)	Pd foil <sup>20</sup>	0.1 M KHCO <sub>3</sub>	-0.8 <sup>a</sup>	2.8	0.14	N.R. <sup>c</sup>
	Pd NPs <sup>21</sup>	1 M KHCO <sub>3</sub>	-0.1 <sup>a</sup>	97.8	15.4	40.5
	Pd/C <sup>38</sup>	0.5 M KHCO <sub>3</sub>	-0.15 <sup>a</sup>	>90	~2.5	40
	PdSn/C <sup>39</sup>	0.5 M KHCO <sub>3</sub>	-0.43 <sup>a</sup>	99.3%	~2.5	N.R.
	PdPt NPs <sup>40</sup>	0.1 M K <sub>2</sub> HPO <sub>4</sub> /0.1 M KH <sub>2</sub> PO <sub>4</sub>	-0.4 <sup>a</sup>	88	~5	44
	Pd-PAN/CNT <sup>41</sup>	0.1 M KHCO <sub>3</sub>	-0.15 <sup>a</sup>	83	~4	N.R.
	partially oxidized atomic Co layer <sup>9</sup>	0.1 M Na <sub>2</sub> SO <sub>4</sub>	-0.85 <sup>b</sup>	90.1	10.59	N.R.
	Co <sub>3</sub> O <sub>4</sub> layer <sup>42</sup>	0.1 M Na <sub>2</sub> SO <sub>4</sub>	-0.88 <sup>b</sup>	64.3	0.68	N.R.
	Cu foam <sup>43</sup>	0.1 M KHCO <sub>3</sub>	-0.45 <sup>a</sup>	23	2.2	N.R.
	oxide-derived Pb <sup>44</sup>	0.5 M NaHCO <sub>3</sub>	-0.7 <sup>a</sup>	95	~0.3	N.R.
	tin/tin oxide film <sup>45</sup>	0.5 M KHCO <sub>3</sub>	-0.7 <sup>a</sup>	40	1.8	N.R.
	SnO <sub>2</sub> /graphene <sup>46</sup>	0.1 M KHCO <sub>3</sub>	-1.8 <sup>b</sup>	86.2	13.1	N.R.
	PEI-coated NCNT <sup>47</sup>	0.1 M KHCO <sub>3</sub>	-1.8 <sup>b</sup>	87	9.5	N.R.
<sup>a</sup> V vs RHE. <sup>b</sup> V vs SCE. <sup>c</sup> N.R.: not reported.						

Figure 2. 8 - Overview of the Faradic efficiencies obtained for (a) CO and (b) formate over a number of commonly studied catalysts [15]

As discussed previously and depicted in figure 2.8, palladium has the ability to reduce CO<sub>2</sub> to formic acid and CO along with the evolution of hydrogen. Furthermore, the reversible oxidation of formic acid over identical active sites has encouraged researchers towards pursuing and optimizing palladium as a catalyst for the reduction of CO<sub>2</sub>. Palladium's advantage to form formic acid at low over potentials is completely overshadowed by the competition it faces from hydrogen and CO that forms concurrently on its surface. Thus the essence of the optimization process lies in better understanding the CO<sub>2</sub> reduction reaction in an effort to eliminate these side reactions and maximize the formic acid production. During the electrochemical reduction of CO<sub>2</sub>, the following reaction steps are proposed to take place on the palladium surface:



OR



The reduction reaction over the palladium surface is considered to be influenced by the following parameters:

- 1) Surface morphology
- 2) Palladium thickness
- 3) Electrochemical potential and palladium-hydrogen phase stability
- 4) pH and electrolyte

All of the above mentioned parameters are interconnected and necessitates elaboration to better estimate their contribution towards the reduction of CO<sub>2</sub>. The surface morphology of the palladium catalyst is a crucial parameter towards initiating the reduction reaction, irrespective of whether the product is formic acid or carbon monoxide. Numerous theoretical as well as experimental studies have deduced the necessity of high miller indexed active sites in order to initiate the CO<sub>2</sub> reduction reaction with ease. Terrace, edge, step and corner sites are the four different positions on which CO<sub>2</sub> adsorption and reduction can possibly occur, out of which terrace sites are said to be the least productive. [17] Studies conducted on palladium foils and wires, predominantly consisting of terrace sites, have shown to form substantial amounts of hydrogen with minimal and negligible amounts of CO and formic acid at high cathodic over potentials ( $\geq 0.8\text{V}$  (RHE)). **Klinkova et al.** performed DFT calculations on (111), (100), (110) and (211) to determine the gibbs free energy required for the formation of formic acid on each of the facets, with (111) requiring the highest while (211) required the lowest. [13] The high coordination number and low surface energy is therefore a clear inhibitor for the formation of formic acid and CO. The need for high index facets has led to the introduction of palladium nanoparticles which offers a mixture of low and high indexed facets depending on the size of the nanoparticles. [17] The reduction of size creates a volcano chart with regards to the formic acid faradic efficiency, with the optimal size balancing the competitive hydrogen evolution with the CO poisoning. [17] [42] [43]

The aforementioned theoretical and experimental results showed that the formation of formic acid and CO is clearly dependent on the surface morphology and particle size of the catalyst. Based on these parameters, the electrochemical potential tends to vary with palladium wires/foils forming negligible formic acid and minimal CO above -0.8 V. In contrast, nanoparticles generally tend to exhibit three different zones, with formic acid forming between 0 V and -0.4 V, H<sub>2</sub> evolving between -0.4 V and -0.6 V and CO forming at potentials beyond -0.6 V. This segregation across the potential range can be, to a certain degree, associated to the palladium hydrogen system and H coverage on the catalyst surface. DFT calculations performed to assess the impact of H coverage on product selectivity had demonstrated an increase in formic acid production with an ever increasing adsorbed hydrogen concentration, while the vice versa was found to be true for the CO molecule. The figures acquired at the end of the analysis predicts an increase in the gibbs free energy of formation and reduction in the binding energy as the surface H

coverage decreases, while considering the formation of formic acid. This variation in the surface H coverage was found to be partially linked to the behavior expressed by the palladium-hydrogen system, giving rise to three characteristic phases namely:

- 1)  $\alpha+\beta$  PdH<sub>x</sub> – maximum H coverage
- 2) Transition region – Intermediate H coverage
- 3)  $\beta$ PdH<sub>x</sub> with a small percentage of palladium metal – minimal H coverage

Each of these phases tend to emerge over specific cathodic potentials; with Regime I existing at lower potentials while regime II and III thrive as the value increases. Synonyms to the cathodic potentials, regime I was found to yield formic acid with regime II and III producing H<sub>2</sub> and CO respectively. [17] [44] [16] [42] [43] [45]

A lot of focus in this section has been awarded to the cathode, in specific palladium, which constitutes only part of the electrochemical cell. Another crucial component of the setup without which the reaction would be incomplete is the electrolyte. The most crucial parameters that require consideration before selecting an appropriate electrolyte are the following:

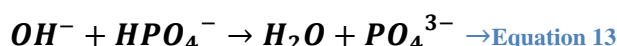
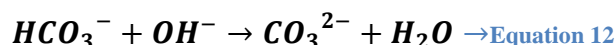
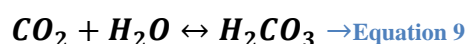
- Anion of the solution
- Cation of the solution
- Concentration of the salt

As the electrolyte tends to control the pH, solubility and CO<sub>2</sub> reduction rate in the electrochemical system, these parameters will be discussed simultaneously over the remainder of the sub-chapter. The pH of the solution has a drastic effect on the adsorption/absorption and desorption of hydrogen, with acidic solutions facilitating lowered formic acid initiation and basic solutions impeding CO formation and hydrogen evolution. [46] Alkali metals have been one of the most commonly used cations in numerous electrochemical CO<sub>2</sub> reduction studies. Based on the experiments performed by **Singh et al.** [47] on copper and silver electrodes, the size of the metal ions were found to play crucial roles in controlling the local pH of the solution. The study clearly depicts the impact alkali metals have on the pH, with Li<sup>+</sup> exhibiting the least and Cs<sup>+</sup> the most effect. Due to the low hydration number for Cs<sup>+</sup> in comparison Li<sup>+</sup>, there are visibly 3 sets of interactions that ensue close to the cathode:

- I Electrostatic interaction between the cation and the surrounding water molecules
- II Electrostatic interaction between the cation and the cathode
- III Electrostatic interaction between the cation and the surface reactions

The interaction between the cation and the cathode facilitates the hydrolysis of the surrounding H<sub>2</sub>O molecules, inducing the formation of H<sup>+</sup>. The H<sup>+</sup> ion generated facilitates the neutralization of by-products formed by the cathode, thus partially operating as a buffer. Further interactions between the cations and the surface reactions have shown to stabilize certain surface intermediates thus suggestive of the influence cations have over the selectivity of products formed. Studies have also hypothesized on the impact the cations have on promoting the reduction of CO<sub>2</sub>, with the zeta potential playing an integral role in the reduction of its activation energy. In combination with the above mentioned phenomena, the use of potassium in comparison to sodium and lithium as cations for palladium electrodes has shown to portray higher hydrogen evolution from its surface. [48] [49] [47] [50]

Similar to the cations, a number of anions such as CO<sub>3</sub><sup>2-</sup>, ClO<sub>4</sub><sup>-</sup>, OH<sup>-</sup>, bicarbonate buffers, phosphate buffers, etc. have been studied, with the phosphate and bicarbonate buffers being favored for the electrochemical reduction of CO<sub>2</sub>. The logic behind choosing phosphate or bicarbonate as the anion stems from its innate ability to combine with the hydroxyl ions generated during hydrogen absorption/evolution, thus preventing side reactions from occurring with the dissolved CO<sub>2</sub>. Equations 12 and 13 depict the reactions that occur between the phosphate/bicarbonate anion and the hydroxyl ion, facilitating longer reduction spells at higher efficiencies. An additional incentive for the implementation of bicarbonate ion is defined in equation 9, which demonstrates the existence of the bicarbonate species in a state of reversible equilibrium with CO<sub>2</sub>; creating ideal reaction conditions for CO<sub>2</sub> reduction. [48]



Finally, an appropriate concentration of the salt must be selected to obtain optimal conditions for the effective electrochemical reduction of CO<sub>2</sub>. It's essential to identify an appropriate quantity, where it is sufficient to provide low IR losses while simultaneously allowing the reduction of CO<sub>2</sub> without the cation blocking active sites on the electrode surface. **Zhong et al.** [51] had observed that at high electrolyte concentrations, the

cations tend to completely populate the surface of the copper electrode; denying CO<sub>2</sub> any sort of access to the surface reaction site. This in turn negatively affects the efficiency of the CO<sub>2</sub> reduction reaction, without affecting the evolution of hydrogen due to the disparity existing between their molecular dimensions. It is therefore paramount to perform preliminary studies to determine the appropriate concentrations of the salt; all in a bid to optimize the CO<sub>2</sub> reduction reaction.

### 2.5 Surface Enhanced Infrared Absorption Spectroscopy

Spectroscopy can be defined as a methodology that exploits the information gathered during the interaction between matter and electromagnetic radiations in order to determine its fundamental properties. One such technique that facilitates the determination of the physical structure and concentration of the subject of interest through the initiation of molecular vibrations is “**Infrared Spectroscopy**”. The technique works on the basis of absorbing IR radiations in the wavelength range of 500  $\mu\text{m}$  to 0.7 $\mu\text{m}$ , thus initiating vibrations at resonant frequencies. This vibration in turn enables the detection of specific bonds present within the system, thus enabling partial identification of molecular species within the system. In order to initiate these specific molecular vibrations, the fundamental property, that requires the presence of a dipole moment, needs to be fulfilled. [52] Upon absorption of the infrared spectra, the following are the possible vibrational motions that can be anticipated from the subject of interest:

- Stretching: Symmetric and asymmetric
- Bending :
  - a) Symmetric: Scissoring and wagging
  - b) Asymmetric: Rocking and twisting

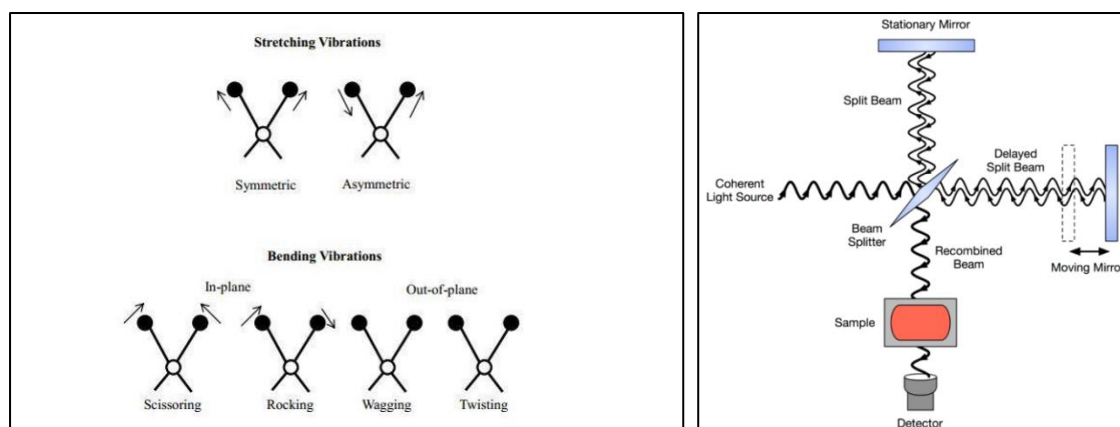


Figure 2. 9 - (a) Schematic diagram depicting the various vibrational motions [53] and (b) Schematic description of an FTIR spectrometer [54]

For the successful implementation, collection and interpretation of the infrared data, a **Fourier Transform Infrared Spectrometer** (FTIR) is utilized enabling the determination of chemical structures of a vast number of samples. Figure 2.9(b) is a diagrammatic representation of a commonly utilized FTIR spectrometer having a silicon carbide source (Globar) (wavelength range of 2.5-25  $\mu\text{m}$ ) and a “Mercury-Cadmium-Telluride” detector (MCT). The poly-chromatic IR spectra generated by the source is directed towards the interferometer. At the interferometer the beam is split into a number of individual spectra’s through constructive/destructive interference due to the presence of a beam splitter, a stationary and moving mirror. Each of these spectra’s interact with the sample as they pass through and make up unique data sets, which are then collected and converted with the help of the detector. All the data sets are then converted into an analyzable format through the use of fourier transformation. The advantage of using the FTIR spectrometer is that it enables quick analysis of a sample over a spectral range with high resolution of the data.

In the year 1980, **A.Hartstein, J.R.Kirtley and J.C.Tsang** during their infrared study on the “Adsorption of organic thin films over silicon substrates” observed an enhancement in the spectra recorded when a thin film of silver or gold was coated either over or under the organic thin film. This was the very first scientific study published introducing a revolutionary surface reaction analysis technique termed “**Surface Enhanced Infrared Absorption Spectroscopy**”, which has ever since been extensively studied and implemented by the scientific community. Surface enhanced infrared absorption spectroscopy is an in-situ near field analysis technique that facilitates real time surface dynamic studies of molecules adsorbed over a metallic surface. During this study, the normal vibrations of the adsorbed species, caused by the absorption of IR radiation, are amplified due the presence of the metallic interface. [55] A basic description on the working principle has been provided within the study to familiarize the reader and also possibly entice them in a pursuit towards understanding and implementing this analysis technique in future publications.

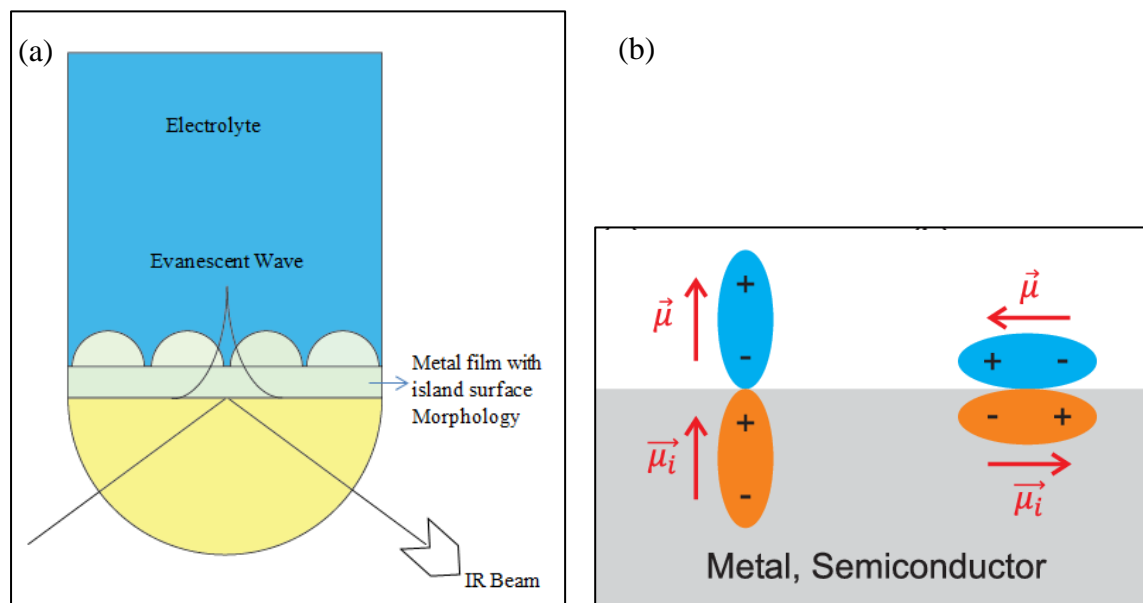


Figure 2.10 - Diagrammatic representation of the (a) SEIRAS process and (b) Perpendicular dipole moment being enhanced while the parallel dipole moment gets cancelled by its mirror image [56]

“**Surface Enhanced Infrared Absorption Spectroscopy**” or “**SEIRAS**” utilizes an “**Attenuated Total Reflectance**” crystal (ATR crystal) coated with a layer of the metal on which the reaction is to be analysed. The ATR crystal acts as an internal reflective element for the infrared beam incident onto its surface and therefore, necessitates a higher refractive index for the crystal in comparison to the metal. Table 1 presents a few frequently utilized ATR crystals that exist in the market currently, with silicon and germanium being the most commonly used crystals for studies of this nature. As the infrared light is incident onto the surface of the crystal at its critical angle, an electromagnetic evanescent wave emerges at the interface over the metallic side of the sputter deposited ATR crystal. The metal surface partially absorbs the EM wave enhancing the vibrations of the adsorbed as well as the electrolyte species up to a short distance from the metal - electrolyte interface. This absorption of the evanescent wave effects the reflected wave at the interface, giving rise to variations in IR spectra relating to the respective species.



## In-Situ Infrared Spectroscopic Studies Of Palladium Thin films during CO<sub>2</sub> Electro-Reduction

Table 2. 1- Different types of ATR crystals available for Infrared spectroscopic studies [57]

S.NO	ATR Crystal
1	Zinc Selenide
2	Germanium
3	Zinc Sulfide
4	Silicon
5	Diamond

The infrared light, which is an electromagnetic radiation, consists of two types of linear polarization states -:

- 1) S-polarization (perpendicular to the plane of incidence)
- 2) P-polarization (parallel to the plane of incidence)

At the point of incidence on the metal –ATR interface, the S-polarized component of the EM wave undergoes a 180° phase change irrespective of the incidence angle. This therefore leads to the elimination of the S- polarized component of the EM wave due to destructive interference of their electrical component. The P-polarized component on the other hand provides increased activity as the incidence angle grows due to the constructive interference of its normal electrical component. This increase can only facilitate the enhancement phenomena up to a maximum angle of incidence called the “grazing angle” beyond which, the P-polarized component undergoes a 180° phase change therein eliminating all possible vibrational signals from the metal surface. For molecules to be IR active, their vibrations must bring about a change in the dipole moment. For the molecule adsorbed on the surface of the metal, only vibrations with a normal component, with respect to the surface, will produce a dipole moment change. This selection rule exists due to the presence of delocalized electrons which orient themselves to form dipole images that cancel out in the case of parallel components, while the dipole moment changes are enhanced for the normal components giving rise to IR activity. [58] [55]

In addition to the incidence angle, the metal thin film is also seen to play a crucial role in the enhancement of the IR spectra. Thus, a brief overview of the thin films involvement is touched upon in the forthcoming paragraphs. A key aspect of the enhancement is the need for island like structures on the surface of the metal; enabling initiation of the surface enhancement factor. Studies have shown that an increase in the diameter of these islands bring about a visible increase in the enhancement factor, until the point where the

islands begin to coalesce. As the particles begin to coalesce, the diameters of the islands begin to rise drastically; deviating from the Rayleigh zone. This therefore causes a reduction in interaction between the metal and the EM wave [59]. Studies have also shown that the electric component of the EM wave plays an integral part in initiating the enhancement factor in the system.

Similarly, the thickness of the thin film is another critical parameter that determines the effect of the enhancement factor. Studies have indicated an increase in the enhancement factor up till a certain maximum thickness, beyond which the effect is seen to diminish. The reason behind this diminishing effect can be associated to the extent of the evanescent wave absorbed by the surface islands, which attains maxima at the optimal thickness and decreases on either side of that value. This effect of the thickness can be understood by conceptualizing the growth kinetics of the thin film. As the thickness of the thin film increases, the diameter of the island structures also increase; giving rise to an increase in the adsorbed species. At the optimal thickness, the island structures will be in close proximity but will not impinge upon each other; giving rise to maximum surface IR signals. As the thickness grows beyond this optimal value, the islands begin to coalesce; traversing beyond the Rayleigh zone as discussed previously. In addition to the growth kinetics, the optimal thickness of the thin film is also a function of the ATR crystal as they are the ones that determine the depth of penetration of the evanescent wave. Equation 15 and 16 define the penetration depth of the evanescent wave and the effective thickness of the metal thin film coated on the surface of the ATR crystal. [55] [60]

$$\sin \theta_c = \frac{n_{sample}}{n_{crystal}} \rightarrow \text{Equation 14}$$

$$\text{Depth of penetration} = \frac{\lambda}{2\pi n_{ire} \sqrt{(\sin \theta)^2 - \left(\frac{n_{sp}}{n_{ire}}\right)^2}} \rightarrow \text{Equation 15}$$

$$\text{Effective thickness} = \frac{\left(\frac{n_{smp}}{n_{crystal}} * E^0^2 * d_p\right)}{(2 * \cos \theta)} \rightarrow \text{Equation 16}$$

The mechanism associated to the enhancement on the surface of the thin film is of two types:

### 1) **Electro-Magnetic enhancement:**

As the evanescent wave upon creation at the metal-ATR interface travels into the sample, it gets absorbed by the island structures present on the metal surface. The absorption that occurs at the island structures is basically an interaction that transpires between the electrical component of the evanescent wave (EM wave) and the plasmon's on the islands. This absorption cause's localized excitation of plasmons, polarizing them to create a dipole moment and therefore creating a short ranged electric field. This electric field enables studying not only the chemisorbed species but also physically adsorbed species up to a certain extent from the metal surface.

### 2) **Chemical enhancement:**

Species adsorbed onto the surface of the metal undergoes transformation due to electron transfers happening to and from the metal. Depending upon the strength of the bond, a shift in the charge distribution across the species can be brought about thereby activating the species. Another possible scenario is the preferential orientation of the chemisorbed species by the metal surface, facilitating the enhancement of the IR vibrations through the execution of the selection rules.

Numerous studies have been conducted using SEIRAS to examine the reduction of CO<sub>2</sub>, oxidation of formic acid and the chemisorption of CO on the palladium surface. These studies were never performed independently and were conducted along with electrochemical and DFT studies, thus providing essential insights into the possible IR peak positions associated to the various species that may be encountered during the study. Table 2 is a consolidated list of peak positions for the species that may be visible on the palladium surface during the CO reduction reaction study.

## In-Situ Infrared Spectroscopic Studies Of Palladium Thin films during CO<sub>2</sub> Electro-Reduction

Table 2. 2- Literature values for IR spectra's of species that would be observed during the SEIRA spectroscopic study

S.No	Species	Wave Number (cm <sup>-1</sup> )
1	PdH <sub>x</sub>	760 and 880 [61]
2	CO symmetric stretching (Bidentate (Bridge bonded) Formate)	1338 [16]
3	HOC bending (Bicarbonate)	1212 [62]
4	COO symmetric stretching (Bicarbonate)	1020 [62]
5	COO asymmetric stretching ( Bicarbonate)	1507 [62]
6	CO stretching (Carbonate )	1577 [62]
7	HOH bending (Water)	1650 [16]
8	Hollow site CO	1800-1880
9	Bridge site CO	1930-2000
10	A-top CO	2050-2120
11	CO asymmetric stretching (CO <sub>2</sub> )	2300 [16]
12	OH stretching (Water)	3600-3800

## III Materials and Methodology

---

Details enumerating the preparation, characterization and experimental techniques implemented during the study are critical towards interpreting the results recorded appropriately. Therefore, the objective of the current chapter is to introduce techniques implemented not only for the fabrication and characterization of the palladium thin films, but also for the analysis of the CO<sub>2</sub> reduction reaction.

### 3.1 Cleaning the Cell

An integral aspect of obtaining accurate results lies in the cleanliness of the apparatus utilized during the study. The electrochemical – IR cell as depicted in figure 3.1(a) is first dismantled and separated into 3 categories based on the synthesized material:

- 1 PEEK
- 2 Stainless Steel
- 3 EPDMA/Viton( O-rings)

While performing experiments for the very first time or while shifting from one electrolyte to another, the EPDMA/ Viton and PEEK are submerged in 20% sulphuric acid solution separately overnight. Following the sulphuric acid cleansing, the components are allowed to boil in water twice for a period of 15 min's each. The stainless steel components on the other hand are sonicated for 10 min's in water followed by IPA and then again water. All the components were then dried with the help of a nitrogen gun. In situations where the electrolyte remains the same, the EPDMA/Viton and PEEK components are directly boiled in water twice for a period of 15 min's each. Once boiled, the components were then dried with the help of a nitrogen gun.

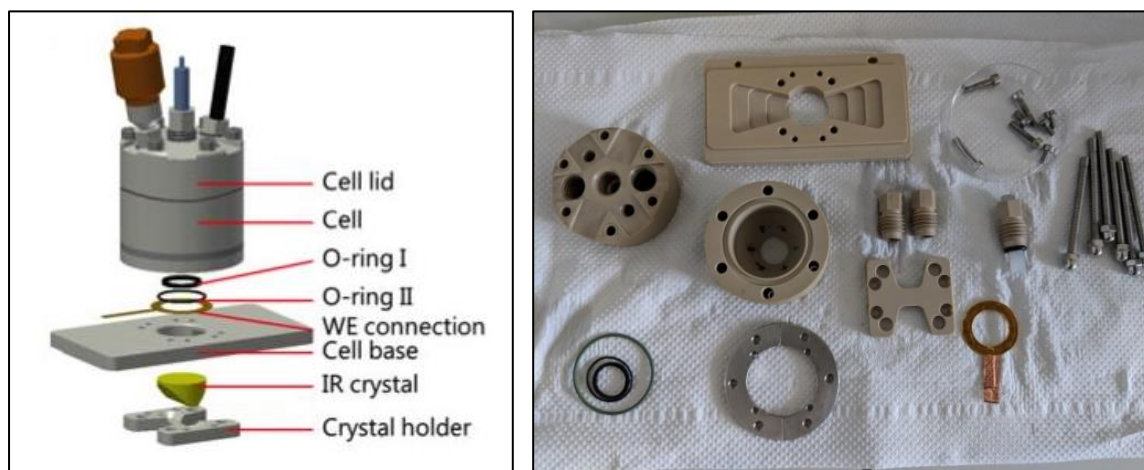


Figure 3. 1 - (a) Diagrammatic representation of the electrochemical-IR cell and (b) The various components of the electrochemical-IR cell

### 3.2 Palladium thin film preparation and characterization

#### 3.2.1 Thin film Preparation

A 15 nm palladium thin film was deposited onto the reflecting plane of a hemispherical 60° bevelled silicon internal reflection element (IRE) by magnetron sputter deposition (Prevac project 229). First the Si IRE was mirror polished by utilizing a 1.0  $\mu\text{m}$ , 0.3  $\mu\text{m}$  and 0.05 $\mu\text{m}$  grain sized alumina paste, followed by thoroughly washing the IRE with water, iso-propyl alcohol and finally water. The IRE was then dried with N<sub>2</sub> and placed into the IRE holder, after which it was loaded into the load lock of the sputtering system. Once the load lock reached a pressure of  $2.5 \times 10^{-6}$  mbar, the IRE was transferred into the sputtering chamber where a pressure of  $1.8 \times 10^{-7}$  mbar was maintained. The stage on which the IRE holder was placed had a working distance of 0.35mm and rotated at a velocity of 15°/s to enable uniform deposition of palladium over the Si IRE. Following this, argon was allowed to flow through the sputtering system maintaining a pressure of 3 $\mu\text{bar}$ , while a power of 15 was provided to initiate the sputtering process. The sputtering process was performed for 9 min's and 45secs at a rate of 0.256 Å° to produce a 15nm thick palladium nano-film that had a mirror finish similar to that of the silicon IRE.

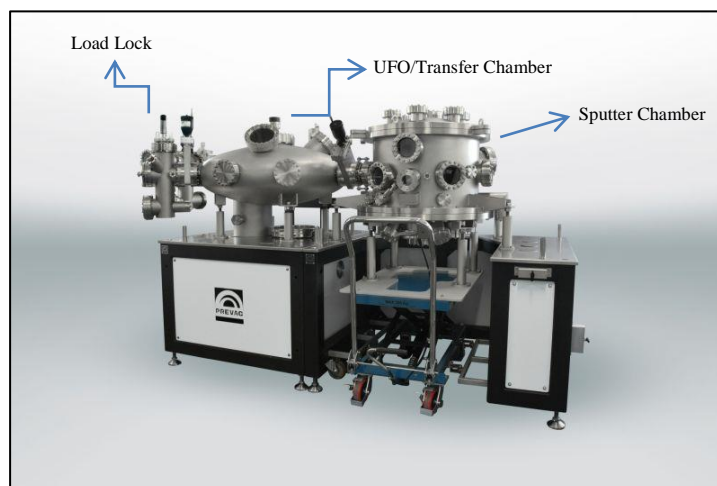


Figure 3. 2- Magnetron Sputtering System utilized for the deposition of Palladium on the silicon IRE [63]

### 3.2.2 Electrochemical Surface area characterization

The surface area of the activated palladium thin film was determined by electrochemically cycling the thin film between 0.35 V and 1.4 V in a CO<sub>2</sub> saturated 0.1M KHCO<sub>3</sub> electrolyte with a pH of 6.8 and at scan rate of 100 mV/s. Upon achieving the cyclic voltammogram, the area under the oxide reduction peak is determined to estimate the surface area of the palladium thin film activated. The highlighted peak in figure 3.3 is the reduction peak whose area was calculated to determine the surface area of the thin film.

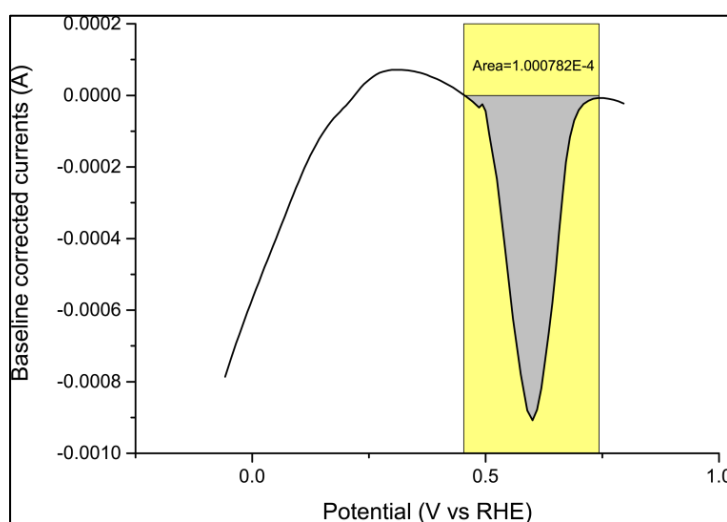


Figure 3. 3– Example of a palladium oxide reduction peak used for surface area determination [64]



### 3.2.3 Atomic Force Microscopy

Atomic Force microscopy or AFM is a technique designed to study the surface morphology of samples ranging from metallic to biological. The AFM apparatus consists of a probe with a radius of less than 10nm attached onto a cantilever. The apparatus can be operated in different settings namely:

- 1 Contact Mode
- 2 Intermittent Mode
- 3 Non- Contact Mode

;with each setting providing different sample – probe separation. The advantages associated with analyzing the sample through the contact mode include fast scans, detailed information of rough surfaces and friction analysis of the surface. During this study the contact mode was utilized to study the surface topography and therefore the probe was placed close to the surface of the sample with a separation distance between the two being close to 0.2-10 nm. As the probe was moved along the surface to be characterized, it experiences a repulsive force to extents depending on its proximity to the sample surface. Depending on the strength of the repulsive force, the cantilever deviates modifying the distance traversed by the laser between the cantilever and the photo detector (all with respect to a set equilibrium position); converting the extent of deflection into electrical signals which upon processing gives rise to the 3-D profile of the surface at the nano-scale level. Figure 3.4 pictorially represents the AFM instrument and the basic working principle associated with the system. [65]

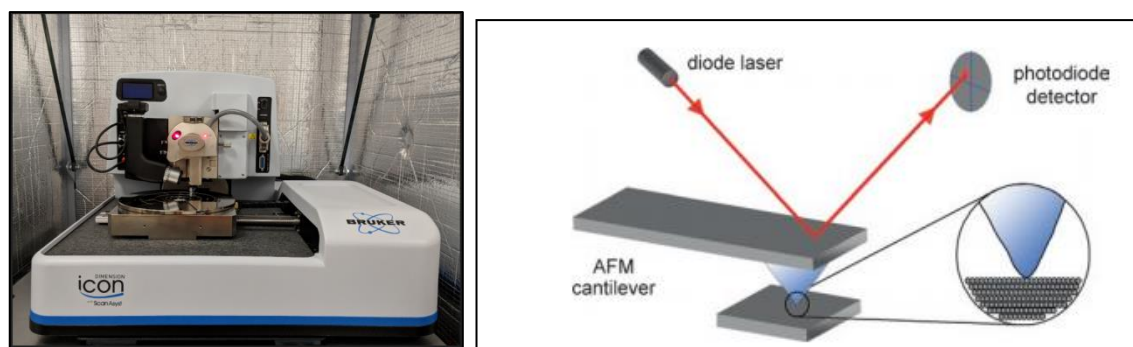


**Figure 3. 4 - (a) Bruker Atomic Force Microscopic setup and (b) Schematic representation of the Atomic Force Microscope in contact mode [65]**

Upon procuring the topographical profile of the surface, one must be able to analyze the data in order to extract vital information that can elucidate its nature and significantly contribute towards better understanding the reactions and trends observed. The following are the parameters extracted from the surface images through the application of **Nanoscope Analysis**:

- ❖ **RMS Roughness ( $R_q$ ):** The RMS roughness or  $R_q$  is a statistical method which determines the roughness of the surface profile recorded. The method is sensitive to the peak and valleys present on the surface of the material. The formula for calculating the  $R_q$  is given as -:

$$R_q = \sqrt{\frac{1}{L} \int_0^L |Z^2(x)| dx} \rightarrow \text{Equation 17}$$

Where L = Length

Z(x) = Height at a particular position along the measured distance L

- ❖ **Skewness:** Skewness is a statistical parameter that defines the morphology of the measured surface. The values vary about either side of 0, with negative values indicating a higher number of valleys/pores while the positive values depict a higher number of peaks.
- ❖ **Kurtosis:** Kurtosis is a statistical parameter that defines the broadness of the peaks on the surface of the material. The value is observed to vary either side of 3, with values greater than 3 displaying narrow peaks while the reverse is seen for values less than 3.

The AFM study was performed by the **Bruker Dimension Icon** on an as- sputtered 15 nm palladium thin film on a silicon ATR crystal. The scan size utilized during the study period was 500 nm×500 nm and 100 nm×100 nm.

### 3.3 Electrochemical and In-Situ Surface Enhanced Infrared Absorption Spectroscopy

A combination of electrochemistry and infrared spectroscopy, this in-situ measurement technique provides real time information on the interactions occurring over the palladium electrolyte interface. The electrochemical study employed a 3 electrode setup with the sputter deposited palladium acting as the working electrode, leak-less Ag/AgCl being the reference electrode while a graphite rod was used as the counter electrode.

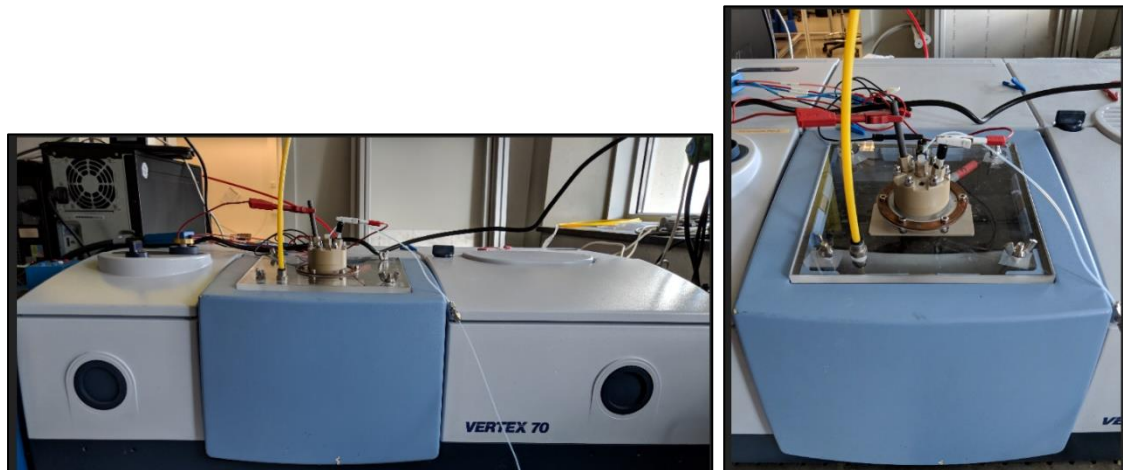


Figure 3. 5 - (a) Bruker Vertex 70 IR Spectrometer with the SEIRA spectroscopic cell and (b) A close-up of the fully functional setup

The setup (figure 3.1(a)) employed was constructed first by screwing together the cell and the cell base, with the gold contactor (to provide electrical contact with the working electrode) placed in-between them. To prevent leakage, the hole of the cell was partially covered with an O-ring having a diameter of 1.3 cm. The 15 nm palladium sputtered Si IRE is placed on top of the hole with the beam inlet/outlet facing the breadth of the cell base. In order to fasten the crystal into position, the crystal holder was screwed onto the base of the cell. The cell was then filled with 8 ml of the electrolyte, following which it was closed with the lid to create an air tight system. The lid of the cell consists of 5 holes, 3 big (diameter = 0.6cm) and 2 small (diameter = 0.2cm), with 2 out of the 3 big holes housing the counter and reference electrode while one of the 2 small holes acted as the gas inlet. To maintain an air tight system, the remaining big hole was blocked with a cylindrical plastic cork while the small hole was left unobstructed in order to prevent over pressurizing the system. The cell upon assembly was then placed within the **Bruker Vertex 70** containing the **Pike VeeMAX III** which facilitates specular reflection of the infrared beam. Before beginning the experiment, the spectrometer was purged with nitrogen for 30-40 min's. This was done to allow the removal of atmospheric water vapor and CO<sub>2</sub>, thus preventing its influence on the IR spectra's recorded during the study.

The electrochemical analysis conducted during the study was performed at room temperature (25°C) under 5 different electrolytes which are as follows:

- Lithium Carbonate
- Sodium Bicarbonate
- Potassium Bicarbonate
- Cesium Carbonate
- C<sup>13</sup> Sodium Bicarbonate

Table 3 provides detailed information on the various electrolytes implemented during the study. The electrolyte solutions were saturated with either CO<sub>2</sub> or N<sub>2</sub> for a period of 15 min at a flow rate of 5 ml/min before each experiment. Once saturated, the gas tube was pulled out of the solution allowing CO<sub>2</sub>/N<sub>2</sub> to purge the atmosphere within the cell. During the N<sub>2</sub> saturation study, the pH of the solution doesn't change to a large extent, while a dramatic shift towards a more neutral pH is observed in the case of CO<sub>2</sub> saturation. While for the bicarbonate solution a 15 min CO<sub>2</sub> bubbling period would suffice, the carbonates require close to an hour of bubbling to achieve CO<sub>2</sub> saturation. The major acidic shift in the electrolyte can be attributed to the increased concentration of H<sup>+</sup> ions due to the following reactions:

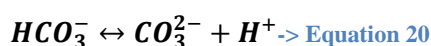


**Table 3. 1- Information regarding the electrolytes implemented during the study**

Electrolyte	Formula	Cation Radius (pm)	Solvation Radius (pm)	Molecular Weight (g/mol)	Concentration (M)	pH under CO <sub>2</sub>	pH under N <sub>2</sub>
Lithium Carbonate	Li <sub>2</sub> CO <sub>3</sub>	76	340	73.89	0.05	6.8	11.41
Sodium Bicarbonate	NaHCO <sub>3</sub>	102	276	84.0066	0.1	6.8	8.62
Potassium Bicarbonate	KHCO <sub>3</sub>	138	228	100.114	0.1	6.8	8.62
Cesium Bicarbonate	Cs <sub>2</sub> CO <sub>3</sub>	167	228	325.82	0.05	6.8	11.41
C <sup>13</sup> Sodium Bicarbonate	NaHC <sup>13</sup> O <sub>3</sub>	138	276	85.0066	0.1	-	8.62

### 3.3.1 Reduction of CO<sub>2</sub> on a palladium thin film under 0.1M KHCO<sub>3</sub>

Upon thorough preparation and setup of the experimental system, the following electrochemical - FTIR studies were performed on the palladium thin film for analysing its behaviour under the presence of 0.1M KHCO<sub>3</sub> solution:

- Activation cycle: Before beginning the electrochemical analysis on the palladium thin film, the surface is cycled 3-6 times between 0.35 V and 1.4 V under CO<sub>2</sub> saturated electrolytes in order to IR activate the surface for subsequent studies.

- Dynamic Chrono-amperometric and IR studies were performed between 0 V and -0.8 V with a step size of 0.1 V and a hold time of 10 seconds at each potential, followed by the oxidation at 1.2 V for 1min and 5 sec.
- Chrono-amperometric and IR studies were performed at -0.3 V for a period of 5 min, following which a similar study is performed at 1.2 V until complete oxidation is achieved.
- Chrono-amperometric and IR studies were performed at -0.5 V for a period of 5 min, following which a similar study is performed at 1.2 V until complete oxidation is achieved.
- Cyclic voltammetric and IR measurements were performed between -0.8 V and 1.2 V at a scan rate of 10 mVpers, with the CV's initiation and termination occurring at 0V and the scan originating in the cathodic direction.
- Cyclic voltammetric and IR measurements were performed between -0.8 V and 1.2 V at a scan rate of 2 mVpers, with the CV's initiation and termination occurring at 0 V and the scan originating in the cathodic direction.
- Chrono-amperometric and IR studies were performed at -0.8 V for a period of 5 min, following which a similar study is performed for a period of 5 min at:
  - i. 0.8 V
  - ii. 0.9 V
  - iii. 1.0 V
  - iv. 1.1 V
  - v. 1.2 V

The studies mentioned above were performed in both CO<sub>2</sub> and N<sub>2</sub> saturated 0.1 M KHCO<sub>3</sub> solutions. Each of the experiments listed above are specifically designed to enumerate upon the influence the palladium catalyst has on the reduction of CO<sub>2</sub> in combination with the resulting phenomena's observed on the palladium as well as the reduced products. The choice of KHCO<sub>3</sub> as the electrolyte for this study is stems from its use as the principle electrolyte across numerous studies.

### 3.3.2 Cationic effect on the palladium thin film affecting the CO<sub>2</sub> reduction reaction

An interesting assessment of the CO<sub>2</sub> reduction reaction on minimizing CO formation is to identify the possible modifications induced in the behaviour of palladium in the presence of varying cationic radii. Therefore a study was performed to analyse and compare the influence of lithium, sodium, potassium and cesium ions on the palladium thin films ability to reduce CO<sub>2</sub>. The following experiments were performed in order to conduct the comparative study:

- Activation cycle: Before beginning the electrochemical analysis on the palladium thin film the surface is cycled 3-6 times between 0.35 V and 1.4 V under CO<sub>2</sub> saturated electrolytes in order to IR activate the surface for subsequent studies.
- Dynamic Chrono-amperometric and IR studies were performed at 0 V to -0.8 V with a step size of 0.1 V and a hold time of 10 seconds at each potential followed by oxidation at 1.2 V for 1 min and 5 sec.
- Chrono-amperometric and IR studies were performed at -0.3 V for a period of 5 min, following which a similar study is performed at 1.2 V until complete oxidation is achieved.
- Chrono-amperometric and IR studies were performed at -0.5 V for a period of 5 min, following which a similar study is performed at 1.2 V until complete oxidation is achieved.
- Cyclic voltammetric and IR measurements were performed between -0.8 V and 1.2 V at a scan rate of 10 mVpers, with the CV's initiation and termination occurring at 0 V and the scan originating in the cathodic direction.
- Cyclic voltammetric and IR measurements were performed between -0.8 V and 1.2 V at a scan rate of 2 mVpers, with the CV's initiation and termination occurring at 0 V and the scan originating in the cathodic direction.

The studies mentioned above were performed under CO<sub>2</sub> saturation for all the electrolytes utilized.

### 3.3.3 Identification of the CO formation on the palladium surface

To confirm the influence of bicarbonate in the CO<sub>2</sub> reduction reaction, N<sub>2</sub> saturated 0.1M tracer carbon-13 NaHC<sup>13</sup>O<sub>3</sub> solution was utilized. The palladium thin film was first activated under CO<sub>2</sub> saturated 0.1M NaHCO<sub>3</sub> solution, following which the cell was drained and washed with distilled water. The cell is then filled with 8 ml 0.1M tracer carbon-13 NaHC<sup>13</sup>O<sub>3</sub> solution and bubbled with N<sub>2</sub> for a period of 15 min. The palladium thin film is then electrochemically and spectroscopically studied, by cathodically cycling once between 0 V and -0.8 V (0 V to -0.8 V to 0 V).

All FTIR measurements in this report were performed at a resolution of 4 cm<sup>-1</sup>, scan frequency of 40 Hz, optical diameter of 2.5 cm and background scan of 32. The scans collected for the cyclic voltammetric and dynamic chrono-amperometric experiments were 32 (7 sec), while for the -0.3 V and -0.5 V chrono-amperometric experiments they were 2 (0.462 sec). All potentials reported above were done with respect to the reversible hydrogen electrode (RHE) and all backgrounds for the IR measurements were recorded at 0.45V.

## IV Results

---

A crucial step encountered during research is the chronicling of oddities observed during the analysis of processed data. Therefore, this chapter focuses on meticulously detailing the various observations encountered during the investigation of the data recorded and processed during the course of the study.

Before diving into the fascinating results obtained, the following essential points are enumerated to better elucidate the results:

- ❖ The bipoalr peaks observed between 1800 cm<sup>-1</sup> and 2000 cm<sup>-1</sup> are assigned to the formation and accumulation of CO.
- ❖ All potentials described below are done with respect to the Reversible Hydrogen Electrode (RHE).
- ❖ The background IR scan for all the studies were performed at 0.45 V.
- ❖ All the IR spectra's are baseline corrected and represented in absorbance mode
- ❖ All cyclic voltammograms have been corrected for IR losses
- ❖ The palladium thin film is stable even after the activation cycle

### 4.1 Palladium Thin Film Characterization

The 15 nm palladium thin film, which is sputter deposited on the mirror polished silicon ATR crystal, presents a smooth shiny reflective surface when observed with the naked eye. The palladium thin film was also observed to peel off upon extensive electrochemical analysis on its surface.

#### 4.1.1 Electrochemical Surface area characterization

The electrochemical oxide reduction peak, as observed in figure 4.1, collected upon activation under CO<sub>2</sub> saturated 0.1M KHCO<sub>3</sub> solution is utilized to ascertain the surface area of the palladium thin film over which the reduction reactions are performed.



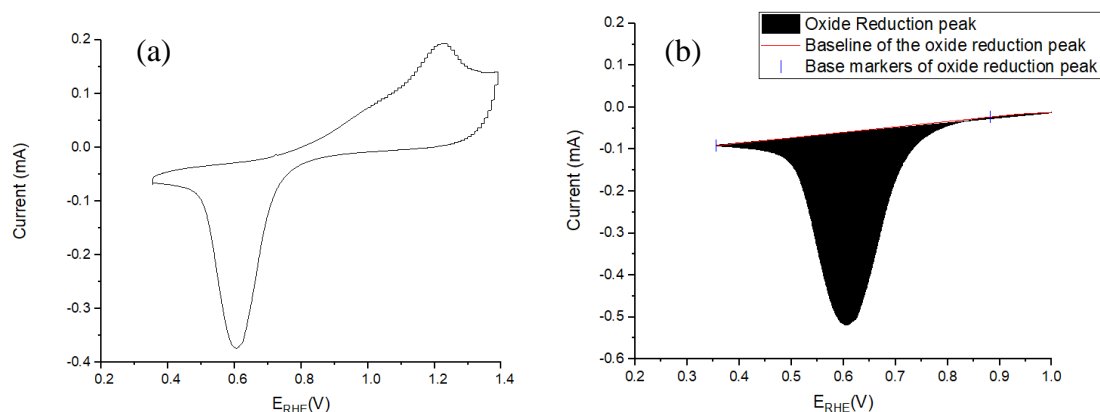


**Figure 4. 1 – (a) Cyclic Voltammogram of the activated palladium thin film between 0.35 V and 1.4 V in CO<sub>2</sub> saturated 0.1M KHCO<sub>3</sub> solution and (b) Oxide reduction peak between 0.35 V and 1.0 V as observed in (a) highlighted for surface area calculations**

The surface area of the thin film is determined by comparing it with an ideal (111) faceted palladium surface. Palladium (111) is known to have the highest packing density and the lowest surface energy, thus making it the most stable configuration for a FCC structure. Given below are the calculations for deriving the surface area of the palladium thin film -:

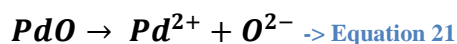
The area under the oxide reduction peak in figure 1 (b) was found to be =  **$679.5 \times 10^{-7}$  AV**.

As the cyclic voltammogram was collected at scan rate of 100 mV the total charge of observed during the reduction was found to be =  $\frac{679.5 \times 10^{-7}}{0.1} = \mathbf{679.5 \mu C}$ .

$$\text{Number of atoms in the (111) plane} = \left(\frac{1}{2} \times 3\right) + \left(\frac{1}{6} \times 3\right) = \mathbf{2}$$

$$\text{Number of atoms of palladium per unit area (N)} = \frac{2}{\frac{\sqrt{3}}{2}a^2} = \frac{2}{\frac{\sqrt{3}}{2}(3.89 \times 10^{-8})^2} = \mathbf{1.5262 \times 10^{15} \text{ atoms/cm}^2}$$

We know from the literature study that the reduction reaction goes as follows:



Thus the number of electrons (n) involved during the reaction is 2. Therefore the total charge per unit area that would be obtained from a (111) faceted surface is =

$$n \times q \times N = 1.526 \times 10^{15} \times 1.602 \times 10^{-19} \times 2 = \mathbf{489 \mu C/cm^2}$$

Thus the surface area of the activated surface area is  $= \frac{679.5}{489} = \mathbf{1.389 \text{ cm}^2}$

The geometric surface area calculated based on the diameter of the O-ring of diameter 1.3 cm within the cell  $= \pi \times \left(\frac{d}{2}\right)^2 = \pi \times \left(\frac{1.3}{2}\right)^2 = \mathbf{1.327 \text{ cm}^2}$

Comparing the surface areas calculated based on the cyclic voltammogram and that from the diameter of the O-ring, a clear understanding of the smoothness of the activated palladium thin film can be visualized.

## 4.1.2 Atomic Force Microscopy

As discussed in chapter 3, AFM analysis of the as-sputtered 15 nm palladium thin film was performed and the results are present as 2-D and 3-D images in figure 4.2 and 4.3.

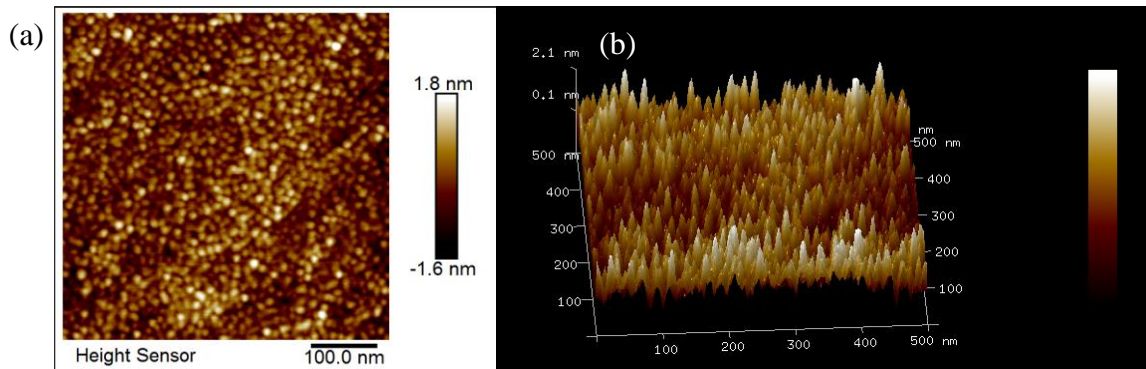


**Figure 4. 2 - AFM images of the 15nm as-sputtered palladium thin film in (a) 2-D and (b) 3-D over 500×500 nm**

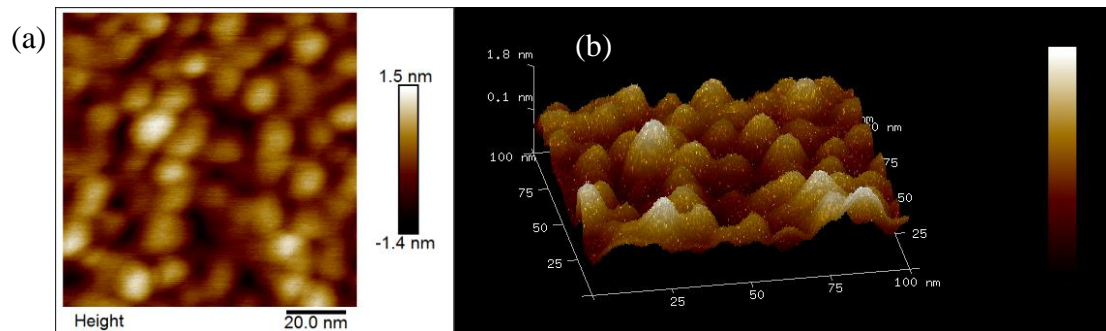


**Figure 4. 3 - AFM images of the 15nm as-sputtered palladium thin film in (a) 2-D and (b) 3-D over 100×100 nm**

The topography of the surface clearly indicates the presence of numerous island like structures over a very small area, with closer observations suggesting the initiation of coalescence on the thin film surface as seen from the surface profiles in figures 4.4 and 4.5. The island structures over the larger scan area are depicted as pointed spikes, but

viewed from the smaller scan area clearly indicate their spherical nature with these structures exhibiting an average diameter of 21.3 nm. The dark spots observed on the palladium surface can most probably be assumed to be an effect of the island structures giving rise to valleys rather than being caused due to the presence of pores on the thin film.

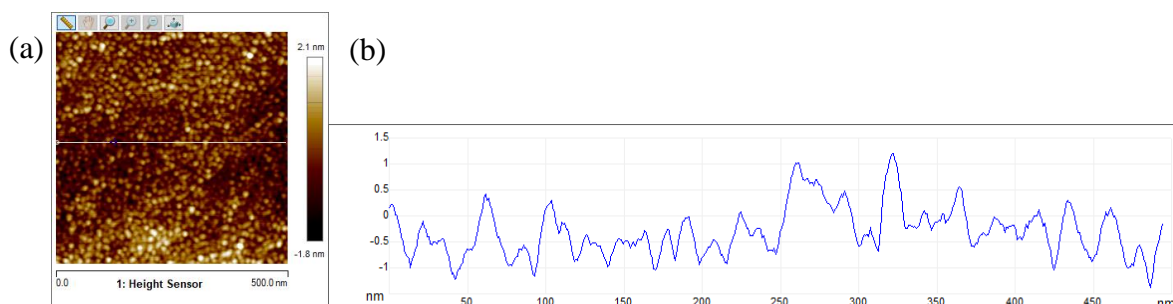


Figure 4. 4 - Surface profile of the as-sputtered palladium thin film from along the white line defined on the 500nm × 500nm AFM image

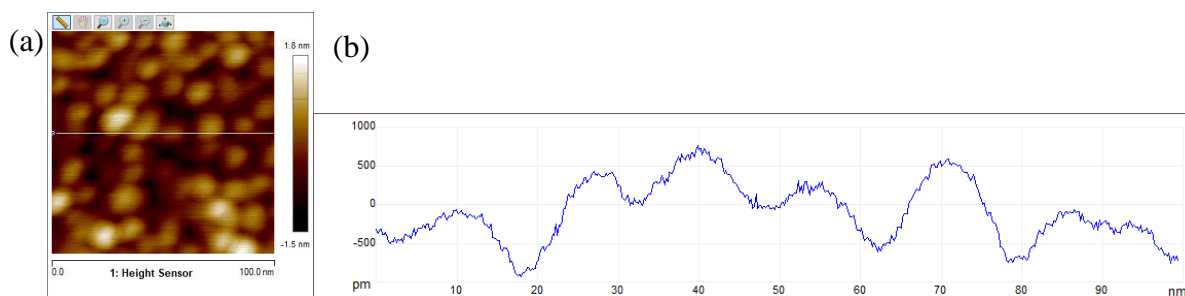
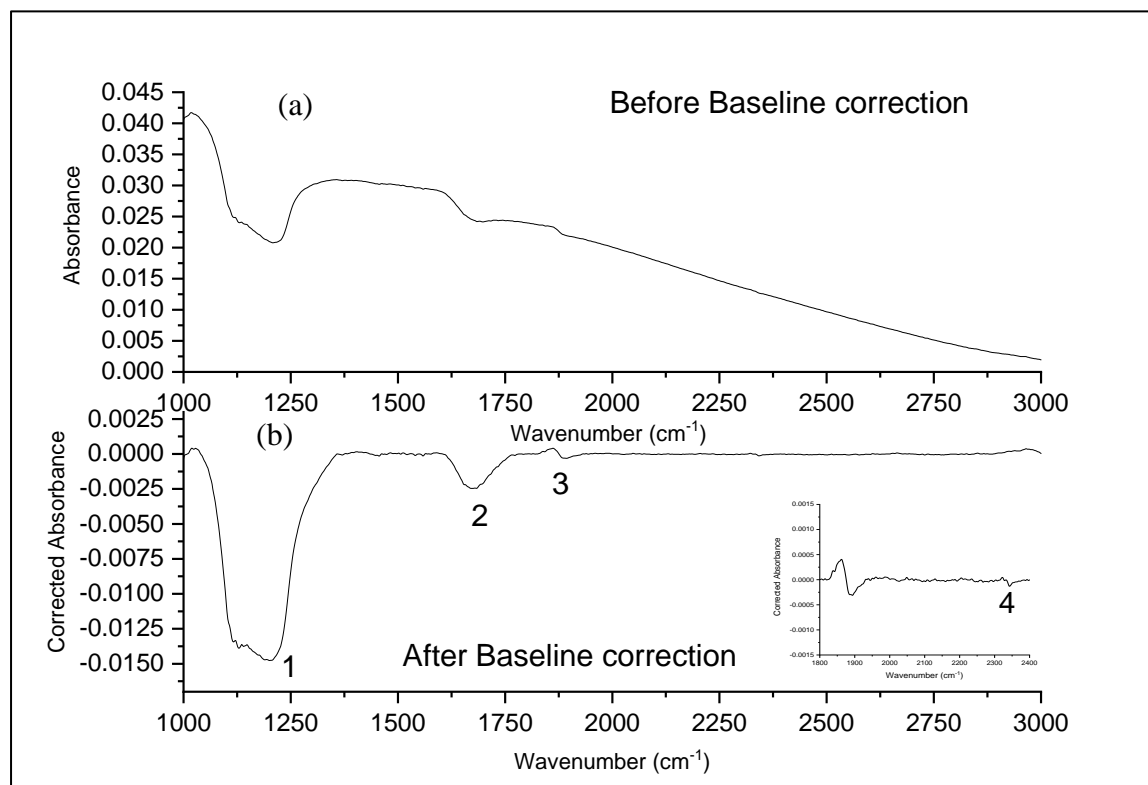


Figure 4. 5 - Surface profile of the as-sputtered palladium thin film from along the white line defined on the 100nm × 100nm AFM image

Further analysis of the AFM images through **Nanoscope Analysis** enabled the determination of certain parameters essential towards understanding the palladium thin film. The two images collected from the as-sputtered surface provides insight on certain parameters such as the average RMS roughness, kurtosis and skewness . Based on the 2 different scan sizes ( 500 nm and 100 nm) the average RMS roughness was found to be 0.511 nm, while the average kurtosis and skewness was found to be 2.93 and 0.26 respectively.

### 4.1 Reduction of CO<sub>2</sub> on the palladium thin film under 0.1M KHCO<sub>3</sub>

Once activated, the palladium thin film can be utilized to study the reactions transpiring during the reduction of CO<sub>2</sub> under the 0.1M KHCO<sub>3</sub> solution. Figure 4.6 is a representation of an IR spectrum recorded between 1000 cm<sup>-1</sup> and 3000 cm<sup>-1</sup> at -0.8 V before and after baseline correction.



**Figure 4. 6 - IR Spectra recorded between 1000 cm<sup>-1</sup> and 3000 cm<sup>-1</sup> at -0.8 V for CO<sub>2</sub> saturated 0.1M KHCO<sub>3</sub> solution on the 15 nm palladium thin film (a) Before baseline correction and (b) After baseline correction along with an inset between 1800 cm<sup>-1</sup> and 2400 cm<sup>-1</sup>**

A total of 4 peaks can be identified from the IR spectra in figure 4.6 namely:

- 1- Negative peak assigned to the vibrational frequency of SiO with a peak at 1220 cm<sup>-1</sup>
- 2- Negative peak assigned to the vibrational frequency of OH bending of water with a peak between 1600 cm<sup>-1</sup> and 1750 cm<sup>-1</sup>
- 3- Bipolar peak assigned to the vibrational frequency of CO with a peak between 1800 cm<sup>-1</sup> and 2000 cm<sup>-1</sup>
- 4- Negative peak assigned to the vibrational frequency of aqueous CO<sub>2</sub> at 2340 cm<sup>-1</sup>

The negative peaks observed during the IR spectra indicate the declining concentrations of the compound at that particular potential, with the IR spectra depicting the desorption of water and reduction of CO<sub>2</sub> at -0.8 V.

To initiate the analysis, the dynamic chrono-amprometric (CA) study was performed between 0 V and -0.8 V under CO<sub>2</sub> with the results depicted in figure 4.7. Based on the outcome of the experiment three distinct zones can be identified namely:

- Zone 1 – This zone exists between 0 V and -0.2 V, where there is an observable increase in the current with no change in the IR spectrum between 1800 cm<sup>-1</sup> and 2000 cm<sup>-1</sup>.
- Zone 2 – This zone is seen to exist between -0.3 V and -0.5 V, where the current begins to decline exponentially before attaining steady state at -0.5 V. During this period the emergence of a bipolar peak between 1800 cm<sup>-1</sup> and 2000 cm<sup>-1</sup> is noticed in the IR spectrum with the peak portraying a blue shift until -0.5 V. An interesting feature detected during this period is with regards to the area under the bipolar peak; depicting continues growth along with the peak shift.
- Zone 3 – This zone lasts till -0.8 V, where a linear increase in the current is observed. During this period the bipolar peak begins to shift towards lower frequencies, with the area under the bipolar peak gradually decreasing till -0.8 V.

Based on the position of the peak in figure 4.7(a), we can establish that the molecule formed on the palladium surface is carbon monoxide. The results obtained under tracer carbon 13 in **section 4.3** will be utilized to further justify the claim of the bipolar peak being formed due to the presence of CO. To identify the extent of peak shift during zone 3 of the study, peak centers from -0.4 V were plotted with the slope turning out to be 64.064 cm<sup>-1</sup>perV. Following the dynamic CA reduction study, the CO is electrochemically oxidized to further extract information on the phenomena occurring on the palladium surface during reduction. As the oxidation begins, a sharp drop is observed in the current followed by a broad peak with the process finally culminating at the 32<sup>nd</sup> second. During the same period, the bipolar peak depicts a constant peak center with the peak growing (appendix 1) until 9.24 secs (20th IR scan) and a slope of 0.316 cm<sup>-1</sup>, ending exactly where a maxima is observed in the current. Beyond this point the bipolar peak transforms into a positive peak, slowly diminishing with a slope of 7.804 cm<sup>-1</sup> and finally ending at 17.54 secs.

# In-Situ Infrared Spectroscopic Studies Of Palladium Thin films during CO<sub>2</sub> Electro-Reduction

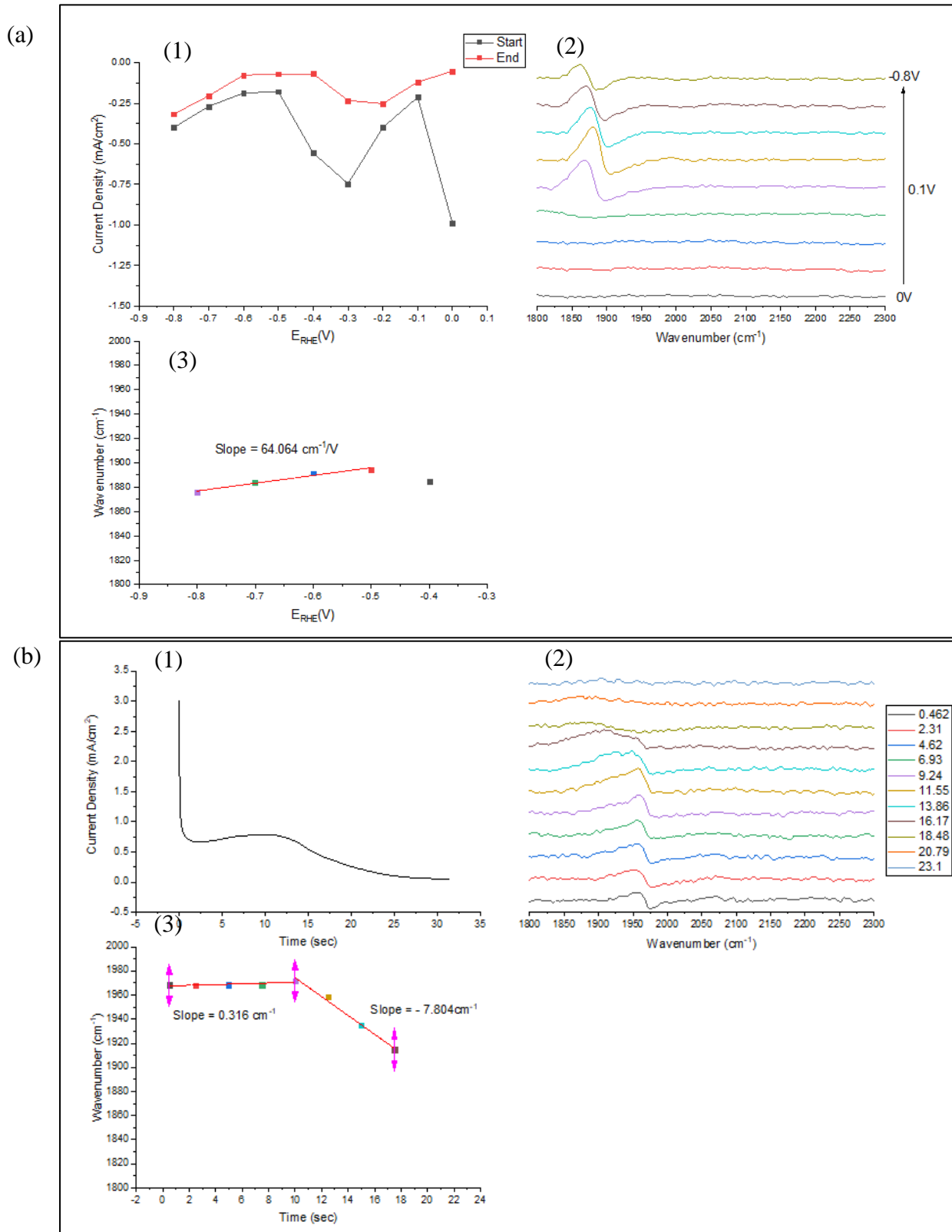


Figure 4. 7 – (a) Dynamic CA study between 0V and -0.8V under CO<sub>2</sub> with a hold time of 10 sec at each potential (1) Current density vs.  $E_{RHE}(V)$ , (2) IR spectra plotted between 0V and -0.8V from 1800 cm<sup>-1</sup> and 2300 cm<sup>-1</sup> with a least count of 0.1V and (3) Wavenumber (cm<sup>-1</sup>) Vs.  $E_{RHE}(V)$  and (b) Desorption profile for the dynamic CA study at 1.2V (1) Current density vs. Time(sec), (2) IR spectra plotted between 0 and 50 from 1800 cm<sup>-1</sup> and 2300 cm<sup>-1</sup> with a least count of 5 and (3) Wavenumber (cm<sup>-1</sup>) Vs. Time (sec)

In a bid to understand the relationship between CO and the palladium thin film, the dynamic CA study was repeated and upon completion the solution was bubbled with N<sub>2</sub> for a period of 5 min. The IR spectrum displayed in figure 4.8, clearly indicates negligible change in the position and the area of the CO peak over the 5 min period.

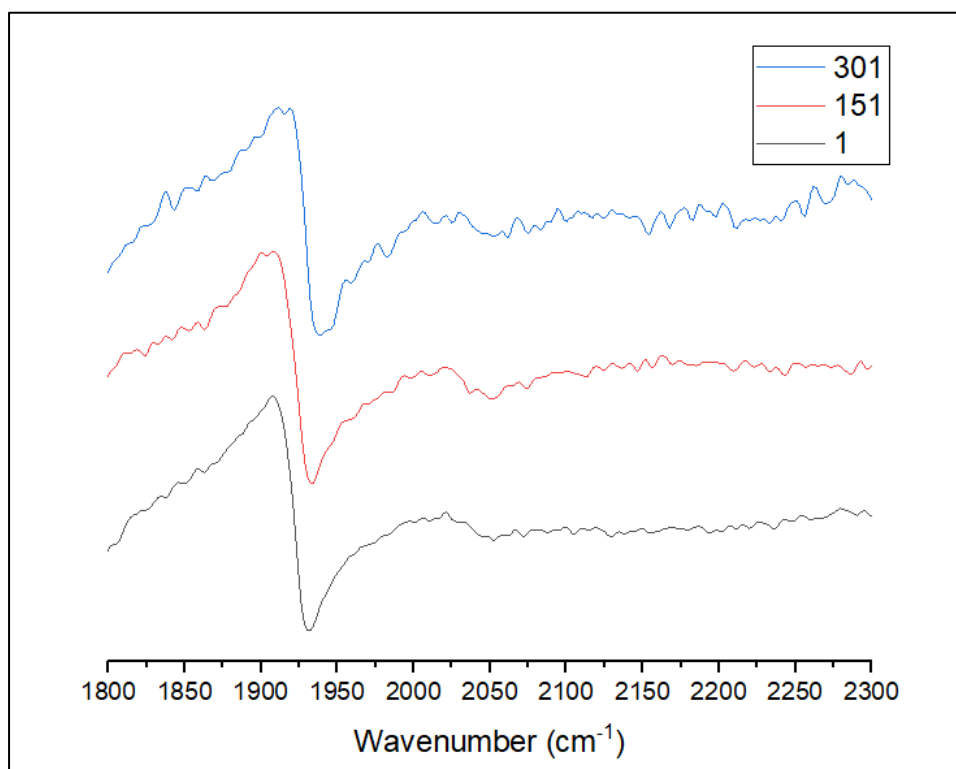


Figure 4. 8 - IR spectra recorded during N<sub>2</sub> bubbling of the CO<sub>2</sub> saturated 0.1M KHCO<sub>3</sub> solution for 5 min after the dynamic CA study recorded between 1 and 301 from 1800 cm<sup>-1</sup> and 2300 cm<sup>-1</sup> with a least count of 150

Based on the results obtained during the dynamic CA study, 2 additional CA studies were performed at -0.3 V and -0.5 V to further enumerate upon the various phenomena's occurring during the reduction reaction. Figure 4.9 depicts the results obtained during the -0.3 V CO<sub>2</sub> CA study performed on the palladium thin film. During the -0.3 V 5 min reduction study, the bipolar peak is seen to shift exponentially until 46.2 secs (100<sup>th</sup> IR measurement), where the system is seen to attain pseudo steady state. CO formation is seen to continue beyond this point but, at a lower rate as observed by the shift in the peak center. The area under the bipolar peak is also seen to increase, but unlike the previous case it achieves stability at about 184.6 sec (appendix 2) (400<sup>th</sup> IR measurement); exactly where the current also seem to achieve stability. Upon completion of the CA, the CO formed is electrochemically oxidized with complete oxidation occurring within 2.31 sec as per the IR spectra. Unlike the previous case, the oxidation begins directly from the positive peak, with its area initially increasing, decreasing and finally vanishing as the oxidation reaction proceeds. The CA also depicts immediate oxidation of CO with the current achieving maximum at the point of complete oxidation.



## In-Situ Infrared Spectroscopic Studies Of Palladium Thin films during CO<sub>2</sub> Electro-Reduction

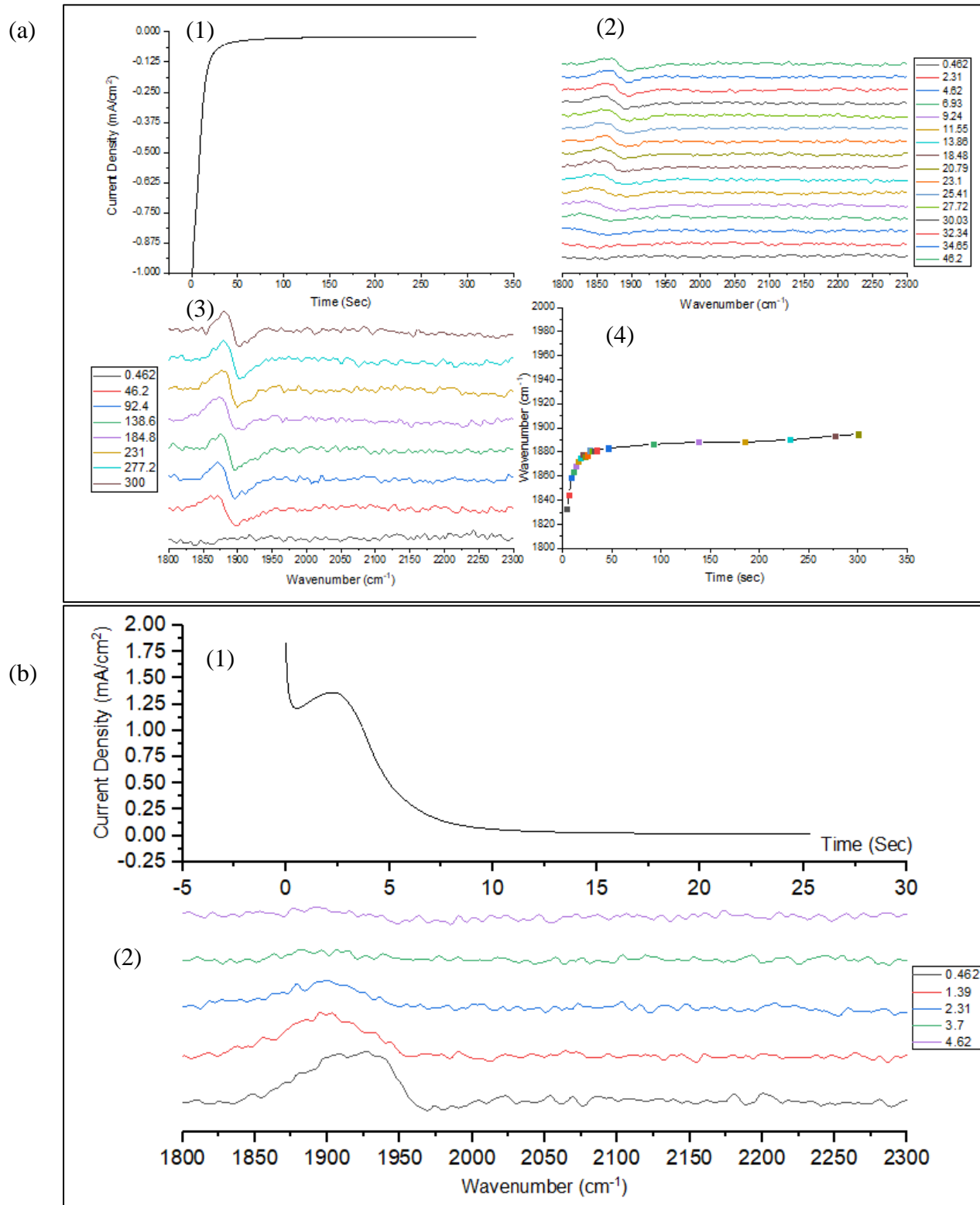
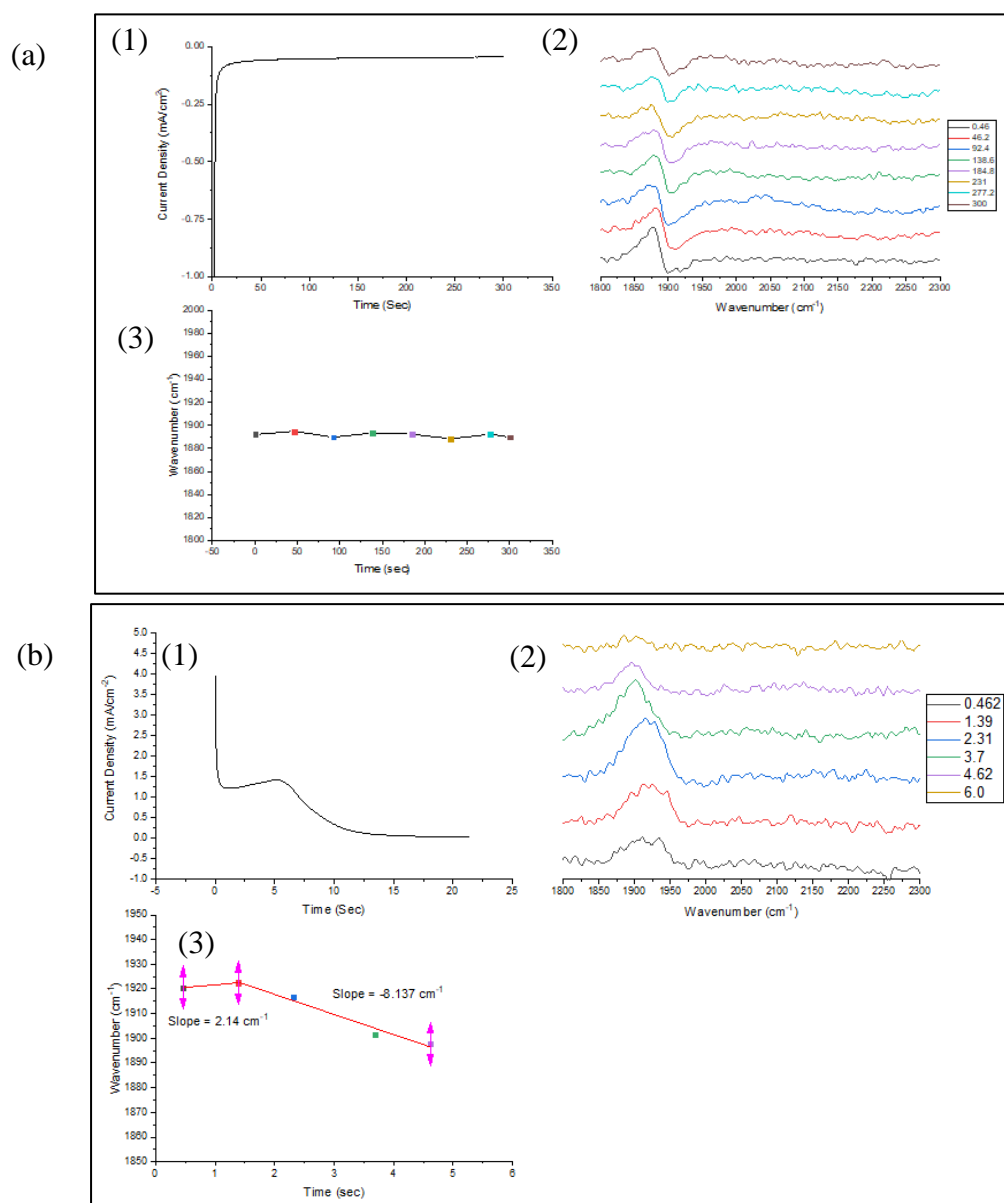


Figure 4.9 – (a) -0.3 V CA study under CO<sub>2</sub> for a period of 5 min (1) Current density vs. Time (sec), (2) IR spectra plotted between 0.462 and 46.2 sec from 1800 cm<sup>-1</sup> and 2300 cm<sup>-1</sup>, (3) IR spectra plotted between 0.462 and 300 sec from 1800 cm<sup>-1</sup> and 2300 cm<sup>-1</sup> and (4) Wavenumber (cm<sup>-1</sup>) Vs. Time (sec) and (b) Desorption profile for the -0.3 V CA study at 1.2V (1) Current density vs. Time(sec) and (2) IR spectra plotted between 0.462 and 4.62 from 1800 cm<sup>-1</sup> and 2300 cm<sup>-1</sup>

Moving on to the -0.5 V CA study, CO formation occurs instantaneously based on the results published in figure 4.10. Unlike in the case of -0.3 V, the current also seems to reach steady state immediately. Furthermore, the bipolar peak centers remain constant at about  $1890\text{ cm}^{-1}$ , with the area decreasing under the bipolar peak up till 400 ( appendix 3). The oxidation of CO is seen to take slightly longer, 4.62 sec, with the regular behavior of the bipolar peak observed as in the case of the dynamic CA study. The slope of the constant regime was found to be  $2.14\text{ cm}^{-1}$ , while the reduction regime depicted a slope of  $8.137\text{ cm}^{-1}$ . The relation between the CA and the oxidation peak is similar to that observed under -0.3 V, with a slight delay in achieving the maximum current value.



**Figure 4. 10 - (a) -0.5 V CA study under CO<sub>2</sub> for a period of 5 min (1) Current density vs. Time (sec), (2) IR spectra plotted between 0.462 and 300 sec from  $1800\text{ cm}^{-1}$  and  $2300\text{ cm}^{-1}$  and (3) Wavenumber ( $\text{cm}^{-1}$ ) Vs. Time (sec) and (b) Desorption profile for the -0.5 V CA study at 1.2V (1) Current density vs. Time (sec), (2) IR spectra plotted between 0.462 and 6 sec from  $1800\text{ cm}^{-1}$  and  $2300\text{ cm}^{-1}$  and (3) Wavenumber( $\text{cm}^{-1}$ ) vs. Time (sec)**

To further analyze the evolution of the reduction reaction over the palladium thin film, cyclic voltammetric studies at 10 and 2 mVpers were performed. The results of the 10 mVpers study are displayed in figure 4.11.

The CV study begins in the cathodic direction upto -0.8 V, followed by the reverse scan till the anodic potential of 1.2 V with the study finally culminating at 0 V. Contradictory to the dynamic CA study, the 10 mVpers CV depicts an exponential drop in the current at -0.2 V concurrent with the initiation of CO formation on the palladium surface. The current is seen to exponentially drop until -0.4 V, after which it increases linearly. Simultaneously the bipolar peak depicts a blue shift with regards to the peak center until -0.4 V, followed by a red shift until -0.7 V at a rate of 50.395 cm<sup>-1</sup>perV. Coupled with the peak center shift, the peak area also grows until -0.4 V, subsequently decreasing and stabilizing at -0.7 V during the reverse cathodic scan. As the potential reverses at -0.8 V, the bipolar peak center observably shifts back in the positive direction (towards higher wavenumbers) with the slope of the shift found to be 57.79 cm<sup>-1</sup>perV. This trend in the peak center is seen to continue until 0.7 V, with a slope of 39.11 cm<sup>-1</sup>perV in the anodic region.

Beyond 0.7 V, oxidation of the bound CO commences with completion achieved at 1.0 V at a rate of 251.4273 cm<sup>-1</sup>perV. Along with the peak center shift occurring beyond 0.7 V, a similar shift in the peak area, as in previous oxidation experiments, is detected. The peak area is seen to increase at 0.8 V, synonymous to the peak center shift, with the area subsequently diminishing until complete oxidation is achieved. An interesting mechanism was noticed during the oxidation of CO in that at 0.7 V and 0.8 V the peak centers remained constant while an increase in the peak area occurred. Concurrently, the 10 mVpers CV presents the oxidation peak initiation at about 0.5 V with the peak centers of the 2 convoluted peaks observed at 0.9 V and 1.1 V. Although CO oxidation is observed to culminate at 1.0 V, there still exist reactions occurring on the surface as denoted by the current values beyond the potential. The forward anodic scan showcases no current in between 0 V and 0.4 V with the reverse anodic scan presenting a peak between 0.9 V and 0.5 V.

# In-Situ Infrared Spectroscopic Studies Of Palladium Thin films during CO<sub>2</sub> Electro-Reduction

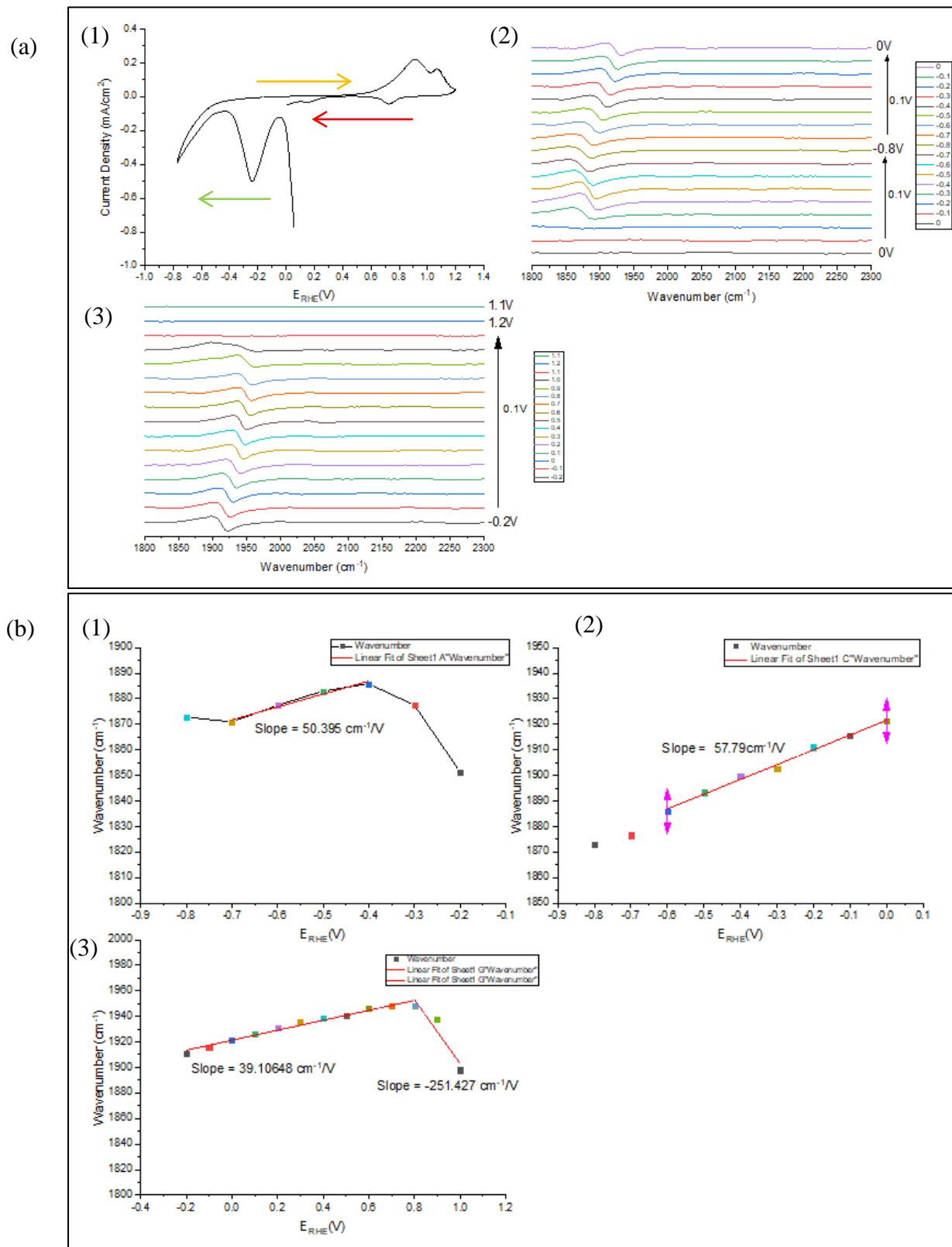


Figure 4. 11 - (a) 10 mVpers CV study under CO<sub>2</sub> between -0.8 V and 1.2 V with 0 V as the mid-point (1) Current density Vs.  $E_{RHE}(V)$ , (2) IR spectra plotted from 0 V to -0.8 V to 0V from 1800  $cm^{-1}$  and 2300  $cm^{-1}$  with a least count of 0.1 V and (3) IR spectra plotted from -0.2 V to 1.2 V to 1.1 V from 1800  $cm^{-1}$  and 2300  $cm^{-1}$  with a least count of 0.1 V and (b) Wavenumber( $cm^{-1}$ ) Vs.  $E_{RHE}$  for the 10 mVpers CV study (1) -0.2 V to -0.8 V, (2) -0.8 V to 0 V and (3) -0.2 V to 1.0 V

In contrast to the 10 mVpers CV study, the 2 mVpers study presents a slight shift in the CO initiation potential with the reaction originating at -0.3 V as depicted in figure 4.12 . The IR spectrum was found not corroborating this claim, with the initiation of the bipolar peak occurring at -0.4 V. As in the 10 mVpers study, the reduction in the current extends until -0.4 V with the peak area of the former being greater in comparison to the latter. The shift in the peak centers are similar to the ones observed under the 10 mVpers study, with the slopes of the 4 regimes being:

- -0.5 V to -0.8 V =  $57.606 \text{ cm}^{-1}\text{perV}$  (Forward Cathodic Scan)
- -0.8V to 0 V =  $58.52 \text{ cm}^{-1}\text{perV}$  (Reverse Cathodic Scan)
- 0 V to 0.5 V =  $58.66 \text{ cm}^{-1}\text{perV}$  (Forward Anodic Scan)
- 0.5 V to 1 V =  $99.47 \text{ cm}^{-1}\text{perV}$  ( CO oxidation domain)

Unlike the other cases, the bipolar peak area marginally reduces from -0.4 V attaining stability by -0.6 V. Contrary to the 10 mVpers study, absence of variations in the peak area until initiation of oxidation is noticed during the 2 mVpers study. The oxidation study depicts a usual pattern beginning with the conversion of the bipolar peak into a positive peak, followed by the reduction in peak area with the peak finally vanishing at 1.0 V. This increase in the peak area is observed to occur from 0.7 V , attaining a maxima at 0.8 V and disappearing at 1.0 V. This transformation in the bipolar peak center and peak form is synchronous with the oxide peak initiation and development on the CV. Assessing the oxidation regime based on the data observed from the IR spectra showcases an increase in the current at 0.5 V, verifying initiation of CO oxidation .

Unlike the previous case, the oxidation regime portrays the presence of 2 separate and well defined peaks at 0.7 V and 1.0 V. The rate of CO oxidation during the 2 mVpers study is lower than that observed during the 10 mVpers study, suggestive of a rate limiting step existing during the initiation of the CO oxidation. Along with the above mentioned differences, the 2 CV's also share certain similarities in that the forward anodic scan showcases no current between 0 V and 0.5 V along with the existence of a current beyond the CO oxidation potential and a peak during the reverse cathodic scan between 0.9 V and 0.6 V.

# In-Situ Infrared Spectroscopic Studies Of Palladium Thin films during CO<sub>2</sub> Electro-Reduction

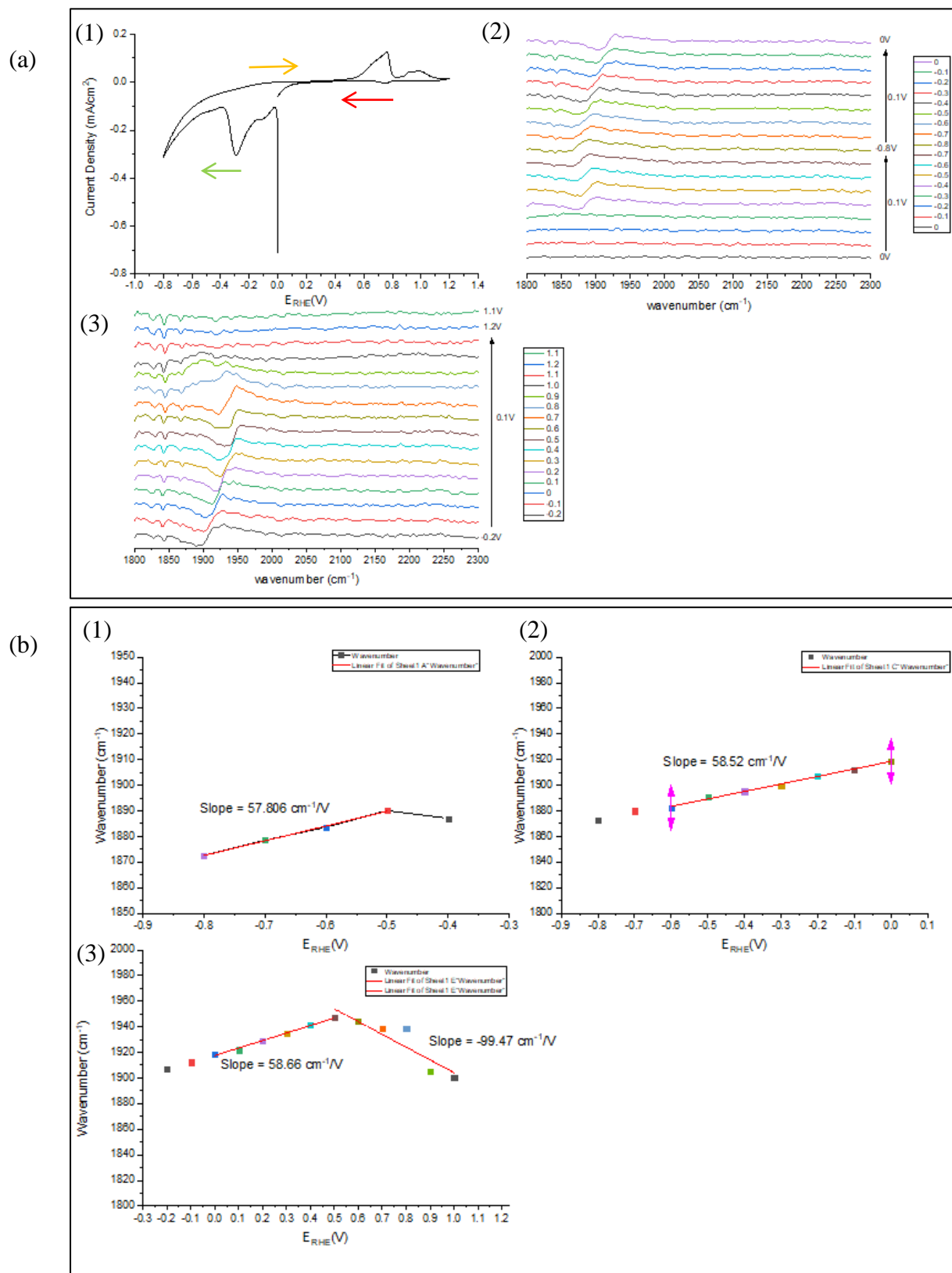
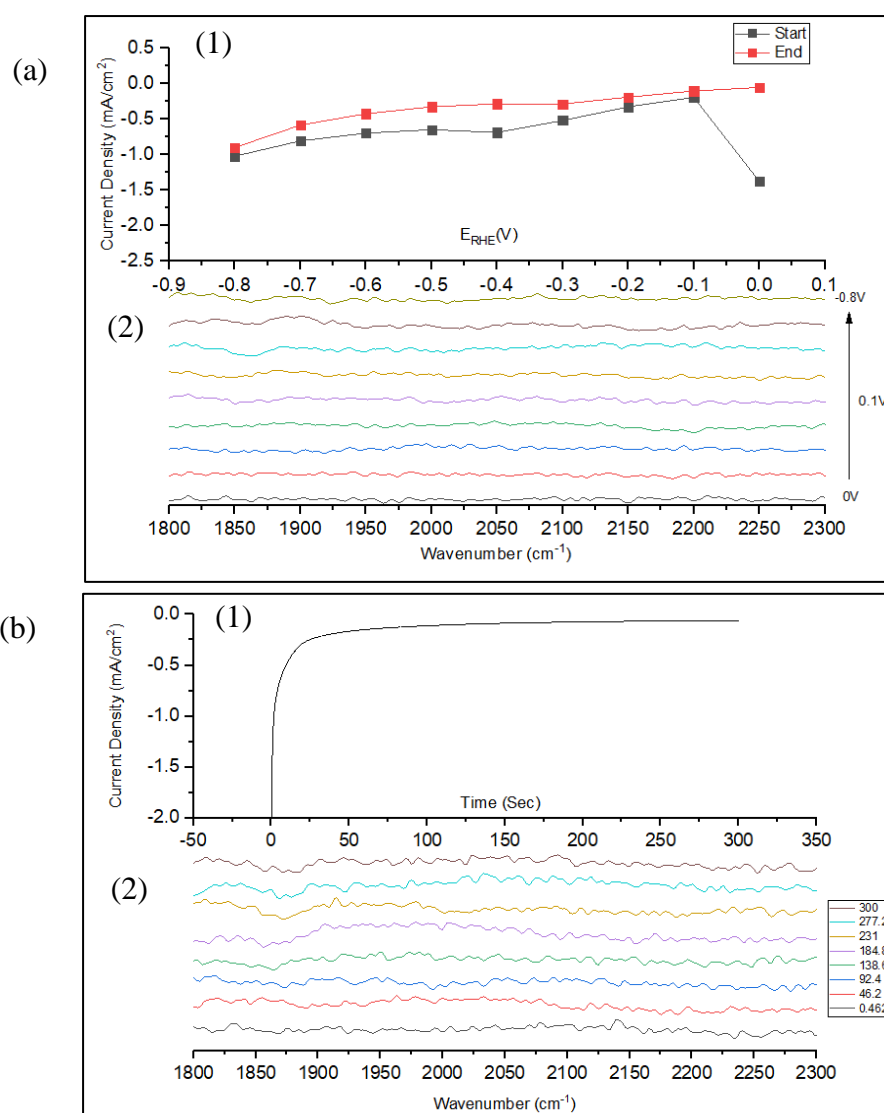


Figure 4. 12 - (a) 2 mVpers CV study under CO<sub>2</sub> between -0.8 V and 1.2 V with 0 V as the mid-point (1) Current density vs.  $E_{RHE}(V)$ , (2) IR spectra plotted from 0 V to -0.8 V to 0 V from 1800  $cm^{-1}$  and 2300  $cm^{-1}$  with a least count of 0.1 V and (3) IR spectra plotted from -0.2 V to 1.2 V to 1.1 V from 1800  $cm^{-1}$  and 2300  $cm^{-1}$  with a least count of 0.1 V and (b) Wavenumber ( $cm^{-1}$ ) vs.  $E_{RHE}$  for the 2 mVpers CV study (1) -0.2 V to -0.8 V, (2) -0.8 V to 0 V and (3) -0.2 V to 1.0 V

Although the study of CO<sub>2</sub> reduction under saturated conditions is essential, understanding mechanisms occurring under CO<sub>2</sub> deficient environments is paramount towards obtaining a holistic understanding of the palladium-CO<sub>2</sub> reaction system. Given that numerous studies have observed pH variations transpiring during the course of the reduction reaction, experiments similar to those performed under CO<sub>2</sub> are conducted under N<sub>2</sub> in a bid to assess the effects this modification has on the electrochemical reduction of CO<sub>2</sub>. While both the dynamic CA as well as the -0.3 V CA don't indicate any deviations, electrochemically as well as spectroscopically, the -0.5 V CA does show slight proclivity towards the formation of CO with the spectra showing minimal bipolarity between 1800 cm<sup>-1</sup> and 2000 cm<sup>-1</sup>. Simultaneously the current depicts a delayed achievement of stability, as is illustrated in figure 4.14.



**Figure 4.13 - (a) Dynamic CA study under N<sub>2</sub> between 0 V and -0.8 V with a hold time of 10 sec at each potential (1) Current density vs. E<sub>RHE</sub> (V) and (2) IR spectra plotted between 0 V and -0.8 V from 1800 cm<sup>-1</sup> and 2300 cm<sup>-1</sup> with a least count of 0.1 V and (b) -0.3 V CA study under N<sub>2</sub> for a period of 5 min (1) Current density vs. Time(sec) and (2) IR spectra plotted between 0.462 sec and 300 sec from 1800 cm<sup>-1</sup> and 2300 cm<sup>-1</sup>**



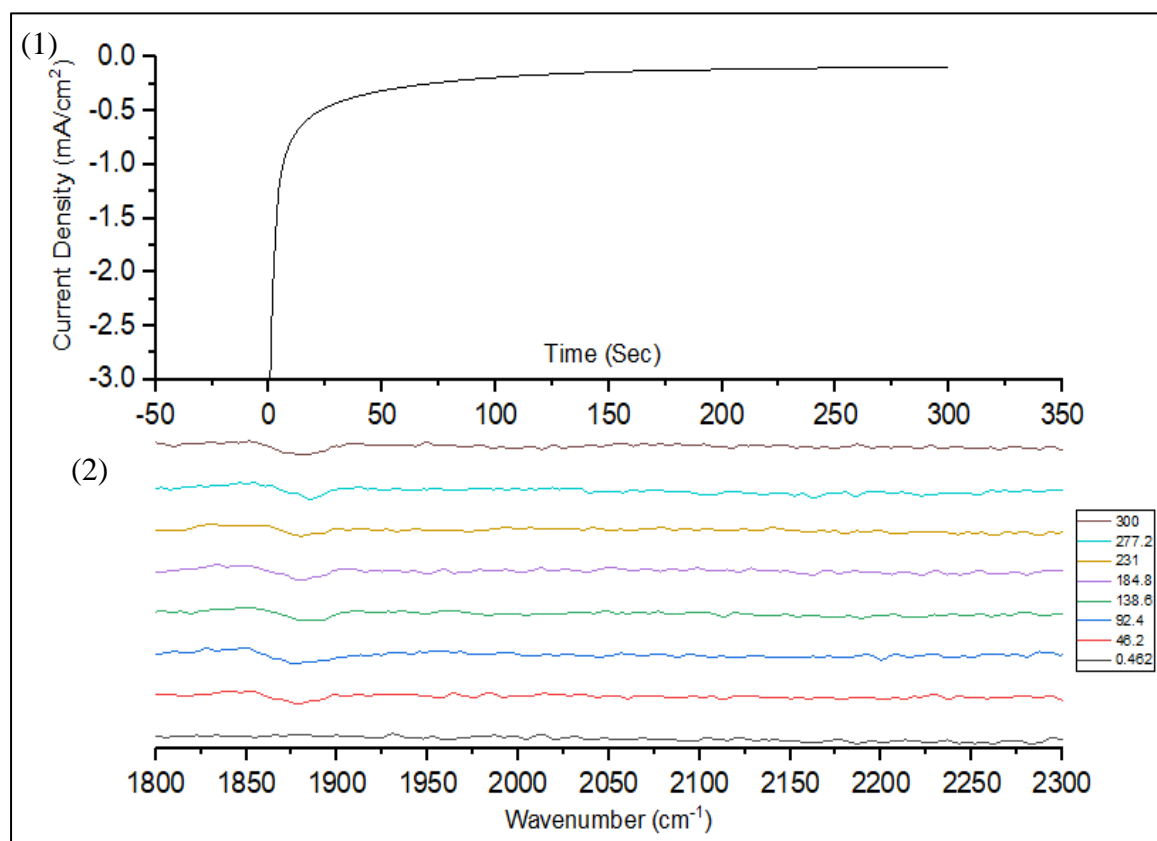


**Figure 4. 14 -0.5V CA study under N<sub>2</sub> for a period of 5 min (1) Current density Vs. Time (sec) and (2) IR spectra plotted between 0.462 and 300 sec from 1800 cm<sup>-1</sup> and 2300 cm<sup>-1</sup>**

Following the CA studies, CV at 10 and 2 mVpers were performed under N<sub>2</sub>, similar to those conducted under CO<sub>2</sub>. The 10 mVpers study, presented in figure 4.15, depicts an exponential increase in the current, with CO formation occurring at -0.7 V during the reverse cathodic scan as per the IR spectra recorded. Unlike previous cases, the initiation of CO doesn't depict any red shift in the peak centers during the cathodic scan of the CV. As the potential backtracks to 0 V in the cathodic regime, the hysteresis in the current increases with the bipolar peak center shift occurring at a rate of 62.671 cm<sup>-1</sup>perV. Along with the shift in the peak center, the area under the bipolar peak also grows until 0V in the cathodic regime. Upon entering the anodic regime, the presence of four convoluted peaks within the CV is noticed with the first broad peak extending from 0 V to 0.6 V, the second between 0.6V to 0.8V, the third between 0.8 V and 0.9 V and the final between 0.9 V and 1.2 V. The reverse anodic scan depicts a peak between 0.9 V and 0.5 V, similar to that observed during the CO<sub>2</sub> CV studies. The emergence of the second peak coincides with the increase in the bipolar peak area at 0.6 V, transforming into the positive peak at 0.8 V with the peak finally vanishing at 1.1 V. The shift in the peak center between 0 and 0.8 V took place at a rate of 32.871 cm<sup>-1</sup>perV, while the oxidation occurred at a rate of 107.349 cm<sup>-1</sup>perV. Similar to the trends observed during the CO<sub>2</sub> CV studies, the peak area is observed to increase at 0.7 V, attaining maxima at 0.8 V and subsequently fading away until 1.1V.

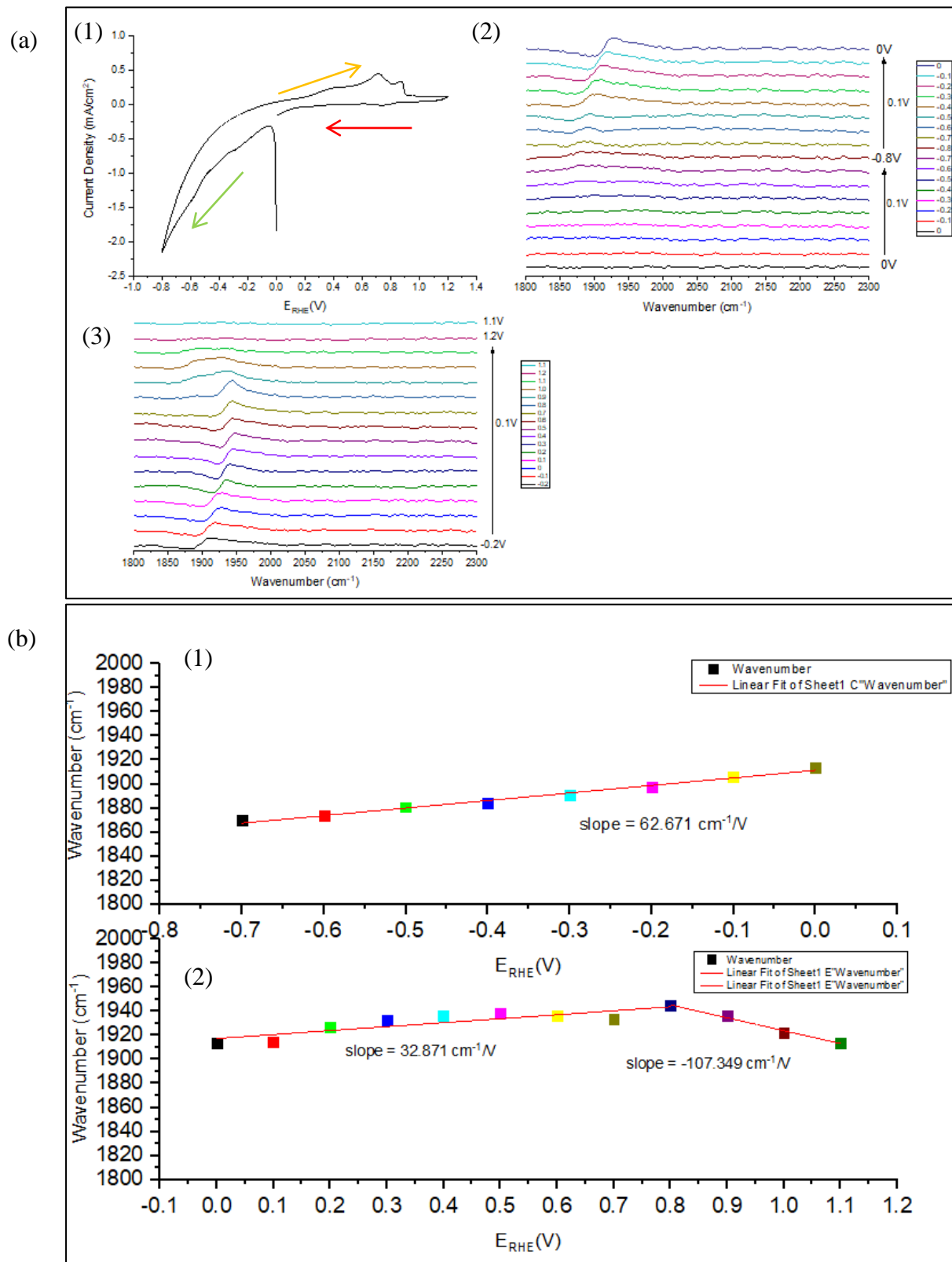


**Figure 4. 15 - (a) 10 mVpers CV study under N<sub>2</sub> between -0.8 V and 1.2 V with 0 V as the mid-point (1) Current density vs. E<sub>RHE</sub>(V), (2) IR spectra plotted from 0 V to -0.8 V to 0V from 1800 cm<sup>-1</sup> and 2300 cm<sup>-1</sup> with a least count of 0.1 V and (3) IR spectra plotted from -0.2 V to 1.2V to 1.1 V from 1800 cm<sup>-1</sup> and 2300 cm<sup>-1</sup> with a least count of 0.1 V and (b)Wavenumber(cm<sup>-1</sup>) vs. E<sub>RHE</sub> (V) for the 10 mVpers CV study under N<sub>2</sub> (1) -0.7 V to 0 V, (2) -0.2 V to 1.1 V**

The reduction in the scan rate from 10 mVpers to 2 mVpers demonstrates a variation in the cyclic voltammogram and IR spectra from that of the former, as noticed upon comparing figure 4.16 (2 mVpers) with figure 4.15 (10 mVpers). The reduction in the current coupled with the hysteresis observed in the cathodic section is greater in comparison to that observed in the 10 mVpers CV. In comparison to the CO<sub>2</sub> saturated CV's, both the N<sub>2</sub> saturated CV studies showcase larger cathodic currents and reduced current drops; suggestive of differences arising with respects to the reaction rates occurring at these varying condition on the palladium surface.

The inception of the cathodic scan as in the case of the 2 mVpers CO<sub>2</sub> study, exhibits 2 convoluted peaks initiating at 0 V and -0.15 V respectively. The inception of the current drop occurs at -0.3 V, with the bipolar peak initiating at -0.4 V; a point on the CV where the current in the forward cathodic scan is the lowest. As the potential study continues, the bipolar peak center exhibits a similar pattern, with an initial decrease between -0.5 V and -0.8 V at a rate of 57.81 cm<sup>-1</sup>perV followed by an increase until 0.6V at a rate of 58.52 cm<sup>-1</sup>perV(-0.8V to 0V) and 58.66 cm<sup>-1</sup>perV(0V to 0.6V) respectively. The oxidation of CO begins at 0.6 V and culminates at 1.0 V, with the frequency exhibiting a red shift coupled with the usual oxidation trends noticed during the course of the study. The desorption rate is found to follow a similar trend as to that observed under CO<sub>2</sub> upon reduction of the scan rate, with comparison amongst identical scan rates across gasses showcasing drastic/similar variations in its value.

Contradicting the 10 mVpers CV studies under CO<sub>2</sub> and N<sub>2</sub> and the 2 mVpers study under CO<sub>2</sub>, CO oxidation under the CV is observed to originate at 0.3 V with the presence of a large peak between 0.3 V and 0.8 V and a small peak between 0.8 V and 1.0 V. Along with differences there also exist a few similarities between the CV's in that the forward anodic scan showcases the absence and presence of current before/after the initiation/culmination of CO oxidation with the reverse anodic scan presenting a peak in between 0.9 V and 0.5 V.

# In-Situ Infrared Spectroscopic Studies Of Palladium Thin films during CO<sub>2</sub> Electro-Reduction

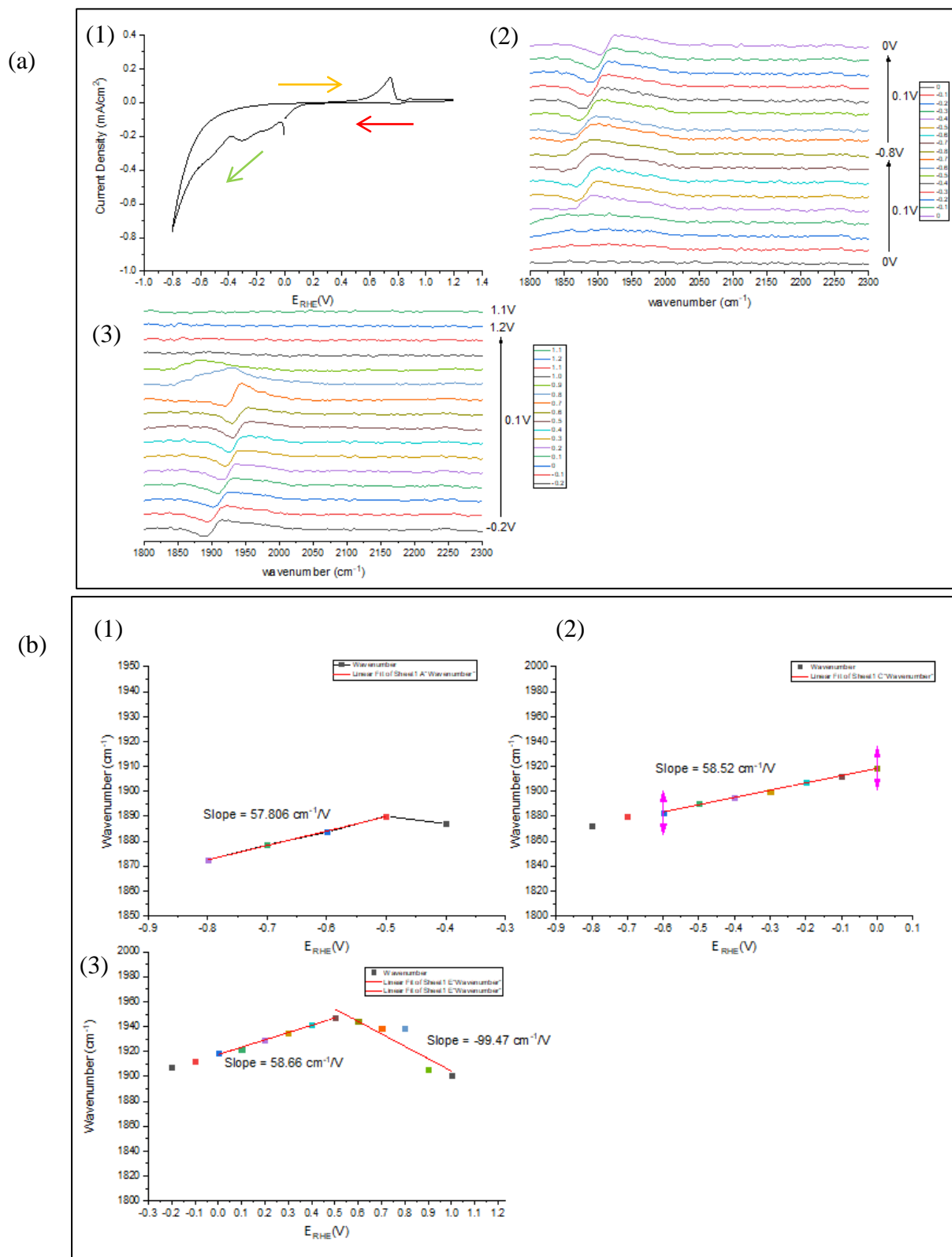


**Figure 4. 16 - (a) 2 mVpers CV study under N<sub>2</sub> between -0.8 V and 1.2 V with 0 V as the mid-point (1) Current density vs.  $E_{RHE}$  (V), (2) IR spectra plotted from 0 V to -0.8 V to 0 V from 1800  $\text{cm}^{-1}$  and 2300  $\text{cm}^{-1}$  with a least count of 0.1 V and (3) IR spectra plotted from -0.2 V to 1.2 V to 1.1 V from 1800  $\text{cm}^{-1}$  and 2300  $\text{cm}^{-1}$  with a least count of 0.1 V and (b) Wavenumber ( $\text{cm}^{-1}$ ) vs.  $E_{RHE}$  (V) for the 2 mVpers CV study under N<sub>2</sub> (1) -0.2 V to -0.8 V, (2) -0.8 V to 0 V and (3) -0.2 V to 1.0 V**

To elaborate upon the formation and accumulation of CO on the palladium thin film, desorption studies starting from 0.8 V until 1.2 V were performed with the results published in figures 4.17 and 4.18 respectively. Prior to their implementation, the palladium surface is engulfed by CO molecules by applying a reduction potential of -0.8 V in a CO<sub>2</sub> saturated 0.1M KHCO<sub>3</sub> solution. The reduction of CO<sub>2</sub> at -0.8 V leads to an instantaneous achievement of stability as observed from the current density as well as the IR spectra.

Analogous to the IR spectra observed during CO<sub>2</sub> reduction study performed under -0.5 V, the -0.8 V study showcases a decrease in the peak area with ultimate stability achieved at 150 sec. The oxidation, beginning with 0.8 V and 0.9 V, exhibits growth in the bipolar peak area with negligible shift in their peak center. The peak area under 0.8 V increases until 95.23 sec while the 0.9 V study depicts a continuous increase in its peak area over the 5 min study period.

The remainder of the potentials demonstrates a surge in the oxidation rate, with 1.0 V, 1.1 V and 1.2 V recording values of 90.47 sec, 83.329 sec and 16.67 sec respectively. The bipolar peaks of the three oxidation potentials begin as observed under 0.8 V/0.9 V, but continue on with the shift in the peak center; finally vanishing from the spectra between 1800 cm<sup>-1</sup> and 2000 cm<sup>-1</sup>. Similarly, the peak areas also increase initially following which they decrease and eventually vanish indicating complete CO oxidation.

Inter-connected, the shift in peak potential and the area reduction appear to begin simultaneously, as is the case throughout the study. Although the 3 show similar area trends, the initiation of the increase seems delayed while considering the case under 1.2 V, suggestive of a possible blockade towards the oxidation of CO. The current densities at each of the oxidation potentials achieve stability within 60 sec, with each depicting a unique trend. While 0.8 V CA shows the absence of a peak, the others do so with the area under the peak increasing with increasing oxidation potentials.

# In-Situ Infrared Spectroscopic Studies Of Palladium Thin films during CO<sub>2</sub> Electro-Reduction

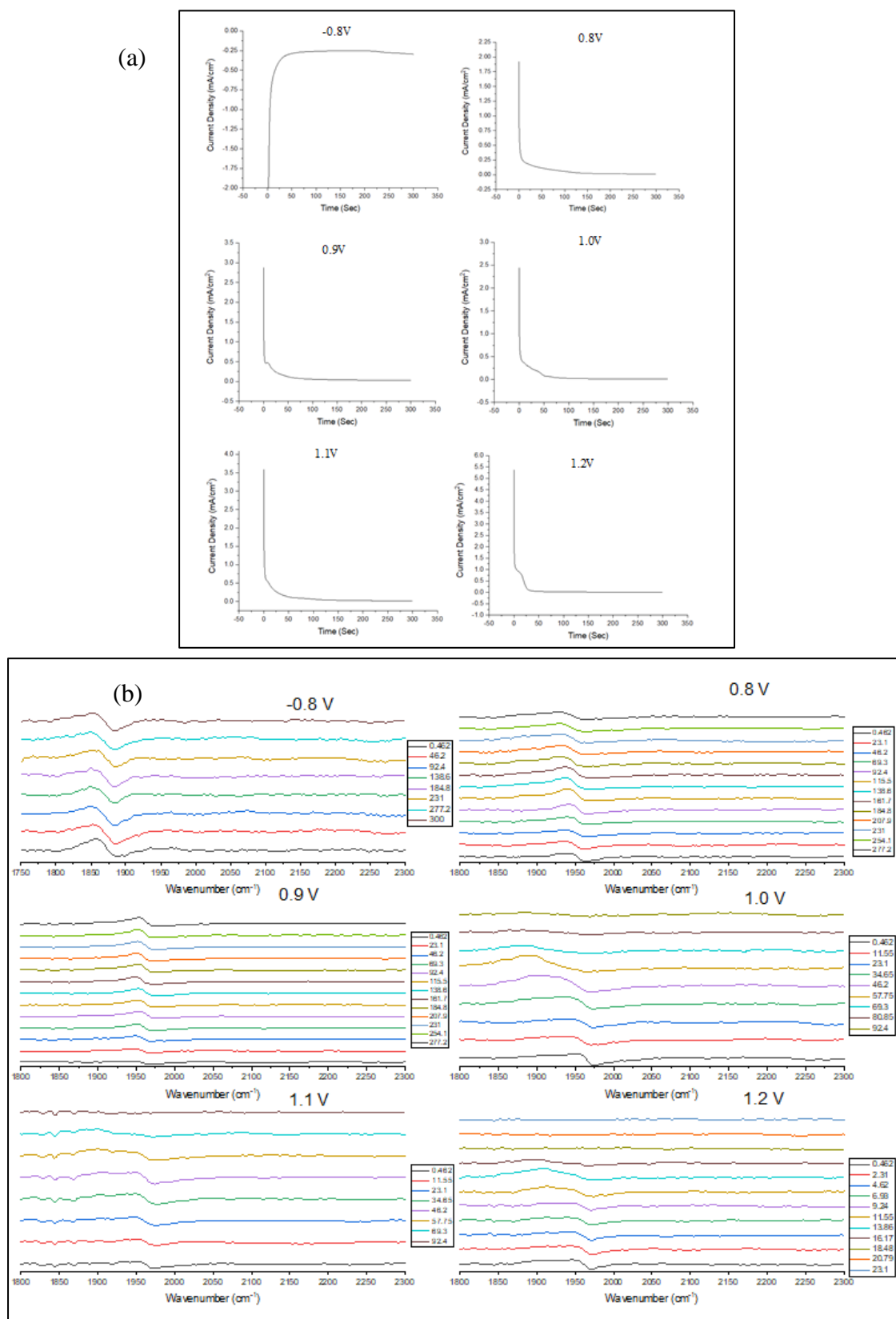


Figure 4. 17 - (a) Current density Vs. Time (sec) for the 5 min reduction study at -0.8 V and 5 min desorption study at 0.8 V, 0.9 V, 1.0 V, 1.1 V and 1.2 V and (b) IR spectra recorded during the 5 min reduction study at -0.8 V and the desorption study until the end of the 5<sup>th</sup> min or the complete oxidation of CO at 0.8 V, 0.9 V, 1.0 V, 1.1 V and 1.2 V.

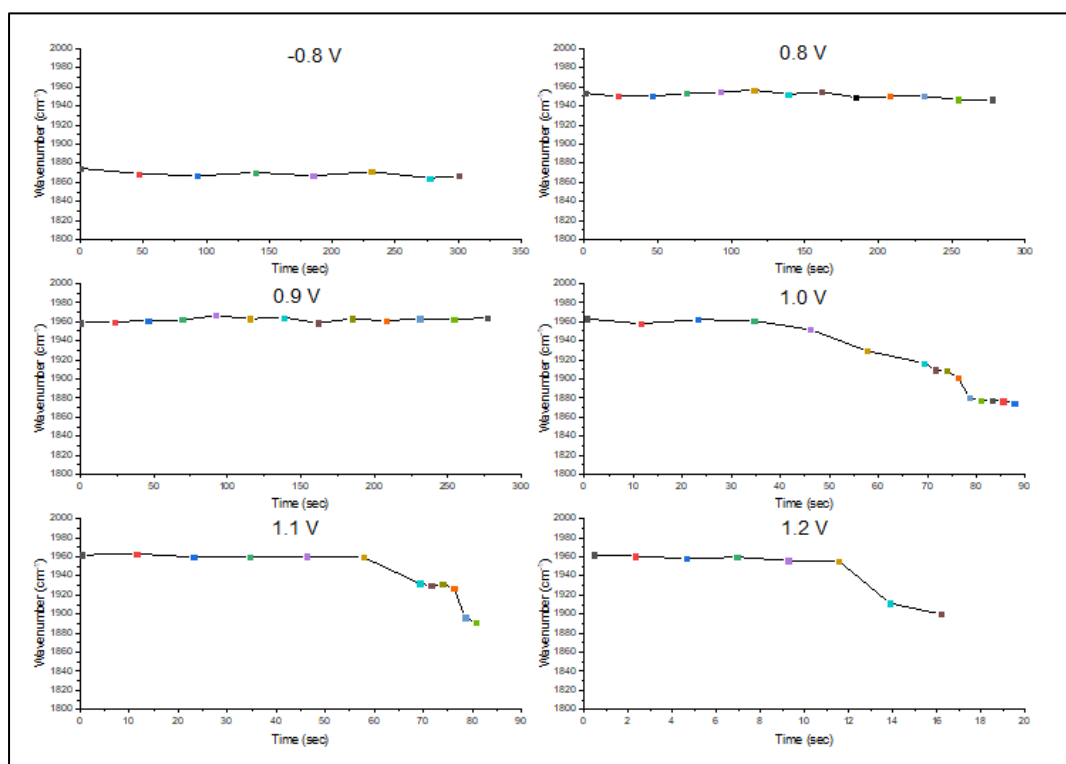


Figure 4. 18 – Wavenumber (cm<sup>-1</sup>) Vs. Time (sec) for the 5 min reduction study at (1) 0.8 V and the 5 min desorption study at (2) 0.8 V, (3) 0.9 V, (4) 1.0 V, (5) 1.1 V and (6) 1.2 V

### 4.2 Cationic effect on the palladium thin film affecting the CO<sub>2</sub> reduction reaction

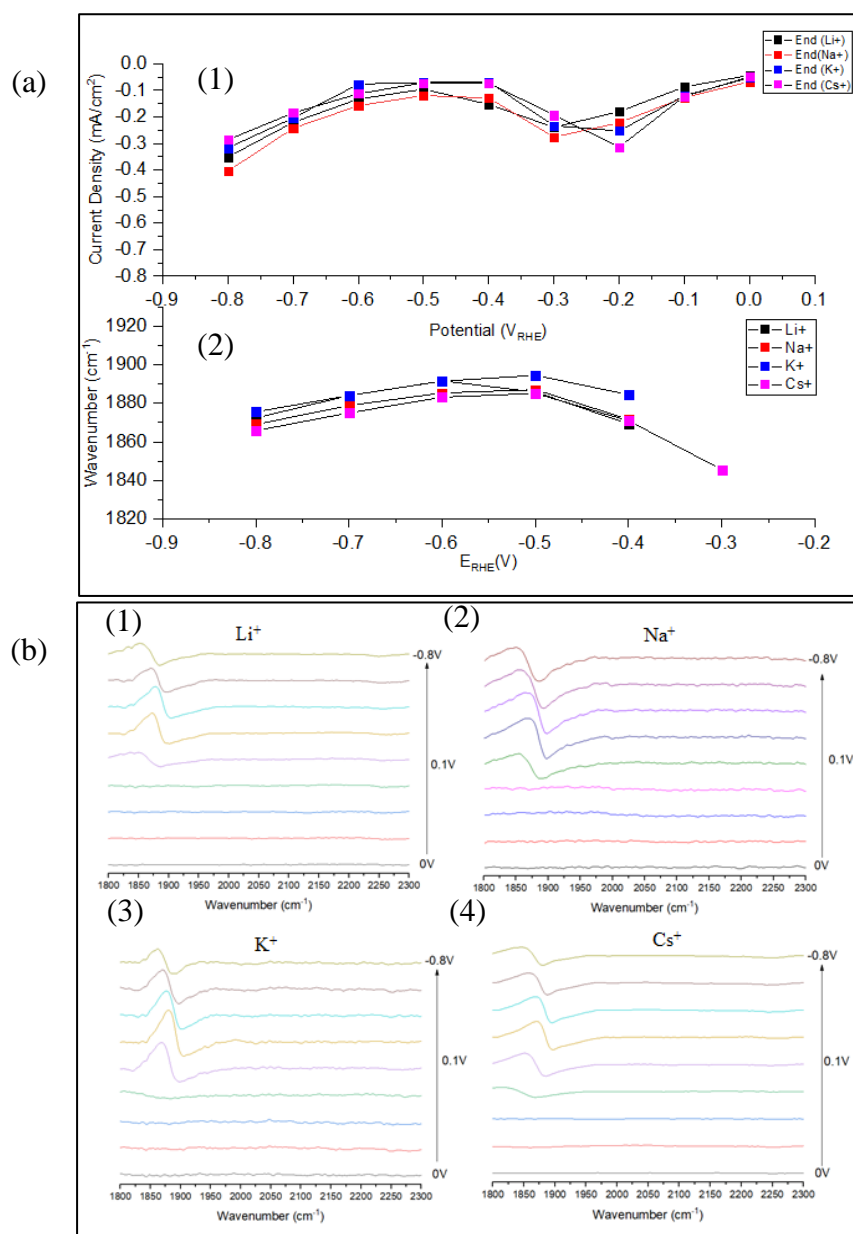
The impact potassium bicarbonate is discovered to have on the reduction of CO<sub>2</sub> has been vital in detailing minute discrepancies, central towards achieving an enhanced understanding of the palladium-CO<sub>2</sub> reduction system. Although insightful, the lack of information on the effects induced by the cation, over the palladium thin film or on the reduction reaction, warrants in depth analysis within the topic. Therefore to identify the cations impact on the CO<sub>2</sub> reduction reaction, 4 different elements from the alkali metal family are employed namely:

- a Lithium
- b Sodium
- c Potassium
- d Cesium

Beginning with the dynamic CA across the 4 alkali metal cations presented in figure 4.19, a distinct trend on the formation and accumulation of CO can be estimated from the variations in current densities. The Li<sup>+</sup> ion demonstrates delayed and Cs<sup>+</sup> ion the earliest initiation of CO at -0.4 V and -0.3 V respectively, with the Na<sup>+</sup> and Cs<sup>+</sup> ions displaying lowest and highest current density values at -0.8 V. Although the Li<sup>+</sup>, Na<sup>+</sup> and K<sup>+</sup> ions

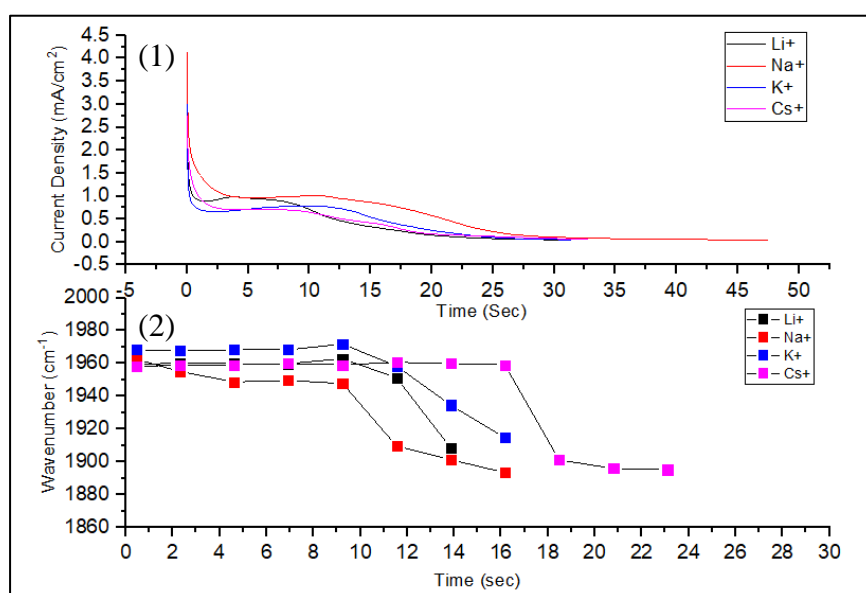


exhibit CO initiation at -0.3 V, the IR spectra signals its presence only at -0.4 V. The position of the peak centres plotted for the respective ions represent similar values, with the experimentally calculated rate of blue shift being 95.68, 60.509, 64.06 and 66.06 cm<sup>-1</sup>perV respectively. A similar trend across all the ions with regards to the peak area modification is observed, with it portraying an initial growth up to -0.5/-0.6 V followed by its decline until -0.8 V. Along with the dissimilarity in the initiation of CO across the various ions, the peak centres also show a slight difference in their values with potassium having the highest followed by lithium, sodium and cesium respectively.



**Figure 4.19- Dynamic CA study under CO<sub>2</sub> between 0 V and -0.8 V with a hold time of 10 sec at each potential conducted under 0.1M bicarbonate solution with Lithium, Sodium, Potassium and Cesium as the cation (1) Current density Vs. E<sub>RHE</sub> (V) and (2) Wavenumber (cm<sup>-1</sup>) Vs. E<sub>RHE</sub> (V) and (b) IR spectra plotted between 0 V and -0.8 V from 1800 cm<sup>-1</sup> and 2300 cm<sup>-1</sup> with a least count of 0.1 V under Lithium, Sodium, Potassium and Cesium.**

Continuing on the same surface, the CO formed under each of these ions was then oxidized by electrochemically applying a potential of 1.2 V, with the results published in figure 4.20. While complete oxidation under Li<sup>+</sup>, Na<sup>+</sup> and K<sup>+</sup> ions occur at 13.86 sec and 16.17 sec respectively, under Cs<sup>+</sup> ion the process prolongs to about 23.1 sec. Furthermore, the constant peak center regime extends until 16.17 sec under the Cs<sup>+</sup> ion in comparison to 9.27 sec observed under the other ionic solutions. While the peak center constant regime is uniform over the chosen cations, the bipolar conversion regime exhibits oxidation rates of 5.45 cm<sup>-1</sup>perV under Li<sup>+</sup>, 3.42 cm<sup>-1</sup>perV under Na<sup>+</sup>, 3.9 cm<sup>-1</sup>perV under K<sup>+</sup> and 3.93 cm<sup>-1</sup>perV under Cs<sup>+</sup> respectively. Comparing amongst the ions, the peak center positions of the various ions depict a recurrent trend with the K<sup>+</sup> ion presenting a higher frequency followed by the lithium, cesium and then sodium. In continuation with trends observed in the previous sub-section, irrespective of the ion the peak area is observed to increase with its reduction synchronous with the red shift in the peak center. Focusing on the CA plot, each of the curves display an increase in the current; concurrent with the change in area of the bipolar peak with the attainment of the peak maxima at a point when the peak center decreases. Analysis of the individual current density peaks depict its initiation to occur at 1.4 sec for Li<sup>+</sup>, 4.7 sec for Na<sup>+</sup>, 2 sec for K<sup>+</sup> and 3.5 sec for Cs<sup>+</sup>, with the Li<sup>+</sup> and K<sup>+</sup> ions presenting narrow, Na<sup>+</sup> ion presenting broad and Cs<sup>+</sup> ion presenting 2 convoluted peaks.



**Figure 4. 20 - Desorption profile for the dynamic CA study at 1.2V under CO<sub>2</sub> for Lithium, Sodium, Potassium and Cesium (1) Current density Vs. Time (sec) and (2) Wavenumber (cm<sup>-1</sup>) Vs. Time (sec)**

Following the dynamic CA study, the cationic effect on the reduction of CO<sub>2</sub> was analyzed by performing electrochemical studies at -0.3 V and -0.5 V for a period of 5 min as published in figures 4.21 and 4.22 respectively. While the Li<sup>+</sup>, K<sup>+</sup> and Cs<sup>+</sup> ions exhibit the formation and accumulation of CO under -0.3 V, the Na<sup>+</sup> ion only presents glimpses of its formation with its initiation occurring after 138.6 sec. While in the previous section

the time taken for attaining pseudo-stability under potassium was calculated to be 138.6 sec, the pseudo stability for the Li<sup>+</sup> and Cs<sup>+</sup> ions from the current data was calculated to be 238.08 and 190.46 sec respectively. Comparing the IR results with the CA data concurrently illustrates a synonymous relationship existing between the rate of current stability and the rate of pseudo stability of the bipolar peak center. The CA also establishes a trend with regards to the individual ions, with potassium once again attaining high frequencies with lithium and cesium following in suit.

Contradictory to the CO formation rate under the K<sup>+</sup> ion, oxidation seems to occur instantaneously. CO oxidation under the remaining cations are also quite interesting to analyze, with the Li<sup>+</sup> ion presenting a broader and shallower CA curve in comparison to the Cs<sup>+</sup> ion's slightly narrower but taller curve. The peak center shifts, especially for the K<sup>+</sup> and Cs<sup>+</sup> ions, depict an unusually decaying trend with the Li<sup>+</sup> ion following the commonly observed pattern of constancy in the peak center followed by a transition to the positive peak during the decreasing slope. CO oxidation, based on the IR spectra, is calculated to end within 10.66, 2.3 and 6 secs for the Li<sup>+</sup>, K<sup>+</sup> and Cs<sup>+</sup> ions respectively. Unlike the desorption study performed during the dynamic CA study, the ions present a reversal in the initial peak center values with potassium presenting the lowest with cesium the highest.

The CA study performed at -0.5 V depicts exponential growth of CO under Li<sup>+</sup>, Na<sup>+</sup> and Cs<sup>+</sup> ions, with the K<sup>+</sup> ion attaining stability instantaneously. Calculations on the formation rate, based on the IR data, clearly indicates the passive nature of the reaction under the Na<sup>+</sup> ion with the system demonstrating delayed initiation at about 7 sec and pseudo-stability after 47.6 sec. In comparison, the Li<sup>+</sup> and Cs<sup>+</sup> ions initiate the reaction instantaneously with pseudo-stability achievement within 28.57 and 23.8 sec respectively. The CA plot is also seen to project data synonymous to the results obtained during the IR Study. A similar pattern as observed across the various ion studies is initially witnessed, with potassium presenting a high vibrational frequency followed by lithium, cesium and sodium with the final frequency showcasing a pattern varying from lithium to cesium.

The oxidation data contradictory to the -0.3 V study, exhibits the presence of the 2 regimes namely the constant peak center regime and the transition regime, with the exception of the Cs<sup>+</sup> ion which seems to have both the regions amalgamated. Based on the results collected, K<sup>+</sup> ion deviates to a great degree during the oxidation reaction with complete oxidation arising within 4.63 sec, while the rest achieve this phenomenon within 13.9 sec for Li<sup>+</sup>, 8.35 sec for Na<sup>+</sup> and 19.9 sec for Cs<sup>+</sup> ions respectively. The deviation is similar to that observed during the -0.3 V desorption study with potassium having the lowest vibrational frequency while cesium has the highest. While the K<sup>+</sup> ion presents a narrow current curve, the others display a much broader one with the Li<sup>+</sup> ion shallower than Na<sup>+</sup> and Cs<sup>+</sup> ions.

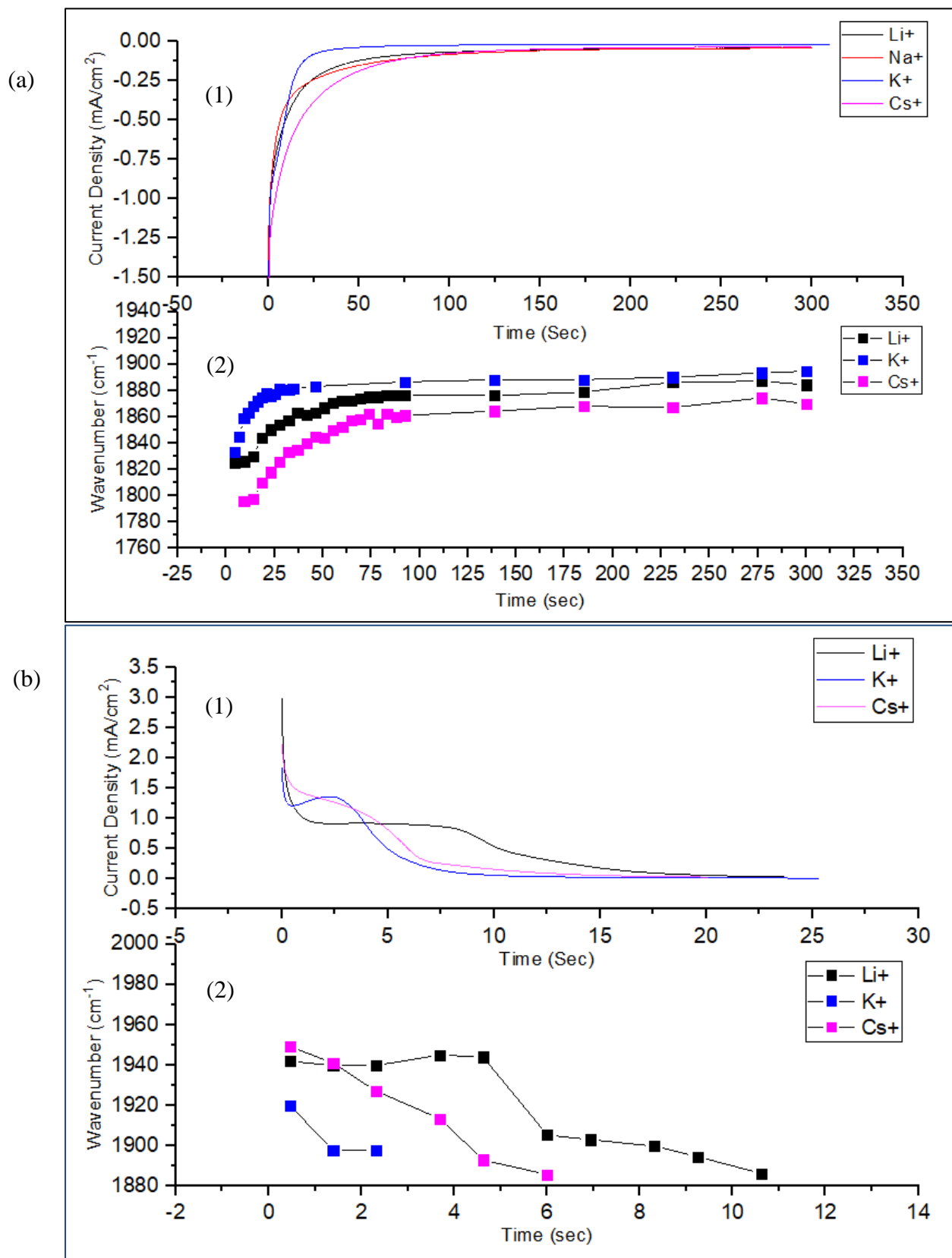


Figure 4. 21 - (a) -0.3 V CA study conducted for Lithium, Sodium, Potassium and Cesium under CO<sub>2</sub> for a period of 5 min (1) Current density vs. Time (sec) and (4) Wavenumber (cm<sup>-1</sup>) Vs. Time (sec) and (b) Desorption profile for the -0.3 V CA study at 1.2 V conducted for Lithium, Potassium and Cesium (1) Current density vs. Time (sec) and (2) Wavenumber (cm<sup>-1</sup>) Vs. Time (sec)

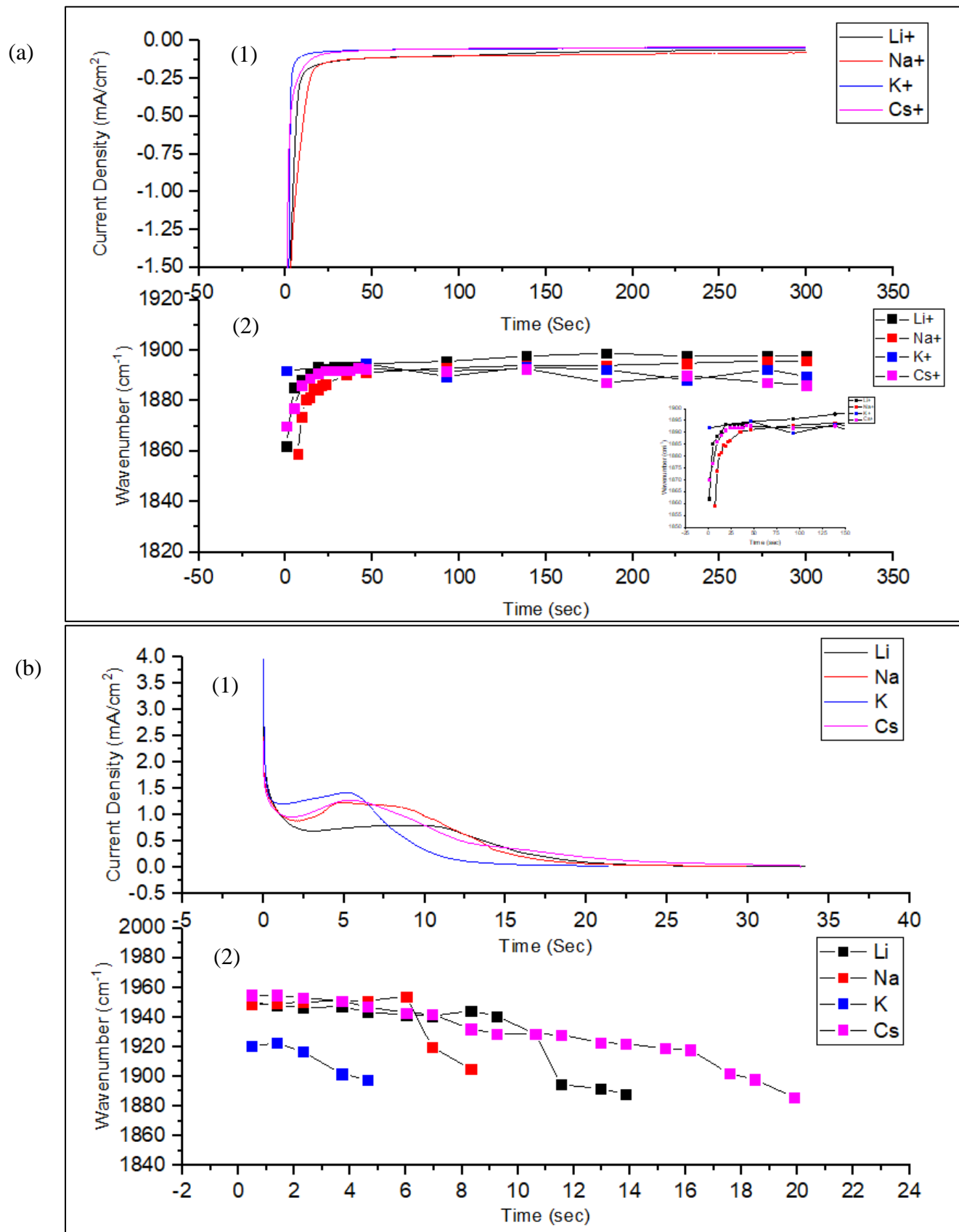


Figure 4. 22 - (a) -0.5 V CA study conducted for Lithium, Sodium, Potassium and Cesium under CO<sub>2</sub> for a period of 5 min (1) Current density vs. Time (sec) and (4) Wavenumber (cm<sup>-1</sup>) Vs. Time (sec) and (b) Desorption profile for the -0.5 V CA study at 1.2 V conducted for Lithium, Potassium and Cesium (1) Current density vs. Time (sec) and (2) Wavenumber (cm<sup>-1</sup>) Vs. Time (sec)

Following the analysis of the reduction reaction over the thin film through chronoamperometry, few interesting cyclic voltammetric studies were performed to delineate the route the reduction reaction adopts under the presence of different cations. Thus cyclic voltammetric studies at 10 mVpers and 2 mVpers are performed, expressing the modifications occurring at various stages of the potential study.

The 10 mVpers study is quite interesting with regards to the results published in figure 4.23(a). Each of the experiments under the different cations depict an ever increasing cathodic current maxima (before the exponential drop in the current), with the Li<sup>+</sup> ion marginally having the lowest current while the Cs<sup>+</sup> ion, through a significant margin, achieves the highest. The initiation of CO observed from the IR spectra in comparison to the CV, portrays concurrence with regards to each other. The slopes projected by the peak centers demonstrate minimal variation across the varying ionic radii (except for Cs<sup>+</sup> for 0 V to -0.8 V), with significant deviations observed only during the CO oxidation regimes of the study. The peak center values for the 4 ions diverge from the general trend observed till now, with lithium exhibiting the highest value followed by potassium, cesium and sodium. The values for the peak center trends under each regime and ion are tabulated in table 4.2. The peak areas, although vary slightly, present a similar trend across Li<sup>+</sup>, Na<sup>+</sup> and K<sup>+</sup> ions with an initial increase, decrease and stability until the oxidation regime after which the usual oxidation pattern is observed. The Cs<sup>+</sup> ion, on the contrary, deviates from the regular area trend with only the oxidation profile imitating the rest. Focusing on the cyclic voltammogram, specifically on the initial stages of the anodic regime, higher currents have been recorded for the palladium thin film under the Cs<sup>+</sup> ion deviating from the trends observed under the remaining three ions where prior to 0.5 V the currents were found to be negligible. The oxidation peaks observed across the 4 ions seem to vary greatly, with the Na<sup>+</sup> ion presenting early initiation with narrow curvature peaks, the Cs<sup>+</sup> ion displaying a broad convoluted peak and the Li<sup>+</sup> and K<sup>+</sup> ions initiating at similar potentials but with a lowered area for the latter in comparison to the former.

Further reducing the scan rate to 2 mVpers demonstrates a synonyms drop in the peak current density (-0.2 V to -0.3 V) amongst the various ions, as depicted in figure 4.23 (b), in comparison to the 10 mVpers study. But unlike the 10 mVpers study, the CO initiation presents a delayed representation on the IR spectra with the bipolar peak emerging only during the drop in the current density. The cathodic peaks recorded under each of the ions were concurrent with the bipolar peak initiation, with the peak center shifts similar across the 4 chosen alkali metals. While the peak shifts were similar, the peak values for the 4 ions on the other hand exhibited an altered arrangement with lithium presenting the highest vibrational frequency followed by sodium, cesium and potassium. The variations in the peak area, unlike the 10 mVpers study, are similar across all the 4 ions with the CO oxidation following similar trends. Shifting onto the CV, the oxidation peaks, except for that of sodium, originate at similar potential with the presence of 2 peaks; differing only with regards to the magnitude of variation in the peak area.

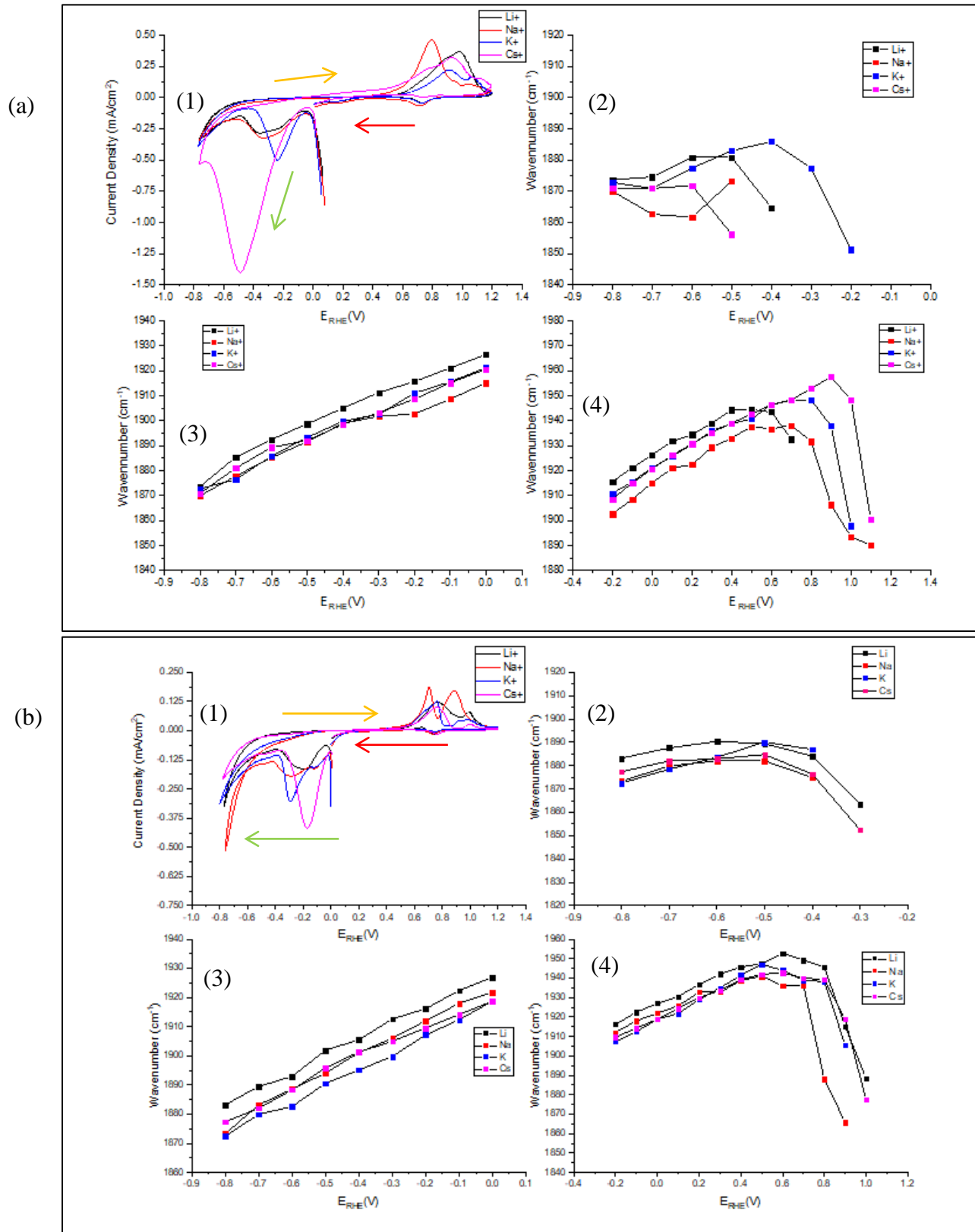


Figure 4.23 - (a) 10 mVpers CV study performed under CO<sub>2</sub> for Lithium, Sodium, Potassium and Cesium (1) Current density vs.  $E_{RHE}$  (V), and Wavenumber ( $cm^{-1}$ ) vs.  $E_{RHE}$  (V) between (2) -0.2/-0.3/-0.5 V and -0.8 V, (3) -0.8 V and 0 V and (4) -0.2 V and 0.8/1.0/1.1 V and (b) 2 mVpers CV study performed under CO<sub>2</sub> for Lithium, Sodium, Potassium and Cesium (1) Current density vs.  $E_{RHE}$  (V), and Wavenumber ( $cm^{-1}$ ) vs.  $E_{RHE}$  (V) between (2) -0.3/-0.4 V and -0.8 V, (3) -0.8 V and 0 V and (4) -0.2 V and 0.9/1.0 V



## In-Situ Infrared Spectroscopic Studies Of Palladium Thin films during CO<sub>2</sub> Electro-Reduction

The slopes across each of the regimes, under the two different scan rates and 4 different ionic radii are tabulated in table 4. Except for the values calculated between 0 V and -0.8 V during the forward scan and the CO oxidation regime, the slopes within a given section irrespective of the rate seem to be in close proximity of each other.

**Table 4. 1- Slope calculated for the peak center shift across the 4 regions identified in the wavenumber (cm<sup>-1</sup>) Vs. E<sub>RHE</sub> (V) plot for Lithium, Sodium, Potassium and Cesium**

Electrolyte		0.1M Sodium Bicarbonate (cm <sup>-1</sup> /V <sub>RHE</sub> )				0.1M Potassium Bicarbonate (cm <sup>-1</sup> /V <sub>RHE</sub> )			
		0V to -0.8V	-0.6V to 0V	0V to 0.7V	0.7V to 1.2V	0V to -0.8V	-0.6V to 0V	0V to 0.7V	0.7V to 1.2V
CO <sub>2</sub>	10mV/s	115.283	45.564	34.395	134.058	50.395	57.79	39.106	251.427
	2mV/s	28.499	56.634	38.46	198.310	57.806	58.524	58.66	99.473
Electrolyte		0.05M Lithium Carbonate (cm <sup>-1</sup> /V <sub>RHE</sub> )				0.05M Cesium Carbonate (cm <sup>-1</sup> /V <sub>RHE</sub> )			
		0V to -0.8V	-0.6V to 0V	0V to 0.7V	0.7V to 1.2V	0V to -0.8V	-0.6V to 0V	0V to 0.7V	0.7V to 1.2V
CO <sub>2</sub>	10mV/s	34.365	56.254	23.216	239.898	4.3917	53.603	37.606	285.46
	2mV/s	21.519	54.818	42.897	162.385	22.947	48.623	40.787	151.844

### 4.3 Identification of CO formed on the palladium surface

To identify the origin of CO during the N<sub>2</sub> saturation study, tracer carbon loaded 0.1M NaHC<sup>13</sup>O<sub>3</sub> solution was utilized during the 2 mVpers cyclic voltammetric study under the cathodic regime. Figure 4.24 represents the results obtained over the course of the CV and IR analysis performed under N<sub>2</sub> saturated 0.1M NaHC<sup>13</sup>O<sub>3</sub> and 0.1M NaHCO<sub>3</sub>.

While the initiation potential for CO formation at -0.6 V is quite similar to that obtained under normal NaHCO<sub>3</sub> solution, the bipolar peak centers demonstrate a significant disparity of about 70 cm<sup>-1</sup> initially and 50 cm<sup>-1</sup> latter on between the two solutions. The bipolar peak, as usually observed, depicts a similar peak center shift at a rate of 72.03 cm<sup>-1</sup>perV with the area under the peak growing and stabilizing at -0.7 V in the reverse cathodic scan. Although similar in terms of the IR trends, the current data exhibits departure from that obtained during the normal study with a reduced hysteresis and current observed in the former in comparison to the latter.

# In-Situ Infrared Spectroscopic Studies Of Palladium Thin films during CO<sub>2</sub> Electro-Reduction

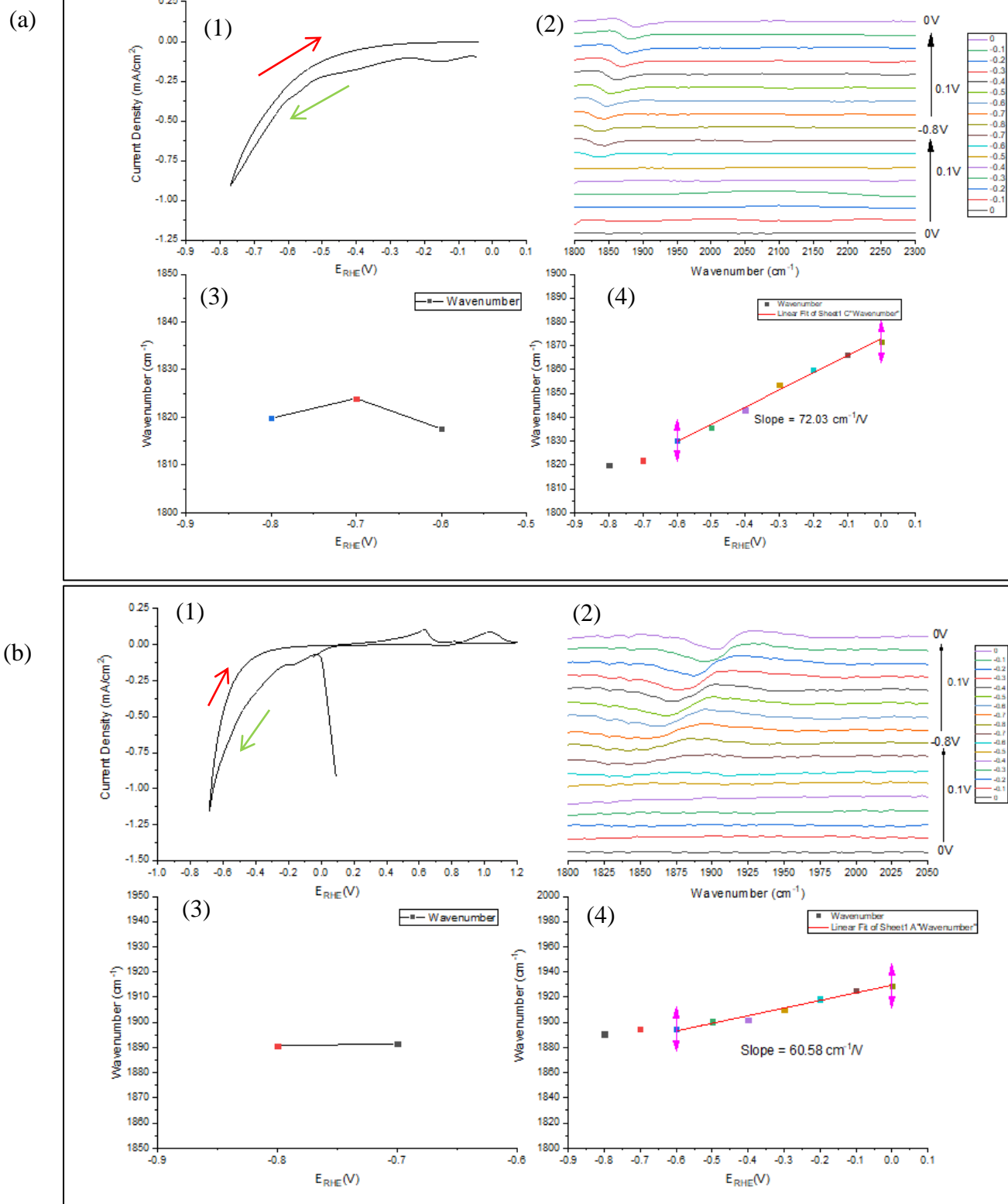


**Figure 4. 24 - (a) 2 mVpers CV study performed under CO<sub>2</sub> saturated 0.1 M NaHC<sup>13</sup>O<sub>3</sub> (1) Current density Vs. E<sub>RHE</sub> (V), (2) IR spectra plotted from 0 V to -0.8 V back to 0 V with a least count of 0.1 V and Wavenumber (cm<sup>-1</sup>) vs. E<sub>RHE</sub> (V) between (3) -0.3 V/-0.4 V and -0.8 V and (4) -0.8 V and 0V (b) ) 2 mVpers CV study performed under CO<sub>2</sub> saturated 0.1M NaHCO<sub>3</sub> (1) Current density Vs. E<sub>RHE</sub> (V), (2) IR spectra plotted from 0 V to -0.8 V back to 0 V with a least count of 0.1 V and Wavenumber (cm<sup>-1</sup>) Vs. E<sub>RHE</sub> (V) between (3) -0.3 V/-0.4 V and -0.8 V and (4) -0.8 V and 0 V**

To verify the extent of vibrational frequency variation between the normal CO molecule and the tracer C<sup>13</sup>O molecule, the following calculations are performed:

$$\text{Reduced mass} = \mu = \frac{m_1 \times m_2}{m_1 + m_2}$$

$$\text{Reduced mass tracer C}^{13}\text{O} = \frac{13 \times 16}{13 + 16} \times 1.66 \times 10^{-27} = \mathbf{1.1906 \times 10^{-26} \text{ Kg}}$$

$$\text{Reduced mass normal CO} = \frac{12 \times 16}{12 + 16} \times 1.66 \times 10^{-27} = \mathbf{1.1382 \times 10^{-26} \text{ Kg}}$$

$$\text{Spring Constant} = (\nu)^2 \times (2 \times \pi \times c)^2 \times \mu =$$

$$(1890)^2 \times (2 \times \pi \times 2.99 \times 10^{10})^2 \times 1.1382 \times 10^{-26} = \mathbf{1434.97 \text{ N/m}}$$

$$\text{Wavenumber for the tracer C}^{13}\text{O} = \frac{1}{2 \times \pi \times c} \times \sqrt{\frac{K}{\mu}} = \frac{1}{2 \times \pi \times 2.98 \times 10^{10}} \times \sqrt{\frac{1434.97}{1.1906 \times 10^{-26}}} = \mathbf{1847.94 \text{ cm}^{-1}}$$

The numerical value calculated for the C<sup>13</sup>O and the difference between the two isotopes with respect to the experimental data are approximately the same suggesting a possible influence of the bicarbonate during the CO<sub>2</sub> reduction study.



**Figure 4. 25 - IR spectra recorded during CO<sub>2</sub> bubbling of the N<sub>2</sub> saturated 0.1M NaHC<sup>13</sup>O<sub>3</sub> solution for a period of 5 min after the 2 mVpers CV study recorded between 1800 cm<sup>-1</sup> and 2300 cm<sup>-1</sup>**

To assess the possibility of substitution between the CO formed and CO<sub>2</sub>, the 0.1M NaHC<sup>13</sup>O<sub>3</sub> was saturated with CO<sub>2</sub> for a period of 5 min post the CV study. The results of the IR spectra recorded over the period are represented in figure 4.25. The bipolar peak existing between 1800 cm<sup>-1</sup> and 2000 cm<sup>-1</sup> displays negligible change in both the bipolar area as well as its peak center over the 5 min study.

## V Discussion

---

The results once collected and analyzed require formal detailed treatment in a bid to logically explain the reasons for the recorded and elaborated data. Therefore this chapter will focus on explaining the various irregularities identified in the previous chapter to improve and enhance our understanding on the CO<sub>2</sub> electrochemical reduction mechanisms on palladium.

### 5.1 Palladium thin film

The electrochemical and microscopic characterization of the palladium thin film is essential towards justifying the claims made during the course of the discussion. The visual appearance of the palladium thin film coupled with the proximity of the calculated surface area to that estimated for the (111) surface and the low average surface roughness clearly indicates its relatively high smoothness. The core reason behind the negligible surface roughness can be traced back to the surface features present on the silicon substrate and the sputter deposition parameters. As elucidated in chapter 2, the absence of irregular features on the surface of the substrate could prevent the emergence of facets other than the (111) through the reduction of their nucleation energies; given palladium has a FCC structure.

In addition to the surface, sputtering parameters such as low sputter pressure and low deposition rate coupled with substrate rotation enables uniform deposition and continuous film formation as is the case for the 15 nm palladium thin film. The absence of external heating of the substrate prevents surface mobility of the deposited atoms, thus resulting in multiple nucleation sites leading to the formation of a polycrystalline continuous film. Based on the sputter conditions implemented during the 9.45 min deposition study, exaggerated influence of the shadowing effect on the deposited film must be observed, but that doesn't seem to have happened with the depth profile, average skewness and kurtosis presenting values that indicate the presence of a continuous palladium film beneath. Due to the low thickness adopted for the study, the polycrystalline grains don't seem to completely coalesce giving rise to numerous island like structures that begin to coalesce; eventually forming the continuous film. Due to the low surface energy of the (111) facet, the formation of a continuous film with the film majorly consisting the (111) orientation is predicted to occur on the silicon substrate.

The adhesion of the sputtered palladium thin film on the silicon substrate is found to be weak and therefore peels off upon application of strong anodic potentials. The formation of palladium oxide which has a tetragonal structure (lattice parameters  $a = 3.051 \text{ \AA}$  and  $c =$

5.495 Å at potentials above 0.9 V) in a film consisting of F.C.C palladium, (lattice parameter of  $a = 3.88$  Å) could possibly induce stresses causing delamination.

The choice of thickness as presented by the AFM study is partially appropriate for conducting SEIRAS analysis due to the existence of island like morphology; critical towards the enhancement of IR vibrations of the adsorbed species. Therefore, surface activation through electrochemical cycling, especially at potentials higher than 0.9 V, enables the dissolution of palladium into the electrolyte reducing the contact between the island structures. During the study, activation cycling was performed at high scan rates to enable reduced dissolution. But converse to that expected, the possibility of palladium precipitating back onto the surface at positions disadvantages to the enhancement is quite high. This precipitation of palladium, leading to the partial coalescence of certain islands, could be one of the causes for the appearance of bipolar peaks (Abnormal Infrared element (AIE)) between  $1800\text{ cm}^{-1}$  and  $2000\text{ cm}^{-1}$ . This dissolution reaction is observed to reduce in intensity from acidic to basic solutions due to the increasing propensity of oxide stability as the pH increases, thus preventing activation under basic electrolytes [28]. In addition to the coalescence, the adsorption of molecules on the palladium surface has also been cited as a possible reason for AIE's, due to the modification of electronic properties affecting the refractive index of the palladium thin film. [66]

### 5.2 Electrochemical reduction of CO<sub>2</sub> under 0.1M potassium bicarbonate

The reduction of CO<sub>2</sub>, in the presence and absence of dissolved CO<sub>2</sub> within the electrolyte, has presented details that will be enumerated upon over the course of the subsection. The absence of IR peaks associated to bicarbonates and carbonates while the visibility of peaks representative of H<sub>2</sub>O, CO and SiO suggest weak bonding between the bicarbonates/carbonates and the palladium thin film.

Beginning with the CO<sub>2</sub> saturation study, the formation of CO is seen to initiate at potentials close to -0.2 V to -0.3 V depending on the mode and rate at which the study was performed. The 10 mVpers study demonstrated early initiation of CO, while both the dynamic CA and the 2 mVpers presented a slightly delayed response to the reduction study. pH measurements have determined the CO<sub>2</sub> saturated 0.1M KHCO<sub>3</sub> solution to stabilize at a value of 6.8, causing palladium to exhibit slightly delayed desorption of the adsorbed/absorbed hydrogen due to improved hydrogen binding strength of the thin film [28]. As a thin film is utilized during the study, the palladium is observed to absorb and adsorb hydrogen from the solution, transforming quickly into  $\beta$ -palladium hydride. But due to the low surface energy of the sputtered thin film, it is also assumed to have lowered surface binding energy to hydrogen leading to earlier initiation of H<sub>2</sub> evolution [44] [17]. The evolution of hydrogen will require constant flow of hydrogen to the

surface, causing the formation of  $\beta$ -palladium hydride with palladium clusters in the bulk of the palladium thin film. This in turn will give rise to a lowered surface coverage of hydrogen; enabling the facile formation of CO. [42] [44]

The lowered hydrogen coverage activates the reaction pathway through the lowered gibbs free energy of formation, thus promoting the formation of  $\text{COOH}^*$  and ultimately CO [16] [17]. The CO formed is strongly chemisorbed onto the palladium surface, as attested by the  $\text{N}_2$  bubbling test, presenting no discernable peak centre or peak area shift during the 5 min study. This result although in itself doesn't mean a lot, but when compared with the bond strengths on silver, gold and copper showcases its significance with regards to the objectives stated at the beginning of study. A.M Bradshaw et al. conducted infrared studies on silver, gold and copper depicting negligible to weak chemisorption ( $\text{Ag} < \text{Au} < \text{Cu}$ ) caused due to the limited  $\pi$  and enhanced  $\sigma$  bonding occurring between these metal surfaces and CO [67]. Figure 5.1 depicts the mechanism adopted for the reduction of CO on the palladium thin film.

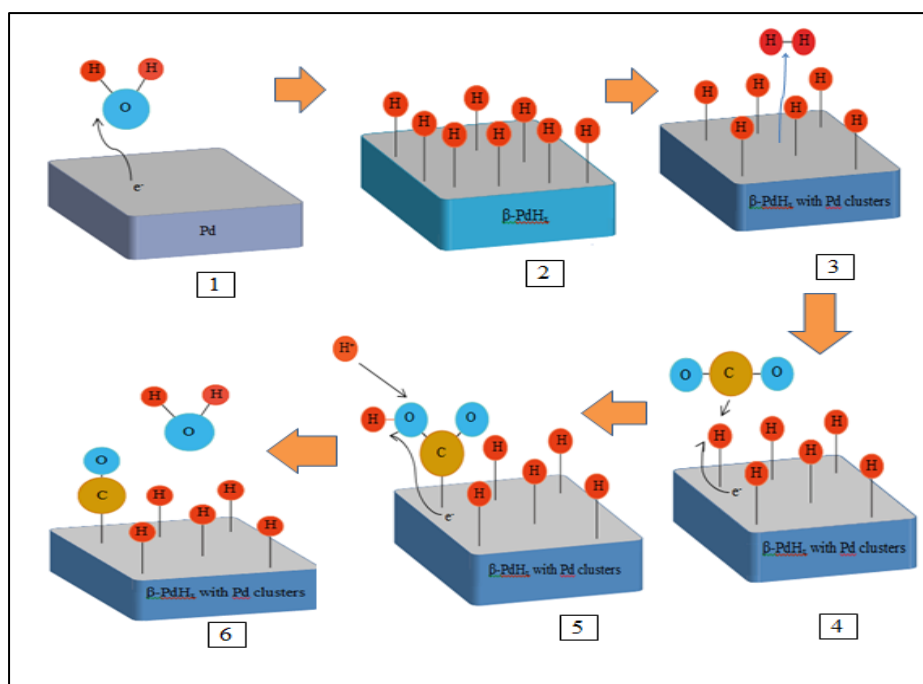


**Figure 5. 1 – Steps depicting the CO<sub>2</sub> reduction mechanism on the 15 nm palladium thin film (1) Reduction of H<sub>2</sub>O to adsorb hydrogen, (2) H completely adsorbed and absorbed to form  $\beta$ -PdH<sub>x</sub>, (3) Evolution of H giving rise to Low H surface coverage and  $\beta$ -PdH<sub>x</sub>@Pd, (4) The adsorption and reduction of CO<sub>2</sub> to form  $\text{COOH}^*$ , (5) Simultaneous proton and electron transfer towards the  $\text{COOH}^*$  and (6) Formation of CO with H<sub>2</sub>O as the by-product**

Focusing on the individual experiments beginning with the dynamic CO, the shift through the potentials starting with 0 V brings about bulk and surface related modification that are visible on the current density. As the potential shifts from 0 V to -0.2 V, the thin film first begins adsorbing/absorbing hydrogen followed by its evolution



beyond -0.2 V. As the potential reaches -0.3 V, the hydrogen coverage approaches the requisite percentage in order to facilitate the formation of CO, which strongly adheres onto the surface of the palladium thin film with the IR simultaneously depicting its presence at 1830 cm<sup>-1</sup>. The -0.4 V shows massive drop in the current density with the CO concentration exponentially increasing during this period. The subsequent potentials, starting from -0.5 V, represent an increase in the current density which can be related mostly to the evolution of hydrogen with only a small percentage of the current being utilized for the formation of CO. Such behaviour with regards to the CO accumulation rate was also observed by **Hahn Christopher et al.** [68] with the CO formation rate dropping beyond -0.6 V and the hydrogen evolution rate rising simultaneously. The amount of H<sub>2</sub> evolved during this region is substantially low due to the extreme poisoning of the palladium surface, observable from the current density before and after CO formation. Simultaneously, the bipolar peak on the IR spectra shows an increase in the area and the peak centre position synonymous with the formation and exponential accumulation of CO till -0.4 V. This was then followed by a red shift in the peak centre and a decrease in the peak area strongly suggesting the possible desorption of CO from the surface beyond -0.5 V. The desorption of CO from the palladium thin film surface can be explained with the help of the d- band theory. According to the d-band theory, there are two possible reasons that account for the desorption of CO:

- The presence of the (111) facet can give rise to a wider d band due to the high density of the plane, leading to greater overlap of the d orbital. This in turn could shift the d band centre slightly away from the fermi energy level causing reduced CO  $\Pi^*$  electron filling and therefore a weak bond from the onset.
- As the cathodic potential increases, the electron density of palladium also increases causing further shift in the d-band centre and ultimately rupturing the Pd-CO bond.

The desorption study conducted during the dynamic CA study shows the presence of a broad curve, a sign of the extent of CO accumulation on the palladium surface with the peak denoting a clear transition from CO oxidation to combined oxidation of CO and palladium. The cause for the delayed shift can be associated to the lack of active sites available for the adsorption of H<sub>2</sub>O through the Langmuir- Hinshelwood mechanism; identified by the lack of a discernable peak centre shift, but an observable bipolar area enlargement until the current maxima [69]. This enlargement in the peak area is symbolic of the weakening of the dipole-dipole coupling mechanism causing CO density reduction on the palladium surface. The maximum area achieved during the oxidation reaction is found to be synchronous with the red shift in the wavenumber, suggestive of the collapse of the dense colony structure that possibly forms over the course of the reduction

reaction. [70]. The oxidation of the CO molecule is suggested to occur through the following reaction -:

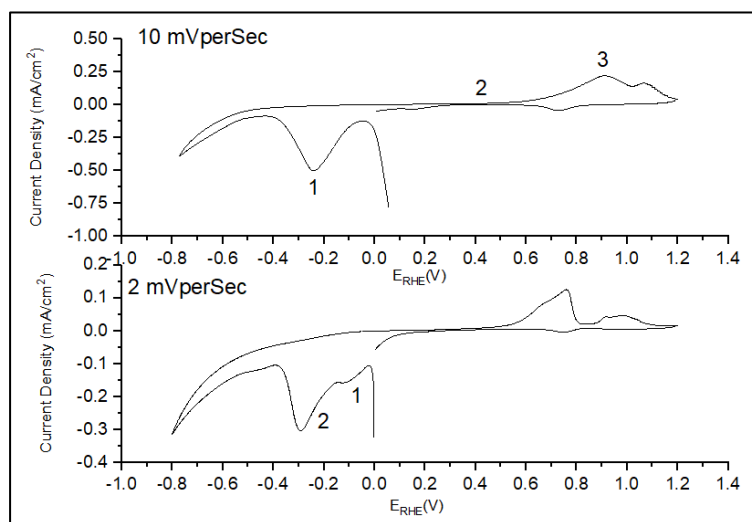
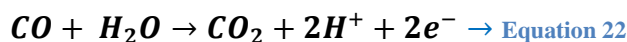


**Figure 5. 2- CV Study conducted at (a) 10 mVpers and (b) 2 mVpers under the CO<sub>2</sub> saturated 0.1M KHCO<sub>3</sub>**

The 10 mVpers, as with the dynamic CA, follows a similar trend during the forward cathodic scan. Peak 1 presents an immediate increase in the cathodic current which consists of both the adsorption/absorption as well as the evolution of hydrogen, with the subsequent drop indicating the formation and accumulation of CO. The increase in the current density following the minima demonstrates a similar trend of hydrogen evolution and CO desorption with lowered rate of CO formation. The reverse scan indicates a blue shift in the peak centre caused due to the increasing CO coverage on the surface of the palladium thin film causing repulsion between the increasing CO species. The increasing CO repulsion thus causes an increase in the strength of the CO bond which in turn increases the vibrational frequency of the system. In addition to the increasing CO-CO repulsion, the possibility of dipole-dipole coupling between the CO molecules can also occur causing increased vibrational frequency of the system [70]. Another interesting region on the CV is peak 2, indicating the absence of hydrogen desorption; a clear sign of the intense CO poisoning transpiring during the forward as well as the reverse cathodic scans of the CV. [39] [38]

The IR spectrum during the anodic scan depicts a stark tuning effect on the CO molecules created due the presence of anions. Stark effect is defined by the shift in the electronic properties of a molecular system due the presence of an external electric field. The accumulation of electrons on the palladium thin film and anions in the outer Helmholtz

layer generates an electric field that causes a shift in the electrical properties of CO and therefore leading to a shift in the vibrational frequency [71]. At about 0.5 V, peak 3 initiates the oxidation of CO along with the desorption of hydrogen. The desorption of hydrogen along with CO oxidation is caused by the unavailability of surface active sites for the recombination of hydrogen. As the oxidation continues, the peak area variation occurs simultaneously with the peak centre blue shift at 0.8 V which entails the disbandment or almost complete oxidation of CO. These theories to a certain extent can be corroborated by the sharp drop in the CO concentration with palladium oxide forming simultaneously beyond the transition point. The reason behind the sluggish oxidation profile, as explained during the desorption profile of the dynamic CA, results from the inability to adsorb water (hydroxyl ion) for CO<sub>2</sub> formation.

Unlike the 10 mVpers study, the 2 mVpers study represents 2 convoluted peaks during the forward cathodic scan. Peak (1) represents the adsorption/absorption of hydrogen; while peak (2) represent hydrogen evolution and formation of CO. The initiation of CO on the IR spectra shifts from -0.3 V to -0.4 V due to the reduced hydrogen evolution rate caused by the maintenance of a high surface and sub-surface hydrogen concentration at lower scan rates. The remainder of the study depicts similar trends as that of the 10 mVpers study and thus can be explained by similar mechanisms. The lowered rate of CO oxidation during the 2 mVpers CV study in comparison to the 10 mVpers CV study could be related to the increased CO coverage with a strong presence of CO dipole coupling inhibiting the oxidation of CO on the palladium surface.

The CO desorption rate during the three forward cathodic scans and the stark tuning rates between the two CV's during the anodic scans don't present any major deviations, suggestive of the negligible influence of the electrochemical parameters on the rate of shift in the vibrational frequencies. The minute increase in the stark tuning rate from 10 mVpers and 2 mVpers is most probably caused by the increased CO coverage achieved during the course of the 2 mVpers CV study. The lowered oxidation rate from 251.43 cm<sup>-1</sup>perV for the 10 mVpers to 99.473 cm<sup>-1</sup>perV for 2 mVpers signifies the increased driving force required for the initiation of CO oxidation caused by the increased CO coverage and CO dipole coupling on the palladium surface.

The chrono-amperometric studies performed at -0.3 V and -0.5 V provide additional details on the influence of the palladium thin film on the reduction reaction of CO<sub>2</sub>. While the -0.3 V study is found to take its time before achieving pseudo stability, the -0.5 V study achieves that instantaneously indicating the significance of the hydrogen reactions on the formation and accumulation of CO. Based on findings collected from numerous studies it is clear to assume that the surface instantaneously forms β- palladium hydride, with the rate of hydrogen evolution controlled by the potentials applied during the study. This in turn controls the extent of Pd clusters formed along with β- PdH<sub>x</sub> within the thin film; thus influencing the hydrogen surface coverage. [16] [44] [72] The

variation in the rate of hydrogen evolution with potential is observed to have a crucial impact in the rate of formation of CO, with the -0.3 V and -0.5 V depicting gradual and instantaneous CO formation associated to the sluggish and spontaneous rate of hydrogen evolution. Moving towards the desorption studies, the low CO coverage at -0.3 V oxidizes easily within 2.31 sec with a high possibility of loosely packed CO formation on the palladium surface. The reason for this hypothesis will be explained in section 5.3. In contrast to what was observed under the -0.3 V desorption study, the -0.5 V desorption clearly depicts the presence of a small but dense CO colony, collapsing within 1 -2 secs, with the remaining CO residue oxidizing instantaneously as was the case during the CV's. In accordance to the CO accumulation pattern over the palladium surface, the -0.3 V study presents early induction and narrow peak formation, while the -0.5 V portrays a slightly delayed initiation and broader peak formation for the current density profiles observed during their CO oxidation regimes. The peaks, based on the bipolar curves, represent the disintegration of the dense CO colonies coupled with the formation of palladium oxide on its surface. The transition from loosely packed CO molecules at -0.3 V to dense CO colonies at -0.5 V illustrates the transition occurring over the palladium surface during the formation and accumulation of CO, with CO density increasing as the potential increases. The CO molecules formed during the initial stages possibly act as anchors for the remaining to develop close to each other, thus creating a densely packed CO structure.

To understand the uniqueness of the results recorded during the study, a comparative analysis is conducted with results obtained from studies performed on palladium nanoparticles and 100 nm palladium thin films by **Gao Dunfeng, et al.** and **Hahn Christopher et al.** The delayed desorption of CO at about -0.6 V on the 100 nm film illustrates the importance of the palladium hydride system for the reduction of CO. Although differing in the desorption potential, the characteristics associated with the formation and stability of CO remains the same, with a majority of the current utilization gradually shifting from CO to H<sub>2</sub> evolution as the CO concentration attains pseudo-stability (point of lowest current during the forward cathodic scan on the CV's). [68] While this was the case for the thin films, palladium nanoparticles provided the perfect platform to produce a product that doesn't poison the palladium surface, "**FORMIC ACID**". The formation of formate with the concurrent reduction to CO at potentials similar to those applied during our study, provides strong evidence on the effect the surface energies have on the reduction of CO<sub>2</sub>. The high surface energies associated with the different low and high packing density facets and lower number of neighbouring atoms for the individual facets, aids the formation of formate on the nanostructures. [16] [42]

The N<sub>2</sub> saturation study as expected, displayed results deviating to a certain degree from that received during the CO<sub>2</sub> study. The short term and low potential analysis performed on the palladium surface, such as the dynamic CA and the -0.3 V 5min study, do not

present any indication of CO formation. While the dynamic CA depicts a constant increase in the current density over the potential profile, the -0.3 V CA attains stability quite quickly. The major reason behind the lack of CO initiation can be pinpointed to the elevated hydrogen binding strength caused by the 8.5 pH of the electrolyte [28]. The palladium thin film, based on the pH, will contain a high coverage of hydrogen with the evolution of hydrogen observed at high cathodic potentials. In contrast, the -0.5 V study presents a feeble bipolar peak with a peak centre at  $1860\text{ cm}^{-1}$  and a current unable to achieve stability within the 5 min period. This trait undoubtedly depicts the passivation the pH instils onto the palladium film through the large binding energy value for hydrogen.

In contrast, the cyclic voltammetric studies performed at 10 and 2 mVpers under N<sub>2</sub> portrays the films tendency to form CO at higher potentials. The delayed CO initiation during the 10 mVpers study, with the presence of the hydrogen desorption peak convoluted with the CO oxidation peak, is a clear indication of the low CO concentration and therefore proof of the inhibiting properties of high H coverage and low CO<sub>2</sub> concentration on the initiation and accumulation of CO. The 2 mVpers study on the other hand presented earlier initiation at -0.4 V, with the H desorption peak absent. The early initiation and high CO concentration coupled with sluggish growth kinetics (based on the cathodic currents observed) at 2 mVpers signifies the presence of optimal H coverage, lower H evolution rates and low CO<sub>2</sub> concentration over the palladium surface. The current densities observed during the hydrogen evolution regime coupled with the trend observed in the IR spectra proposes the possibility of CO initiation transpiring at high hydrogen coverage's with further accumulation requiring reduced hydrogen concentration on the catalyst surface [73]. In addition to the coverage, the mass transfer limitations introduced by the low CO<sub>2</sub> concentration also play a crucial role in inhibiting the reduction of CO<sub>2</sub>; observable during the scan rate reduction from 10 mVpers to 2 mVpers. The stark tuning rates calculated during the 10 mVpers and 2 mVpers studies at the anodic potentials report similar values as of those under the CO<sub>2</sub> study, suggesting an influence of the pH in addition to the CO coverage on the fluctuations observed on the CO vibrational frequencies. This influence of pH on the CO molecule can be hypothesized by the variation in the Fermi levels as proposed by **Uddin Jamal et al.** for similar shifts observed on platinum electrodes upon CO adsorption. [74]

The lack of CO<sub>2</sub> in the N<sub>2</sub> saturated solution still brings about the formation of CO which is a fascinating observation obtained during the reduction reaction. A number of reasons for the occurrence of this phenomenon exist, with the two prominent reasons being:

- Bicarbonate reduction by the thin film.
- Bicarbonate transformation to CO<sub>2</sub>, with the CO<sub>2</sub> then reduced by the palladium thin film

To confirm the CO growth pattern on the palladium thin film, oxidation studies were performed from 0.8 V to 1.2 V. The results from the study strongly endorse the claims made on the formation of densely packed CO colonies at high CO concentrations. The growth in the bipolar peak area without any detectable peak center shift, observed especially at 0.8 V and 0.9 V, illustrates the existence of a dipole-dipole coupling mechanism between the CO molecules chemisorbed on the palladium surface. The increase in the area of the palladium thin film as the peak center remains constant depicts a density reduction of the CO colony with the dipole- dipole coupling decreasing and the oxidation driving force increasing as the potential increases. At potentials greater than 0.9 V, the CO colony disintegrates at a point when the peak center shifts suggesting simultaneous oxidation occurring on both CO and palladium beyond this stage.

In addition to the intriguing nature of the desorption studies, the -0.8 V 5 min reduction study demonstrates instantaneous CO formation without any indication of desorption in the IR spectra. The modifications in the peak area and peak center under the study are similar to that observed under the -0.5 V study further endorse the existence of CO dipole coupling at high CO coverage's on the palladium surface.

### 5.3 Cationic effect on the palladium thin film affecting the CO<sub>2</sub> reduction reaction

As elaborated in chapter 2, the cations within the electrolyte play a key role in regulating CO<sub>2</sub> reduction on the surface of the palladium thin film. All the experiments performed on the alkali metal ions were based on the experiments conducted during the analysis of the palladium thin film under CO<sub>2</sub> saturated 0.1M KHCO<sub>3</sub> solution.

As usual, beginning with the dynamic CA study, each of the ions seem to have a particular effect on the electrochemical behaviour of the palladium thin film. While K<sup>+</sup> and Cs<sup>+</sup> ions follow a particular trend, the Na<sup>+</sup> ion acts out of character by depicting reduced CO poisoning; possibly an effect of the sluggish H<sub>2</sub> evolution and CO<sub>2</sub> reduction reaction rate. [75] The initial stages of the reduction reaction maintain a trend across the 4 ions, with the Li<sup>+</sup> ion showing the least current density with regards to H evolution while the Cs<sup>+</sup> ion shows the most. This in turn advances the formation of CO as the ionic radii increases from lithium to cesium. These effects have been experimentally explained by **Yoshitake et al.** [75] who suggested an increase in the presence of sub-surface hydrogen with increasing radii; providing constant hydrogen to the surface and maintaining appropriate hydrogen surface coverage for the reduction of CO<sub>2</sub>. Another plausible theory supporting the early initiation of CO is the influence the cation at the outer Helmholtz layer has on reducing the activation energy for the CO<sub>2</sub> reduction reaction. [76] Frumkin based on his studies theorized that as the cationic radii increases, the specific adsorption of these ions at the outer Helmholtz layer increases and thus its potential also increases.



[77] This increasing potential raises the zeta potential of the double layer helping towards reducing the activation barrier for not only enhancing the formation of CO but also for the adsorption/absorption/evolution of hydrogen. Moving on to the IR spectra, the CO desorption rate, as observed in figure 4.19, doesn't seem to vary a great deal with regards to the ions chosen. On the other hand, a comparison across the individual ions did depict a shift in the peak centres, ranging from potassium to cesium, possibly due to the relatively high CO coverage under the K<sup>+</sup> ion causing weakened Pd-CO bonding and high vibrational frequencies.

This outcome yields crucial insights suggesting that while the environmental conditions don't influence the CO desorption rate, the ions seem to induce major modifications, not only on the palladium thin film but also on CO, impacting the entire electrochemical mechanism occurring on the thin film [76]. The influence of the electric field between the ion and the palladium can induce a stabilizing effect on the chemisorbed CO molecule, thus bringing about shifts in their peak centres depending upon the ion utilized.

The oxidation study, based on previous experiments, exhibits laboured oxidation and broad peak formation for all except the Li<sup>+</sup> ion, a sign of the extent of CO accumulation on the palladium surface. The peaks observed on figure 4.20 across the various ions depict a clear transition from CO oxidation to combined oxidation of CO and palladium. The IR spectra are indicative of the presence of dense CO regions as was noted in section 5.2 as well. The peak centres continue on from the dynamic reduction study, with the Cs<sup>+</sup> ion depicting possible structuring of the CO molecules on the palladium surface inhibiting the reduction reaction from initiating; proved by the constant peak area over the first 8 sec of the oxidation study [69]. Another interesting assessment during the study is the completion of CO oxidation simultaneously under Na<sup>+</sup> and K<sup>+</sup> ions suggesting the presence of a loosely packed CO structure under the K<sup>+</sup> ion enabling ease of water adsorption within the CO dense structure.

Moving onto the -0.3 V and -0.5 V study, the deviation of the Na<sup>+</sup> (at -0.3 V and -0.5 V study) and K<sup>+</sup> ion (-0.5 V study) data from the remainder of the study requires further elucidation to better understand their influence on the palladium thin film. The lack of CO formation under the Na<sup>+</sup> ion could be due to the slow hydrogen evolution rate at -0.3 V and -0.5 V through the modification of the palladium behaviour, delaying the reduction reaction on its surface. The converse is noticed for the K<sup>+</sup> ion which shows instantaneous formation of CO at -0.5 V, probably due to the high subsurface H concentration facilitating the maintenance of suitable surface conditions for the formation of CO. [75] The remaining ions in the respective studies depict similar characteristics as observed on the dynamic CA study, with potassium justifying its implementation as the preferred cation for the reduction of CO<sub>2</sub>. The unique trend observed towards the end of the -0.5 V CA study indicates the increasing ionic effect with ionic radii enabling the stabilization of CO on the palladium surface. The absence of this ionic effect during the -0.3 V study



could be associated to the low CO coverage achieved in comparison to that achieved under the -0.5 V CA study.

The oxidation data under -0.3 V at least for the K<sup>+</sup> and Cs<sup>+</sup> ions seem to deviate from the regular patterns generated during the reduction study. While the Li<sup>+</sup> ion bipolar peak characteristics imply the formation of dense CO regions, the formation of CO under K<sup>+</sup> and Cs<sup>+</sup> ions suggest a more scattered profile for the CO molecules. While that may be true for the Cs<sup>+</sup> ion, a more plausible suggestion for the K<sup>+</sup> ion would be the formation of a loosely packed CO colony enabling straightforward oxidation of the CO produced; as assumed during the discussion in section 5.2 . Under the Cs<sup>+</sup> ion, the high concentration of hydrogen in the subsurface region allows the formation of CO but prevents its accumulation; giving rise to scattered CO molecules. While the Li<sup>+</sup> ion has a lower hydrogen evolution rate than the K<sup>+</sup> and Cs<sup>+</sup> ions, the lack of subsurface hydrogen atoms possibly through lowered hydrogen mobility through the palladium thin film prevents surface replenishment and therefore enables maintenance of appropriate surface hydrogen concentrations for the accumulation of CO in a close packed structure. [75] This close packed structure will give rise to delayed CO oxidation as inferred from the peak areas calculated from the IR spectra (Images presented in appendix 10). The current densities again are concurrent with the CO concentrations and arrangements found on the palladium surface as described by the IR spectra.

At -0.5 V, the desorption process returns back to normalcy with all the ions showing dense CO colonies forming on the surface. Again similar to the -0.3 V study, the current densities are concurrent with CO concentrations and arrangements on the palladium surface, but with a longer stability period due to the higher reduction potential. The peak centres, as is the case in the -0.3 V study, vary from the Cs<sup>+</sup> ion to the K<sup>+</sup> ion with cesium depicting maximum coverage. The increased CO concentration under cesium can be linked to the lack of sub-surface H atoms feeding the surface active sites caused due to the increased evolution intensity at -0.5 V, thus aiding the accumulation of CO through the reduction in the gibbs free energy of formation for the COOH\* intermediate. [16] The remaining ions demonstrate similar trends as observed in the -0.3 V study, thus confirming the validity of the assumptions made over the course of the discussion.

Finally a comparative study is performed for the four cations under the 10 mVpers and the 2 mVpers scan rates. The voltammograms from the 4 ions vary with regards to each other only with respect to initiation of the hydrogen evolution from the palladium surface; with the Li<sup>+</sup> ion depicting delayed and reduced evolution while the Cs<sup>+</sup> ion the highest. This behaviour coincides concurrently with data collected on the initiation of CO, with Na<sup>+</sup> and Cs<sup>+</sup> ions showing initiation only at lowered potentials due to their inability to maintain the requisite hydrogen concentration on the surface for CO formation. Although it is quite evident for the Cs<sup>+</sup> ion, this may not be case for the Na<sup>+</sup> ion which depicts a delayed drop in the current even though the area under the curve

between 0 V and -0.4 V is higher than the Li<sup>+</sup> ion. In the anodic section of the voltammogram, all except for the Cs<sup>+</sup> ion depicts peak initiation at about 0.5 V to 0.6 V, with the Cs<sup>+</sup> ion having its initiation from 0 V. This again can be related back to the extensive hydrogen evolution observed under the Cs<sup>+</sup> ion which prevents intensive poisoning of the surface allowing for hydrogen desorption at the appropriate potentials. This observation under the Cs<sup>+</sup> ion is significant as it hints at the existence of a precise hydrogen surface coverage vital for the accumulation of CO. Combining the voltammograms with the bipolar peak centre data during the oxidation region presents a concurrent trend explaining precisely the happenings on the surface. Each of the oxidation peaks illustrate the disintegration of the densely packed CO colonies, followed by the oxidation of palladium simultaneously occurring alongside CO. The increase in the peak centre values for Li<sup>+</sup> and a decrease for Na<sup>+</sup> and K<sup>+</sup> ions over the course of the study suggests the introduction of the stabilizing ionic effect for the K<sup>+</sup> ion on the CO molecules as the CO coverage increases and low CO coverage for the Na<sup>+</sup> ion over the palladium surface increases. This stabilizing effect is not witnessed under the Cs<sup>+</sup> ion possibly due to the minimal CO surface coverage as visible from the hydrogen desorption.

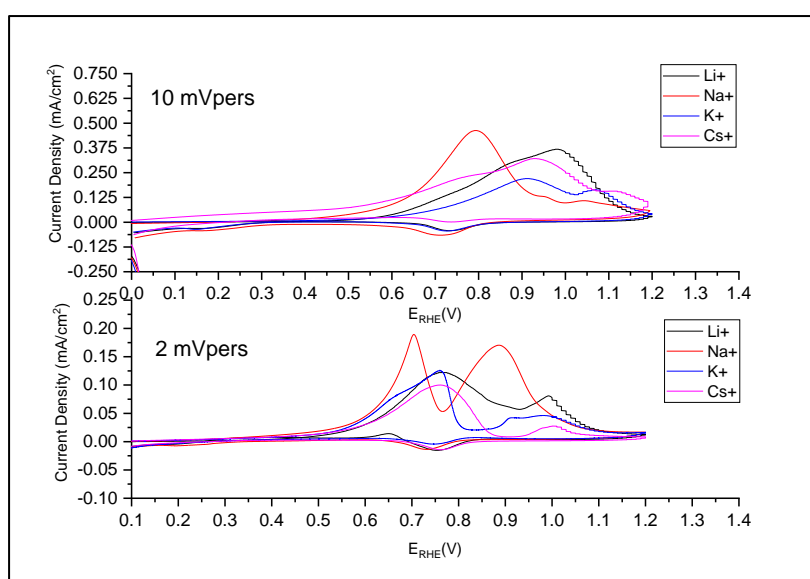


Figure 5. 3- CO oxidation regime for the 4 alkali ion electrolytes under the 10 mVpers and 2 mVpers CV study

As the scan rate reduces to 2 mVpers, the extent of hydrogen adsorbed/absorbed increases with the trends identical to that observed under the 10 mVpers study. The hydrogen desorption peak under the Cs<sup>+</sup> ion is absent in this case, which would suggest an increase in the concentration of CO caused due to the extended period spent at these reduction potentials. The lower scan rates allow the surface to achieve maximum surface CO coverage. Similar to the 10 mVpers, the concurrency between the voltammograms and the bipolar peak centre data during the oxidation region explains precisely the happenings on the surface. In contradiction to the studies performed so far, the peak

centres seem to be high for lithium followed by sodium, cesium and potassium. The reduced value for potassium could be linked to the ion's effect on the CO molecule. For both the studies, a similar trend with regards to the stark tuning rate is observed, irrespective of the technique utilized.

Observing the oxidation regime of the 10 mVpers and 2 mVpers CV study, as depicted in figure 5.3, provides a clear indication of the process overlap occurring at higher scan rates. The process that generally entail during this potential regime, as has been described earlier, are the desorption of hydrogen, oxidation of CO and oxidation of palladium. The existence of such convoluted peaks, especially during the initiation of CO oxidation, could be caused by the adsorption of CO on the various facets on the palladium surface leading to varied oxidation initiation potentials on the palladium surface. The CV's and IR spectra's for the Na<sup>+</sup> ion depict early initiation and low vibrational frequencies further reinforcing the theory of ionic inhibition towards CO formation on the palladium surface.

### 5.4 Identification of CO formed on the palladium surface

In order to clarify the source of CO in a solution devoid of external CO<sub>2</sub>, 0.1M NaHC<sup>13</sup>O<sub>3</sub> electrolyte was implemented during the 2 mVpers study. Although the voltammogram doesn't show a huge hysteresis in comparison to the 0.1M NaHCO<sub>3</sub> study, the CO bipolar peak initiation potential closely matches that of the latters. Based on the vibrational calculations of the two different carbons on the CO and the bipolar peak centre positions, it is indisputable that the bicarbonate acts as a source for the CO formed. The following are the possibilities for the formation of CO from bicarbonate:

- Direct reduction of bicarbonate to CO
- The conversion of bicarbonate to CO<sub>2</sub>, which then gets converted to CO through the pathway discussed above

The lack of evidence supporting the direct reduction of bicarbonate coupled with the existence of theories that firmly explains the reversible nature of the bicarbonate - CO<sub>2</sub> system, suggests the consequential reaction that enables the formation of CO is of that between bicarbonate and CO<sub>2</sub>.

The bubbling of CO<sub>2</sub> reiterates the strong bond that exists between CO and the palladium thin film which doesn't indicate any substitution occurring as can be ascertained from the constant bipolar peak centers on figure 4.25.

## VI Conclusion and Future Recommendations

---

The electrochemical reduction of CO<sub>2</sub> on the 15 nm palladium thin film revealed unique, fascinating and insightful information on the various mechanisms involved during the formation and accumulation of CO. Based on the comprehensive analysis of the accumulated data in chapter 5, a summary of the discoveries along with possible future avenues are enumerated upon in this chapter.

### 6.1 Conclusion

The implementation of SEIRAS to analyse the electrochemical reduction mechanisms transpiring over the palladium surface has successfully been able to contribute towards solving the objectives laid out prior to the inception of the report. Over the course of the sub- chapter, the answers to each of the objective questions will be briefly summarized; offering the reader an overview of the concepts that emerged over the course of the study.

#### **1 Palladium thin film Characterization**

The as-sputtered 15 nm palladium thin film produces an almost continuous layer with numerous island like structures, exhibiting an average diameter of 21.5 nm, coalescing upon each other. The polycrystalline thin film although closely emulating the surface required for SEIRAS, demonstrates poor adhesion courtesy of the weak bond strength between the sputtered palladium and the silicon substrate. The initiation of island coalescence prevents the appearance of the surface enhancement on the IR spectra, thus requiring surface activation through cyclic voltammetry. Given the smoothness of the as-sputtered palladium thin film, the (111) facet would be achieved on the Si-ATR substrate.

#### **2 Qualitative analysis of the CO<sub>2</sub> reduction reaction on palladium thin films under CO<sub>2</sub> and N<sub>2</sub> saturated KHCO<sub>3</sub> solution studied using infrared spectroscopy**

The importance of hydrogen in order to initiate the reduction reaction over the palladium thin film was witnessed during the study under potassium bicarbonate. The formation of CO was found to initiate at -0.3 V with the reduced production and desorption occurring beyond -0.6 V caused by the shift in the palladium d band centre and the increasing CO repulsion force on the thin film surface. The requirement of  $\beta$ -PdH<sub>x</sub>@Pd with the presence of a high H coverage for the initiation of CO but a lowered H coverage for continued accumulation was observed over the course of the study with its quick

formation enabled by the slimness of the palladium film. The CO<sub>2</sub> reduction studies performed under CO<sub>2</sub> and N<sub>2</sub> saturated solutions demonstrate the importance of pH and concentration, with the increased hydrogen binding and CO<sub>2</sub> mass transfer limitation causing delayed initiation and inhibited accumulation of CO on the surface of the palladium thin film. The dense CO structures formed prevent instantaneous oxidation of CO due to CO dipole coupling, with the potential being a key driving force for the oxidation reaction. The very same structure also prevents the desorption of hydrogen adsorbed by the palladium thin film due to the requirement of surface active sites occupied by the CO molecules. The desorption and the stark tuning rates were found to remain constant irrespective of the methods utilized during the study strongly indicating towards the impact the catalyst has on the bond strength with CO. Along with CO<sub>2</sub> being a direct source for the reaction to occur, the bicarbonate ion was identified to be an indirect source providing CO<sub>2</sub> to the solution through the reversible reaction. This identification was performed using a carbon tracer in NaHCO<sub>3</sub> solution under N<sub>2</sub>, giving rise to bipolar peak 70 cm<sup>-1</sup> - 50 cm<sup>-1</sup> below the actual vibrational frequency.

### **3 Qualitative analysis of the cationic effect on palladium thin films during the CO<sub>2</sub> reduction reaction studied using infrared spectroscopy**

Influence of the alkali metal ion over the behavioural modifications ensuing over the activated palladium thin film were clearly demonstrated by the various electrochemical techniques employed during the course of the study. The increase in the ionic radii, as described by frumkins model, brought about an increase in not only the hydrogen evolution rates, but also in the mobility of hydrogen ions within and CO<sub>2</sub> reduction on the palladium thin film. The stabilizing effect of the ions on the CO molecules, which increased with the increasing radii, was observed to take effect only at high CO coverage's, with its absence demonstrating high vibrational frequencies especially for the studies performed under the K<sup>+</sup> ion. While the initiation of the CO<sub>2</sub> reduction reaction varied from Li<sup>+</sup><Na<sup>+</sup><K<sup>+</sup><Cs<sup>+</sup>, the rate of CO accumulation depended on the condition's prevailing during the reduction study. The formation of CO has been observed to produce dense structures with K<sup>+</sup> forming loosely packed CO structures throughout the process, enabling ease of CO oxidation on the palladium thin film. The tightly packed dense structures ,observed for the Li<sup>+</sup> ion under the -0.3 V study and the Cs<sup>+</sup> ion for the dynamic CA study, demonstrate delayed initiation of the oxidation reaction caused by the lack of active sites for the adsorption of water molecules. The similarity in the desorption and the stark tuning rates across the 4 ions cannot be considered as an indication of the ineffectiveness of the environmental parameters on the vibrational frequencies of the CO molecules. This absence is related to the variation in the CO coverage's across the various ions leading to unsuitable scenarios for comparison.

#### **4 Analysis of the CO poisoning effect on the palladium thin films along with the determination of possible solutions towards reducing its formation**

Based on the results discussed with regards to the CO<sub>2</sub> reduction reaction occurring on the palladium thin film, the following important insights were gained enabling improved understanding of the reduction mechanisms on the palladium surface:

- a) CO poisoning on the surface of the palladium thin film is initiated by the formation of palladium hydride with the presence of a relatively high surface coverage of hydrogen for initiation with lowered surface H coverage for accumulation.
- b) The smoothness of the surface doesn't impede the formation and accumulation of CO, demonstrating strong affinity for the thin film to reduce CO<sub>2</sub> to CO.
- c) The CO formed adheres strongly onto the palladium active sites preventing any further reaction from occurring on the surface, including the desorption of hydrogen from the bulk of the thin film.
- d) The alkali metal ions influence the behaviour of the palladium thin films in increasing order of their ionic radii, with the K<sup>+</sup> ion introducing modifications that are perfect for the reduction of CO<sub>2</sub> and oxidation of CO on the thin film surface.
- e) The CO molecules formed on the palladium thin film behaves as anchors for the formation of dense structures on the surface of the thin film.

Although further analysis of the system is required for suggestion of recommendations for the reduction of CO formation:

- Implementation of porous and therefore high surface area thin films to obtain high surface energy facets. This could perhaps inhibit the formation of CO at low cathodic potentials through the formation of formic acid on the palladium catalyst.
- Modification of the electronic structure to reduce the binding strength through either alloying or doping with secondary metals such as gold, platinum, boron, etc.

## **6.2 Future Recommendations**

The limitless expanse of the imagination enables mankind to explore innumerable possibilities aiding advancements in society. Extending this concept into the current study, there exist possibilities to further analyse the reduction mechanisms over the palladium catalyst which are enumerated as follows:

- Implementation of chemical methodologies for the formation of palladium thin films to improve adhesion onto the silicon substrate.

- Analysis of the transformation in palladium behaviour and surface morphology upon multiple reduction cycles on the palladium thin film.
- Analysis of the variation in pH of the electrolyte over long duration reduction studies performed under multiple cations.
- Introduce morphological variations in the palladium catalyst to assess the mechanisms employed for the formation of the various by-products over the course of the reduction reaction.
- Analysis of the ionic interaction with the CO molecules chemisorbed on the palladium thin films at high coverage's through its gradual desorption utilizing infrared spectroscopy.



## VII Bibliography

---

1. **NASA.** Evidence . *Global Climate Change -Vital Signs of the planet* . [Online] Earth Science Communication team - Jet Propulsion Laboratory , July 11, 2018. [Cited: July 12, 2018.] <https://climate.nasa.gov/>.
2. *High resolution carbon dioxide concentration record 650,000-800,000 years before present.* **Dieter Lüthi, Martine Le Floch, Bernhard Bereiter, Thomas Blunier, Jean-Marc Barnola, Urs Siegenthaler, Dominique Raynaud, Jean Jouzel, Hubertus Fischer, Kenji Kawamura & Thomas F. Stocker.** s.l. : Nature, 2008, Vol. 453, pp. 379-382.
3. **Yulsman, Tom.** Carbon Dioxide Hits 400 ppm- Does it Matter ? *Discover.* 2014.
4. Greenhouse gas concentrations surge to new record. *World Meteorological Organization.* [Online] October 30, 2017. [Cited: February 2, 2018.] <https://public.wmo.int/en/media/press-release/greenhouse-gas-concentrations-surge-new-record>.
5. The Paris Agreement. *United Nations Framework Convention on Climate Change.* [Online] 2014. [http://unfccc.int/paris\\_agreement/items/9485.php](http://unfccc.int/paris_agreement/items/9485.php).
6. **J.G.J.Olivier, K.M.Schure and J.A.H.W.Peters.** *Trends in Global CO<sub>2</sub> and otal Greenhouse Gas Emissions* . Netherlands : PBL Netherlands Environmental Assessment Agency , 2017.
7. **IREN.** *Renewable Capacity statistics 2017.* Abu Dhabi : s.n., 2017.
8. **State of Green .** IEA-Global Renewable Electricity Generation SEt to Grow more thsn one-third by 2022. *State of Green* . [Online] November 07, 2017. [Cited: July 13, 2018.] <https://stateofgreen.com/en/partners/state-of-green/news/iea-global-renewable-electricity-generation-set-to-grow-more-than-one-third-by-2022/>.
9. **SLAC and Standford University .** CO<sub>2</sub> Reduction . *SUNCAT- Center for Interface Science and Catalysis.* [Online] [Cited: July 18, 2018.] <https://suncat.stanford.edu/research/co2-reduction>.
10. **Kortlever, Ruud.** *Selective and efficient electrochemical CO<sub>2</sub> reduction on nanostructured catalysts.* Liden : Catalysis and Surface Chemistry Division, Leiden Institute of Chemistry, Faculty of Science, Leiden University, 2015.
11. **Liang, Zheng.** Electrochemical Reduction of Carbon Dioxide into Useful Fuels. *Department of Physics, Standford University* . [Online] Stanford , September 14, 2017. [Cited: July 18, 2018.] <http://large.stanford.edu/courses/2016/ph240/liang1/>.
12. **Luciterua.** Palladium Metal Cube 99.95%. *Luciteria.* [Online] Luciteria. [Cited: July 18, 2018.] <http://luciteria.com/metal-cubes/palladium-metal-cube-9995>.
13. *Rational Design of Efficient Palladium Catalysts for Electroreduction of carbon dioxide to Formate.* **Anna Klinkova, Phil De Luna, Cao-Thang Dinh, Oleksandr Voznyy, Egor M. Larin, Eugenia Kumacheva, and Edward H. Sargent.** 12, s.l. : ACS Catalysis, 2016, Vol. 6, pp. 8115-8120.
14. *Formic Acid electrooxidation on Pd in acidic solutions studied by surface - enhanced infrared absorption spectroscopy.* **Hiroto Miyake, Tatsuhiko Okada, Gabor Samjeske and Masatoshi Osawa.** 25, s.l. : Royal Society of Chemistry, 2008, Vol. 0, pp. 3662-3669.
15. *Pd-Containing Nanostructures for electrochemical CO<sub>2</sub> Reduction Reaction.* **Dunfeng Gao, Hu Zhou, FAn Cai , Jianguo Wang, Guoxion Wang, and Xinhe Bao.** 2, s.l. : ACS Publications , 2018, ACS Catalysis, Vol. 8, pp. 1510-1519.

16. *Switchable CO<sub>2</sub> electroreduction via engineering active phases of Pd nanoparticles.* **Dunfeng Gao, Hu Zhou, Fan Cai, Dongniu Wang, Yongfeng Hu, Bei Jiang, Wen-Bin Cai, Xiaoqi Chen, Rui Si, Fan Yang, Shu Miao, Jianguo Wang, Guoxiong Wang and Xinhe Bao.** 66, s.l. : Springer Link, 2017, Vol. 10, pp. 2181-2191.
17. *Size-Dependent Electrocatalytic Reduction of CO<sub>2</sub> over Pd nanoparticles.* **Dunfeng Gao, Hu Zhou, Jing Wang, Shu Miao, Fan Yang, Guoxiong Wang, Jianguo Wang, and Xinhe Bao.** 13, s.l. : ACS Publications, 2015, Vol. 137, pp. 4288-4291.
18. **Hardy, Norm.** Thin Film Deposition by Sputtering : Essential Basics . *Semicore*. [Online] Semicore Equipment Inc, October 07, 2013. [Cited: July 26, 2018.] <http://www.semicore.com/news/70-thin-film-deposition-sputtering>.
19. **Angstrom Sciences .** Magnetron Sputtering. *Amstrong Sciences*. [Online] [Cited: July 26, 2018.] <https://www.angstromsciences.com/magnetron-sputtering-deposition>.
20. **Almtoft, Klaus Pagh.** *Structural Characterization of Nanocrystalline thin films Grown by Magnetron Sputtering.* Physics and Astronomy, Interdisciplinary Nanoscience Center and University of Aarhus . Aarhus : s.n., 2006. PhD Thesis.
21. **L.Rohde, Allan Matthews and Suzanne.** Coatings and Surface Engineering : Physical Vapor Deposition. *Mechanical Engineers Handbook Volume3: Manufacturing and Management.* s.l. : John Wiley and Sons inc., 2015.
22. *Microstructural evolution during film growth.* **I.Petrov, P.B.Barna, L.Hultman and J.E.Greene.** 5, s.l. : American Vacuum Society, 2003, Journal of vacuum science and technology, Vol. 21, pp. S117-S127.
23. *High Rate Thick Film Growth.* **John A. Thornton.** s.l. : Annual Reviews, 1977, Annual Review of Materials Science, Vol. 7, pp. 239-260.
24. *Investigation of Hydrogen Adsorption and Absorption in palladium Thin Films.* **C.Gabrielli, P.P.Grand, A.Lasia and H.Perrot.** 11, s.l. : ECS, 2004, Journal of the Electrochemical Society, Vol. 151, pp. A19137-A1942.
25. *Thin palladium Films on silicon and Titanium.* **L.A.Harris.** 12, s.l. : ECS, 1982, Vol. 129, pp. 2689-22694.
26. *Electrochemical behavior of Palladium electrode : Oxidation, electrodisolution and ionic adsorption.* **Michal Grden, Mariusz Lukaszewski, Gregory Jerkiewicz and Andrzej Czerwinski.** s.l. : Elsevier, 2008, Vol. 53, pp. 7583-7598.
27. *The electrodisolution of base palladium in relation to the oxygen electroadsorption and electrodesorption in sulphuric acid solution.* **A.E.Bolzan, M.E.Martins and A.J.Arvia.** 1-2, s.l. : Elsevier, 1984, Vol. 172, pp. 221-233.
28. *CO<sub>2</sub> Electroreduction at Bare and Cu-Decorated Pd Pseudomorphic layers: Catalysts Tuning by controlled and Indirect supporting onto Au(111).* **Kulesza, Aneta Januszewska Rafal Jurczakowski and Pawel J.** 47, s.l. : ACS Publications, 2014, Vol. 30, pp. 14314-14321.
29. *An Electrochemical Study of the Composition of Thin, Compact Pd Oxide Films.* 24, s.l. : Royal Society of Chemistry, 1996, Vol. 92, pp. 4041-4047.
30. *Structure . Geocities.* [Online] OHBA Laboratory . [Cited: July 19, 2018.] [http://www.geocities.jp/ohba\\_lab\\_ob\\_page/structure4.html](http://www.geocities.jp/ohba_lab_ob_page/structure4.html).
31. *The role of palladium in a hydrogen economy.* **Aicheng Chen, Brian D.Adams and.** 6, s.l. : Science Direct, 2011, Materials Today , Vol. 14, pp. 282-289.
32. *Seperation of Hydrogen adsorption and absorption on Pd Thin Films.* **Lasia, Hugues Duncan and Andrzej.** 23, s.l. : Elsevier, 2008, Vol. 53, pp. 6845-6850.
33. *CO adsorption on Pd(111): the effects of temperature and pressure.* **W.Kevin Khun, Janos Szanyi and D.Wayne Goodman.** 3, s.l. : Elsevier, 1992, Vol. 274, pp. L611-L618.

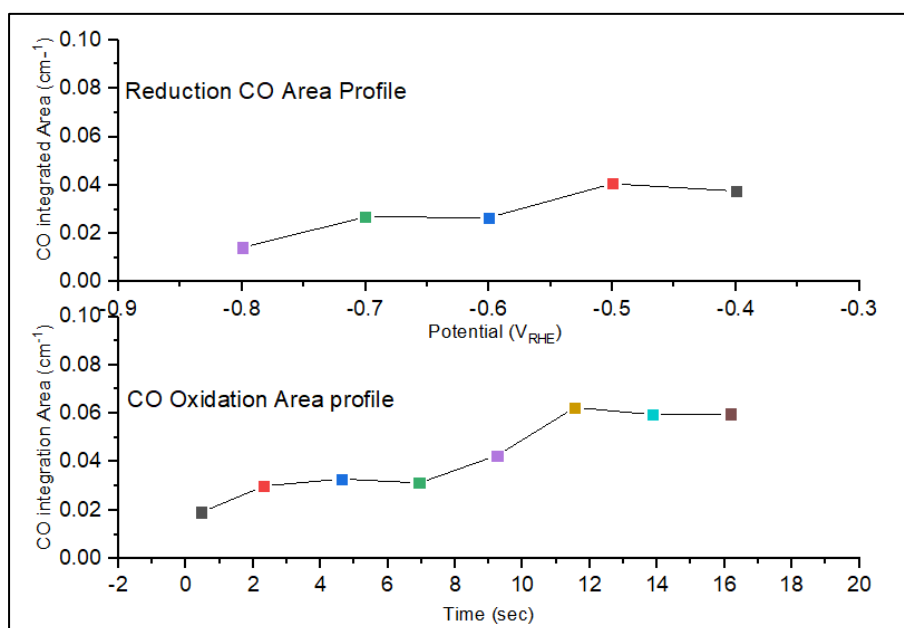
34. *The chemisorption of carbon monoxide on palladium single crystal surfaces: IR spectroscopic evidence for localised site adsorption.* **A.M.Bradshaw, F.M.Hoffmann and.** 3, s.l. : Elsevier, 1978, Vol. 72, pp. 513-535.
35. *Evidence for Inclined CO on Pd(210).* **Theodore E.Madey, John T.Yates Jr, A.M.Bradshaw and F.M.Hoffmann.** 1-3, s.l. : Elsevier, 1979, Vol. 89, pp. 370-380.
36. *CO adsorption on stepped Pd( 112) : Studies by Thermal and Electron simulated Desorption.* **R.D.Ramsier, K-W.Lee and J.T.Yates Jr.** 1-3, s.l. : Elsevier, 1995, Vol. 332, pp. 243-255.
37. *Light at the interface: the potential of attenuated total reflection infrared spectroscopy for understanding heterogeneous catalysis in water.* **Barbara Louise Mojet, Sune Dalgaard Ebbesen and Leon Lefferts.** 12, s.l. : Royal Society of Chemistry, 2010, Vol. 39, pp. 4643-4655.
38. *The influence of carbon monoxide on hydrogen absorption by thin films of palladium.* **A.Czerwinski, S.Zamponi and R.Marassi.** 1-2, s.l. : Elsevier, 1991, Vol. 304, pp. 233-239.
39. *Effect of CO on hydrogen adsorption on palladium.* **Jr., Nguyen Van Hieu and J.H.Craig.** 1, s.l. : Elsevier, 1985, Vol. 160, pp. L483-L487.
40. *Adsorption and coadsorption of carbon monoxide and hydrogen on Pd(111).* **G.M.Bliznakov, M.P.Kiskinova and.** 1, s.l. : Elsevier, 1982, Vol. 123, pp. 61-76.
41. *Electrochemical CO<sub>2</sub> reduction: Electrocatalyst, reaction mechanism, and process engineering.* **Jiao, Qi Lu and Feng.** s.l. : Elsevier, 2016, Vol. 29, pp. 439-456.
42. *Electrocatalytic CO<sub>2</sub> Reduction to Formate at Low overpotentials on electrodeposited palladium films: stabilized performance by suppression of CO formation.* **Dr. Fengling Zhou, Dr. Haitao Li , Dr. Maxime Fournier and Prof. Douglas R. MacFarlane.** 7, s.l. : Wiley Online Library, 2017, Vol. 10, pp. 1509-1516.
43. *Pd-Containing Nanostructures for Electrochemical CO<sub>2</sub> Reduction Reaction.* **Dunfeng Gao, Hu Zhou, Fan Cai, Jian-guo Wang, Guoxiong Wang, and Xinhe Bao.** 2, s.l. : ACS publications, 2018, Vol. 8, pp. 1510-1519.
44. *Electrochemical promotion of catalysis over Pd nanoparticles for CO<sub>2</sub> reduction.* **Fan Cai, Dunfeng Gao, Hu Zhou, Guoxiong Wang, Ting He, Huimin Gong, Shu Miao, Fan Yang, Jianguo Wang and Xinhe Bao.** 4, s.l. : Royal Society of Chemistry, 2017, Vol. 8, pp. 2569-2573.
45. *Electrochemical reduction of carbon dioxide on hydrogenstoring materials: Part 1. The effect of hydrogen absorption on the electrochemical behavior on palladium electrodes.* **Kiyomi Ohkawa, Kazuhito Hashimoto and Akira Fujishima.** 1-2, s.l. : Elsevier, 1993, Vol. 345, pp. 445-456.
46. *pH effect on electrocatalytic reduction of CO<sub>2</sub> over Pd and Pt nanoparticles.* **Dunfeng Gao, Jing Wang, Haihua Wu, Xiaole Jiang, Shu Miao, Guoxiong Wang and Xinhe Bao.** s.l. : Elsevier, 2015, Vol. 55, pp. 1-5.
47. *Hydrolysis of Electrolyte Cations Enhances the electrochemical Reduction of CO<sub>2</sub> over Ag and Cu.* **Meenesh R. Singh, Youngkook Kwon, Yanwei Lum, Joel W. Ager and Alexis T. Bell.** 39, s.l. : ACS Publications, 2016, Vol. 138, pp. 13006-13012.
48. *Catalysts and Reaction Pathways for the Electrochemical Reduction of Carbon Dioxide.* **Rud Kortlever, Jing Shen, Klaas JanP. Schouten, Federico Calle-Vallejo and Marc T.M.Koper.** 20, s.l. : ACS Publications, 2015, Vol. 6, pp. 4073-4082.
49. *Electrochemical conversion of CO<sub>2</sub> to useful chemicals: current status, remaining challenges and future opportunities.* **Huei-Ru "Molly" Jhong, Sichao Ma, and Paul JA Kenis.** 2, s.l. : Elsevier, 2013, Current Opinion in Chemical Engineering, Vol. 2, pp. 191-199.

50. *Theoretical Insights into a CO Dimerization Mechanism in CO<sub>2</sub> Electoreduction*. **Joseph H. Montoya, Chuan Shi, Karen Chan and Jens K. Nørskov**. 11, s.l. : American Chemical Society, 2015, Vol. 6, pp. 2032-2037.
51. *Effect of KHCO<sub>3</sub> Concentration on Electrochemical Reduction of CO<sub>2</sub> on Copper Electrode*. **Heng Zhonga, d,z, Katsushi Fujiib,e and Yoshiaki Nakano**. 9, s.l. : ECS, 2017, Journal of the Electrochemical Society , Vol. 164, pp. F923-F927.
52. *Infrared Spectroscopy*. **Curtis L. Putzig, M. Anne. Leugers, Marianne L. McKelvy, Gary E. Mitchell, Richard A. Nyquist, Richard R. Papenfuss, and Lori. Yurga**. 12, s.l. : ACS Publications, 1994, Vol. 66, pp. 26-66.
53. **Lazzarino, F., Krishtab, M., Tahara, S., & Baklanov, M.** *Ultra-low k dielectric and plasma damage control for advanced technology nodes (10-nm and below)*. FACULTY OF ELECTRICAL AND COMPUTER ENGINEERING, TECHNISCHE UNIVERSITÄT DRESDEN. 2013. Master Thesis.
54. **Sanchonx**. FTIR Interferometer.png. *WIKIMEDIA COMMONS*. [Online] December 23, 2011. [Cited: July 23, 2018.] [https://commons.wikimedia.org/wiki/File:FTIR\\_Interferometer.png](https://commons.wikimedia.org/wiki/File:FTIR_Interferometer.png).
55. *Dynamic Processes in electrochemical eactions Studied by Surface- Enhanced Infrared Absorption Spectroscopy (SEIRAS)*. **Masatoshi, Osawa**. 12, s.l. : CSJ Journals, 1997, Vol. 70, pp. 2861-2880.
56. *Adhesion -induced Orientation of MDI Native Metals - Model Experients* . **Christophe Nies, Kevin Belener and Wulff Possart**. 2014.
57. **Pike Technologies**. ATR Crystal Selection . *Pike Technologie* . [Online] 2018. [Cited: july 26, 2018.] <http://www.piketech.com/ATR-Crystal-Selection.html>.
58. **Steve D. Barrett, Christopher A. Lucas, and Rasmita Raval**. *Photon Spectroscopies. Surface and Interface Science*. s.l. : Wiely-VCH VERlag GmbH and Co., 2012.
59. *Silver island films for surface-enhanced infrared absorption spectroscopy: Effect of island morphology on the absoption enhancement*. **Yuji Nishikawa, Tadahiro Nagasawa and Kunihiro Fujiwara**. 1, s.l. : Elsevier, 1993, Vol. 6, pp. 43-53.
60. *Surface-Enhanced Infrared Absorptlon of p -Nltrobenzolc Acid Deposited on Silver Island Films: Contribution of Electromagnetic and Chemical Mechanisms*. **Masatoshi Osawa, and Masahiko Ikeda'**. 24, s.l. : ACS publications , 1990, Vol. 95, pp. 9914-9919.
61. **Mathew Mate, Brian E. Bent and A.Somorjai**. *Vibrational Spectroscopy of Hydrogen on Metals. Hydrogen Effects in Catalysis: Fundamentals and Practical Applications*. s.l. : Marcel Dekker INC., 1988.
62. *Structural and Spectroelectrochemical Study of Carbonate and Bicarbonate Adsorbed on Pt(111) and Pd/Pt(111) Electrodes*. **Antonio Berna, Antonio Rodes,Juan M. Feliu, Francesc Illas , Alfred Gil, Anna Cltet and Josep M.Ricart**. 24, s.l. : American Chemical Society, 2004, Vol. 108, pp. 17928-17939.
63. **PREVAC**. Magnetron Sputtering System [project 229]. *PREVAC*. [Online] 2012. [Cited: July 15, 2018.] <https://www.prevac.eu/en/2,offer/33,deposition-systems/65,magnetron-sputtering-system.html>.
64. *Quenching H<sub>2</sub> evolution on Pd-Au alloys for a more efficient CO<sub>2</sub> reduction to CO than Au at low overpotentials*. **Marco Valenti, Nitin P. Prasad, Ming Ma, Liangyong Chu, Divya Bohra, Recep Kas, Sixto Gimenez , Juan Bisquert , Bernard Daml & Wilson A. Smith**. 2018.
65. **R.R.L. De Oliveira, D.A.C. Albuquerque, T.G.S. Cruz, F.M. Yamaji and F.L. Leite**. *Measurement of the Nanoscale Roughness by Atomic Force Microscopy: Basic*

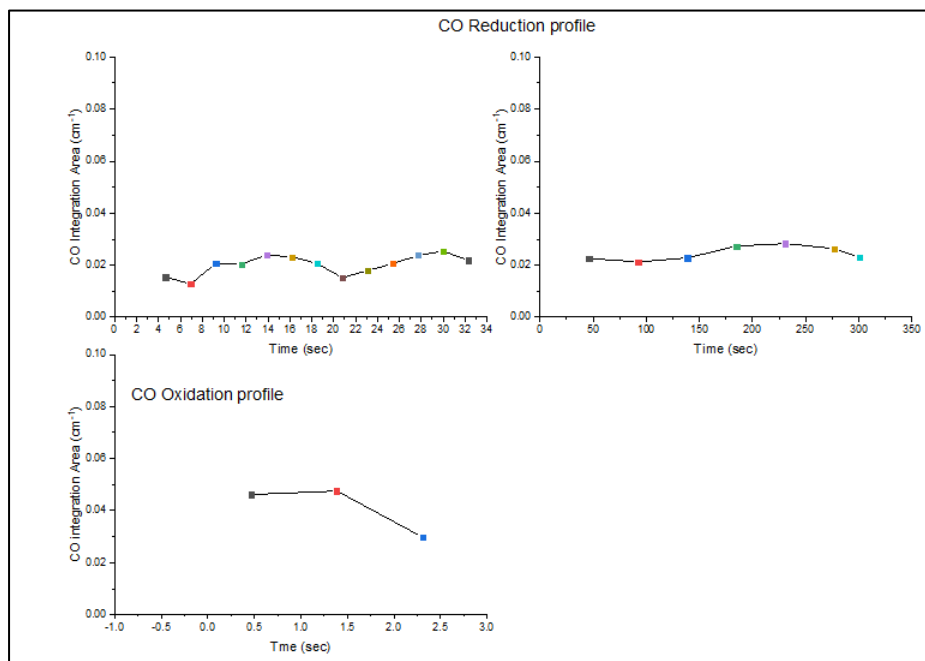


- Principles and Applications . *Atomic Force Microscopy - Imaging, Measuring and Manipulating Surfaces at the Atomic Scale*. s.l. : Intech Open, 2012.
66. *Study of anomalous infrared properties of nanomaterials through effective medium Theory*. **Zhang-Fei Su, Shi-Gang Sun, Chen-Xu Wu, and Zhi-Ping Cai**. 4, s.l. : American Institute of Physics, 2008, Vol. 129.
67. *Infrared Spectra of Carbon Monoxide Chemisorbed on Metal Films: A Comparative Study*. **Pritchard, A. M. Bradshaw and J.** 1525, s.l. : The Royal Society Publishing, 1970, Vol. 316, pp. 167-183.
68. *Synthesis of thin film AuPd alloys and their investigation for electrocatalytic CO<sub>2</sub> reduction*. **Christopher Hahn, David N. Abram, Heine A. Hansen, Toru Hatsukade, Ariel Jackson, Natalie C. Johnson, Thomas R. Hellstern, Kendra P. Kuhl, Etosha R. Cave, Jeremy T. Feaster and Thomas F. Jaramillo**. 40, s.l. : The Royal Society of Chemistry, 2015, Vol. 3, pp. 20185-20194.
69. *The oxidation of carbon monoxide on platinum {111}: Reflection-absorption infrared spectroscopy*. **A.King, R.A.Shigeishi and David**. 2, s.l. : Elsevier, 1978, Vol. 75, pp. L397-L400.
70. **Korzeniewski, Carol**. Vibrational Coupling Effects on Infrared Spectra of Adsorbates on Electrodes. *Interfacial Electrochemistry - Theory, Experiments and Applications*. s.l. : Marcel Dekker Inc., 1999.
71. *Surface (Electro)chemistry of CO<sub>2</sub> on Pt Surface: An in Situ Surface-Enhanced Infrared Absorption Spectroscopy Study*. **Yu Katayama, Livia Giordano, Reshma R. Rao, Jonathan Hwang, Hiroki Muroyama, Toshiaki Matsui, Koichi Eguchi and Yang Shao-Horn**. 23, s.l. : ACS Publications, 2018, Vol. 122, pp. 12341-12349.
72. *Electrochemical Reduction of CO, on Hydrogen-enriched and Hydrogen -depleted surface*. **Hideaki Yoshitake, Koji Takahashi and Ken-ichiro Ota**. 1, s.l. : Royal Society of Chemistry, 1994, Vol. 90, pp. 155-159.
73. *Improving Hydrogen Evolution Reaction Activity of Palladium By Ruthenium*. **Lulu Zhang, Chenkai Feng and Minhua Shao**. s.l. : The Electrochemical Society, 2018, Meeting Abstracts, Vol. 29, pp. 1701-1701.
74. *Trends with coverage and pH in Stark tuning rates for CO on Pt(1 1 1) electrodes*. **B.Anderson, JamalUddinAlfred**. s.l. : Elsevier, 2013, Vol. 108, pp. 398-403.
75. *Poisoning of surface hydrogen processes on a Pd electrode during electrochemical reduction of carbon dioxide*. **Hideaki Yoshitake, Takashi Kikkawa, Go Mutt, Ken-ichiro Ota**. 1-2, s.l. : Elsevier, 1995, Vol. 369, pp. 491-498.
76. *Promoter Effects of Alkali Metal Cations on the Electrochemical Reduction of Carbon Dioxide*. **Joaquin Resasco, Leanne D. Chen, Ezra Clark, Charlie Tsai, Christopher Hahn , Thomas F. Jaramillo, Karen Chan, and Alexis T. Bell**. 32, s.l. : Journal of the American Chemical Society, 2017, Vol. 139, pp. 11277-11287.
77. *Influence of cation adsorption on the kinetics of electrode processes*. **Frumkin, A. N.** s.l. : Royal Society of Chemistry, 1958, Transactions of the Faraday Society , Vol. 55.
78. *Formic acid electrooxidation on Pd in acidic solutions studied by surface-enhanced infrared absorption spectroscopy*. **Hiroto Miyake, Tatsuhiko Okada, Gabor Samjeské and Masatoshi Osawa**. 25, s.l. : Royal Society of chemistry, 2008, Vol. 10, pp. 3662-3669.

## Appendix

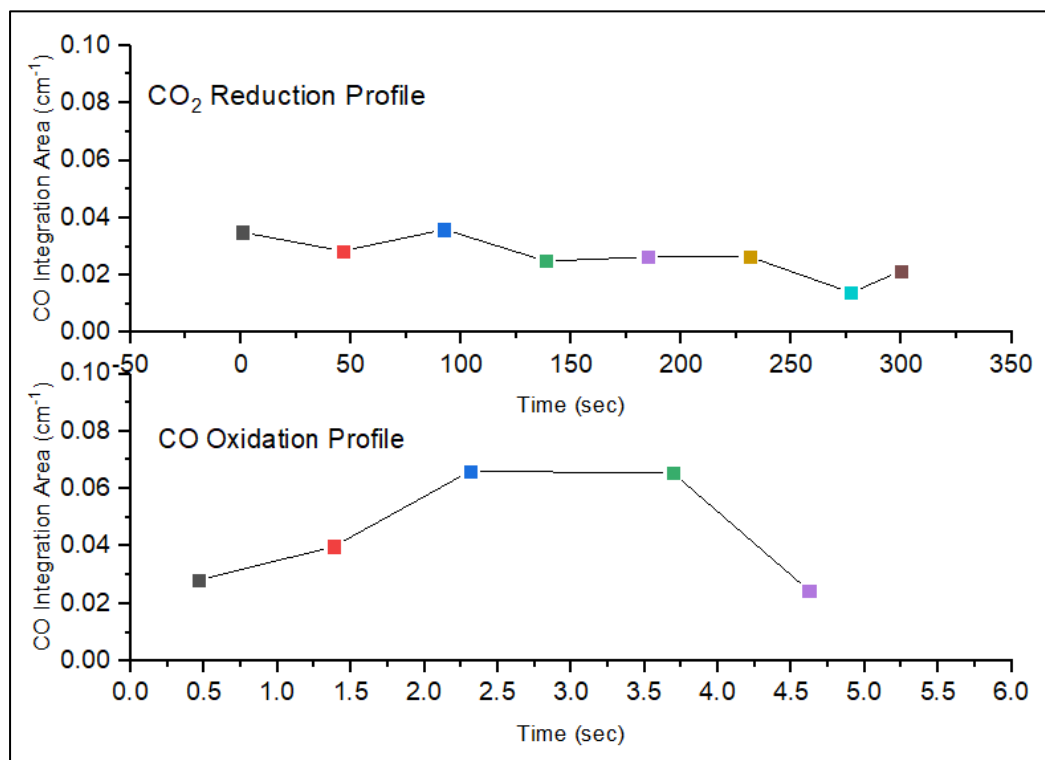


Appendix 1- The area profile observed during the CO<sub>2</sub> reduction and CO oxidation reaction during the dynamic CA study under the CO<sub>2</sub> saturated 0.1 M KHCO<sub>3</sub> solution

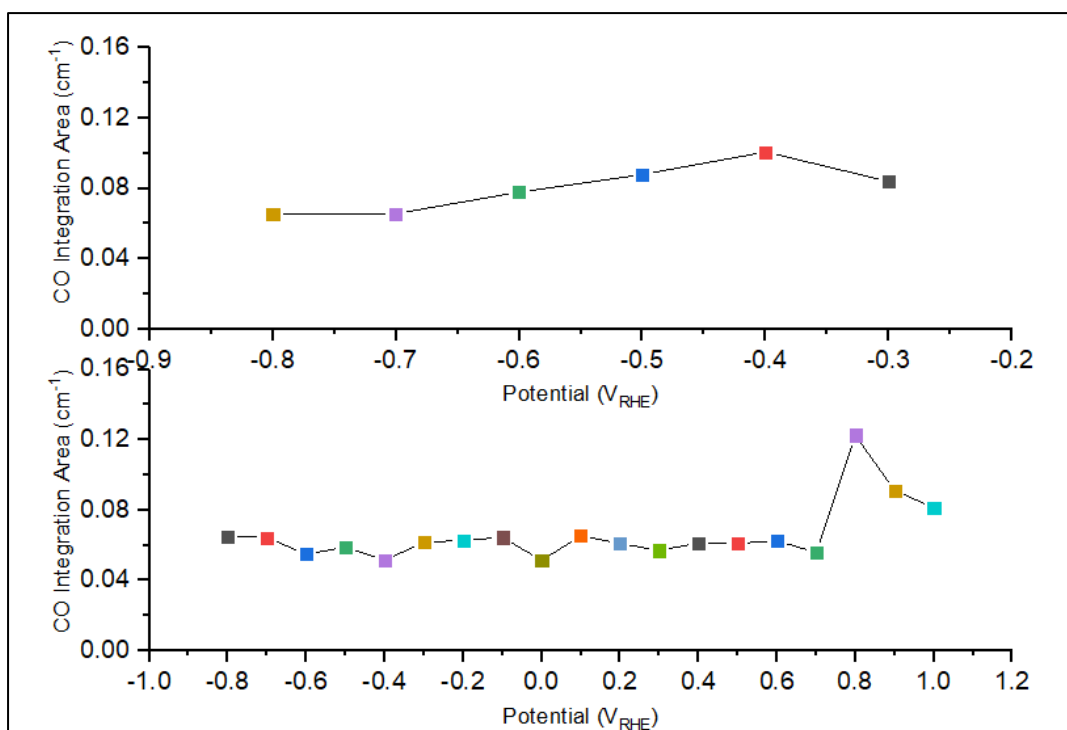


Appendix 2 - The area profile observed during the CO<sub>2</sub> reduction and CO oxidation reaction during the -0.3 V 5 min CA study under the CO<sub>2</sub> saturated 0.1 M KHCO<sub>3</sub> solution

## In-Situ Infrared Spectroscopic Studies Of Palladium Thin films during CO<sub>2</sub> Electro-Reduction

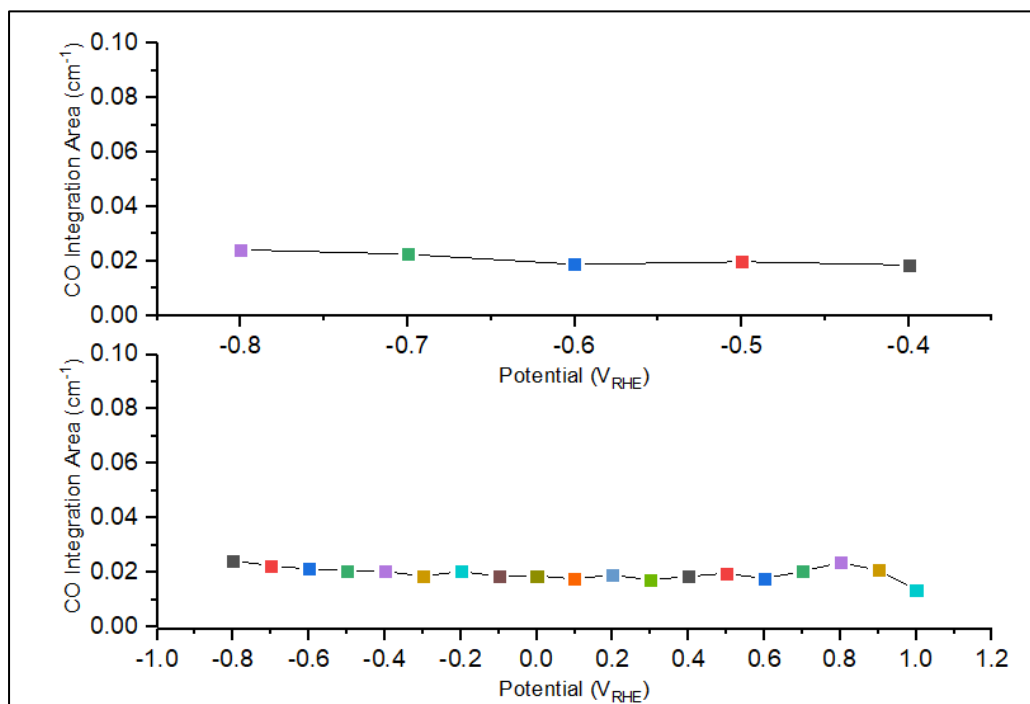


Appendix 3- The area profile observed during the CO<sub>2</sub> reduction and CO oxidation reaction during the -0.5 V 5 min CA study under the CO<sub>2</sub> saturated 0.1 M KHCO<sub>3</sub> solution

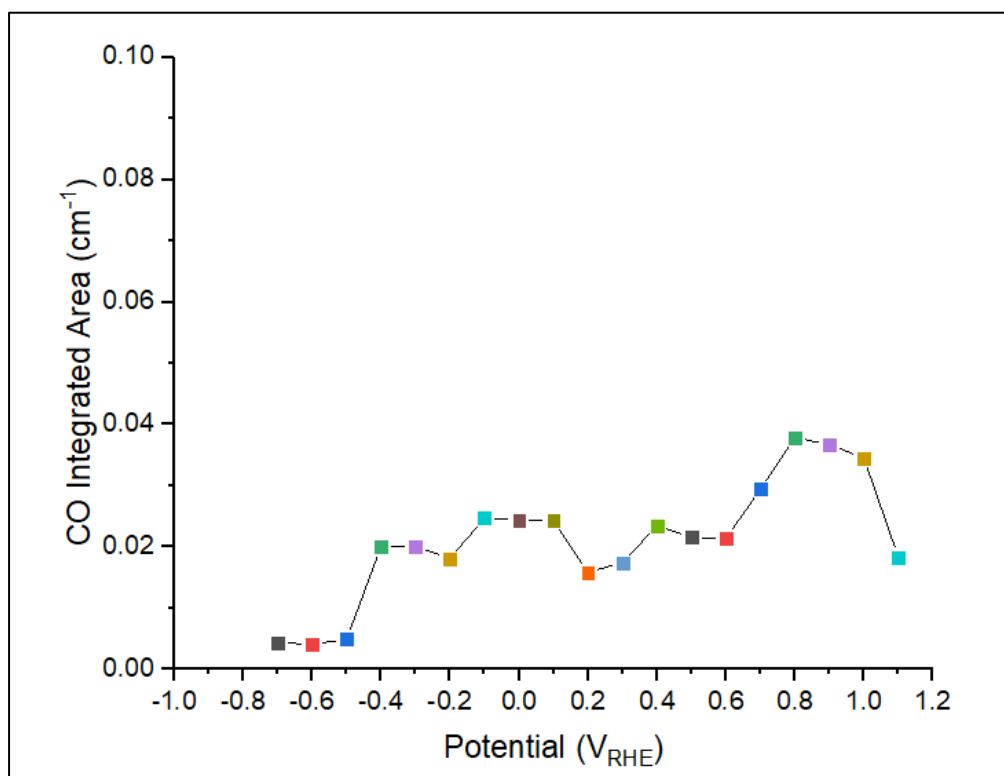


Appendix 4- The area profile observed during the CO<sub>2</sub> reduction reaction during the 10 mVpers CV study under the CO<sub>2</sub> saturated 0.1 M KHCO<sub>3</sub> solution

## In-Situ Infrared Spectroscopic Studies Of Palladium Thin films during CO<sub>2</sub> Electro-Reduction



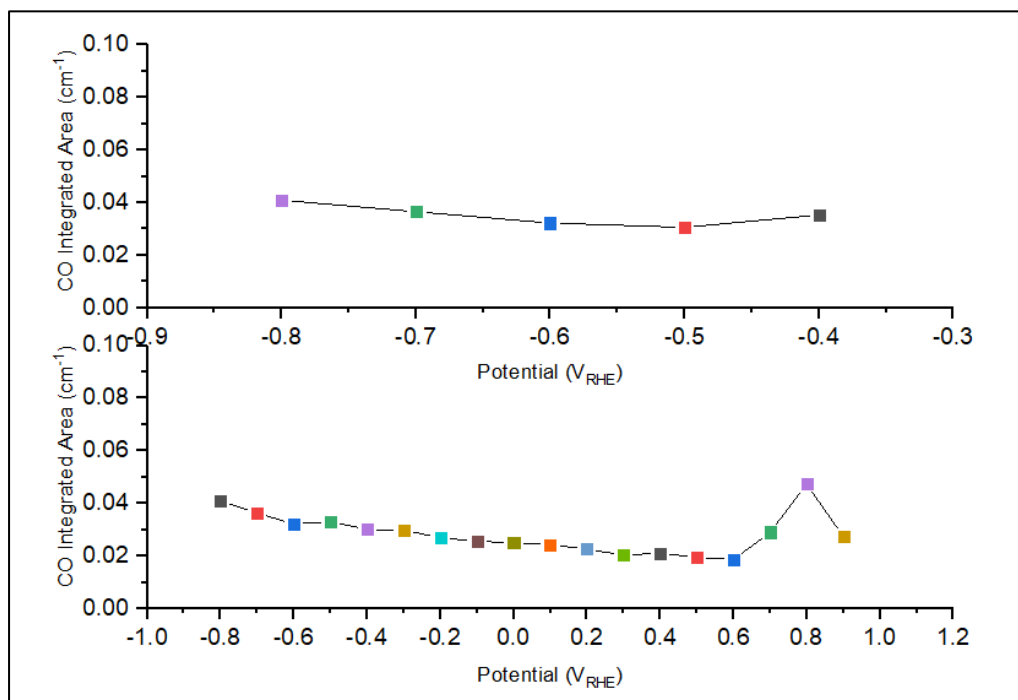
Appendix 5- The area profile observed during the CO<sub>2</sub> reduction reaction during the 2 mVpers study under the CO<sub>2</sub> saturated 0.1 M KHCO<sub>3</sub> solution



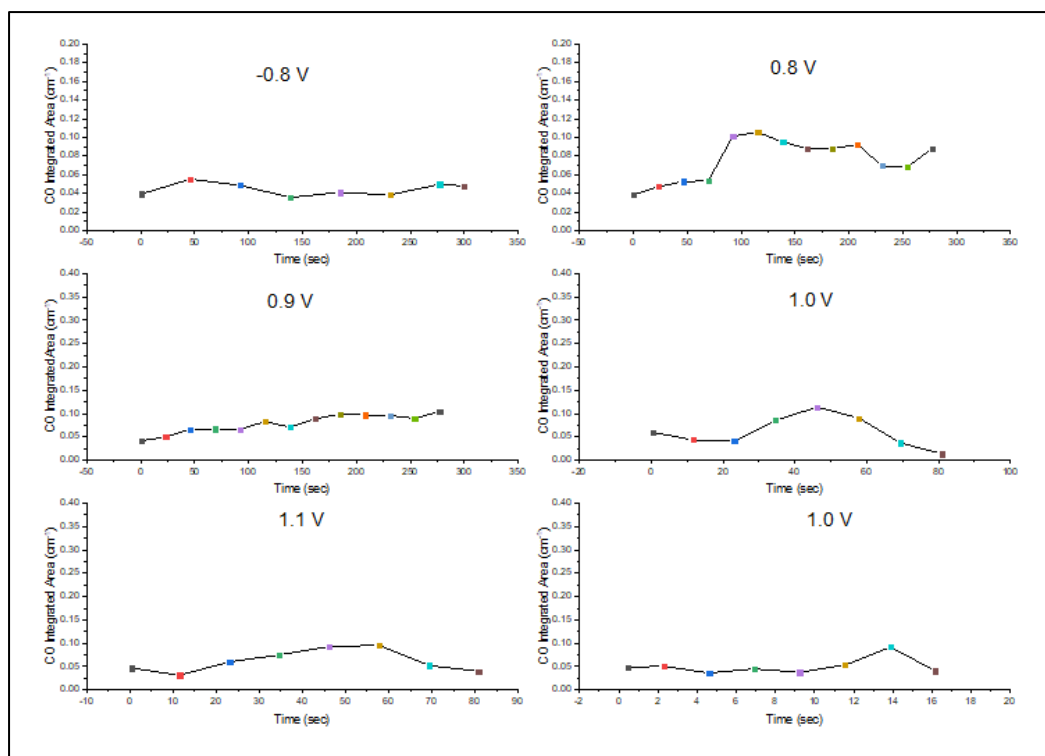
Appendix 6- The area profile observed during the N<sub>2</sub> reduction reaction during the 10 mVpers study under the CO<sub>2</sub> saturated 0.1 M KHCO<sub>3</sub> solution



## In-Situ Infrared Spectroscopic Studies Of Palladium Thin films during CO<sub>2</sub> Electro-Reduction

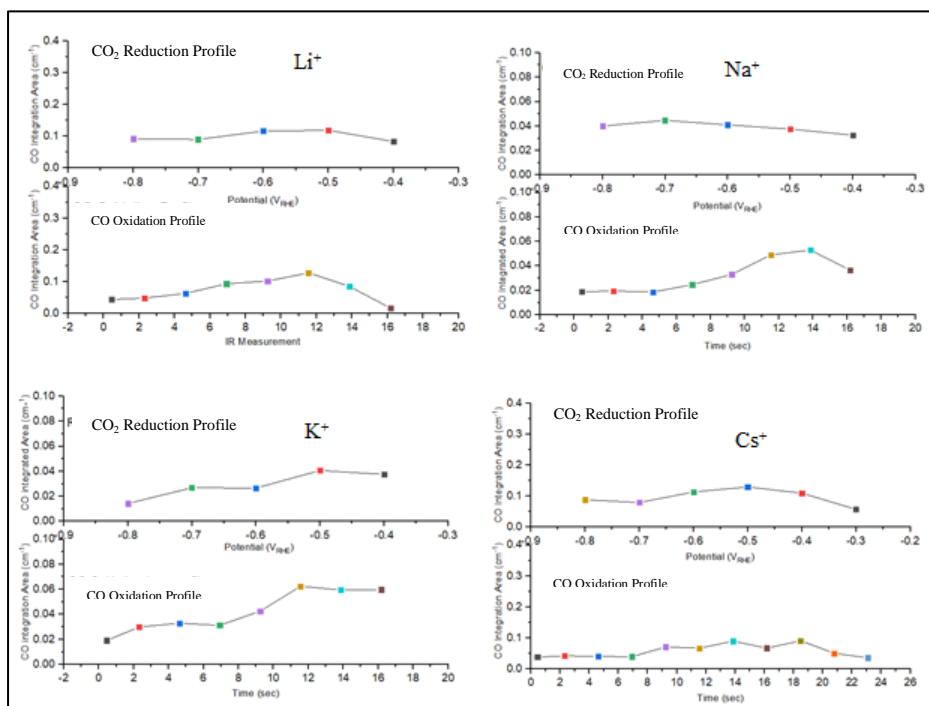


Appendix 7- The area profile observed during the N<sub>2</sub> reduction reaction during the 2 mVpers study under the CO<sub>2</sub> saturated 0.1 M KHCO<sub>3</sub> solution

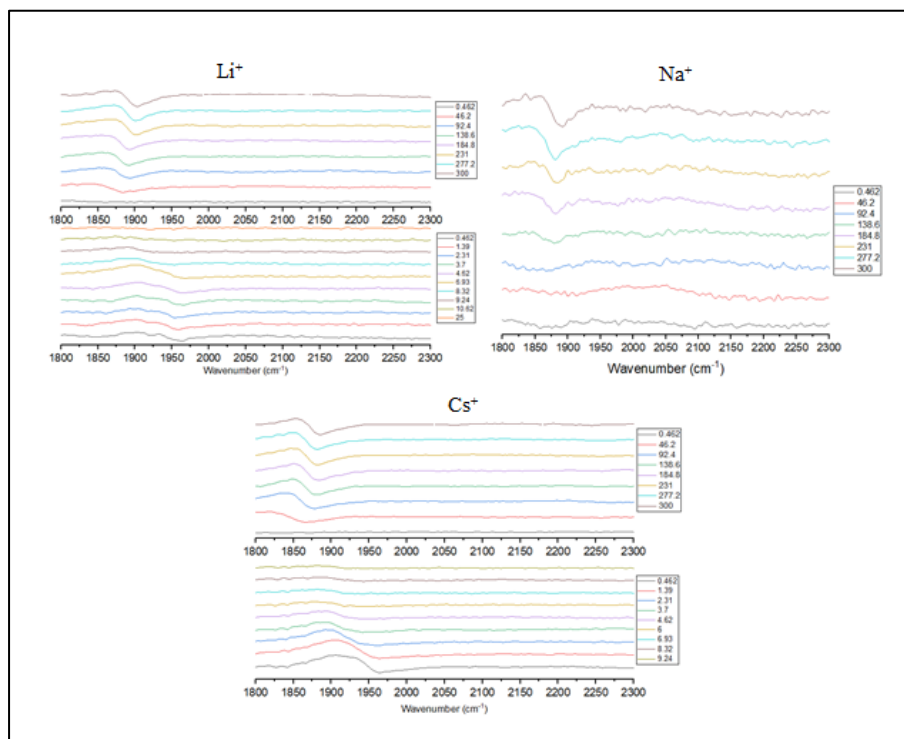


Appendix 8- The area profile observed during the CO<sub>2</sub> reduction reaction during the -0.8 V 5 min CA study under the CO<sub>2</sub> saturated 0.1 M KHCO<sub>3</sub> solution followed by the CO oxidation study at 0.8 V, 0.9 V, 1.0 V, 1.1 V and 1.2 V over the 5 min study

# In-Situ Infrared Spectroscopic Studies Of Palladium Thin films during CO<sub>2</sub> Electro-Reduction

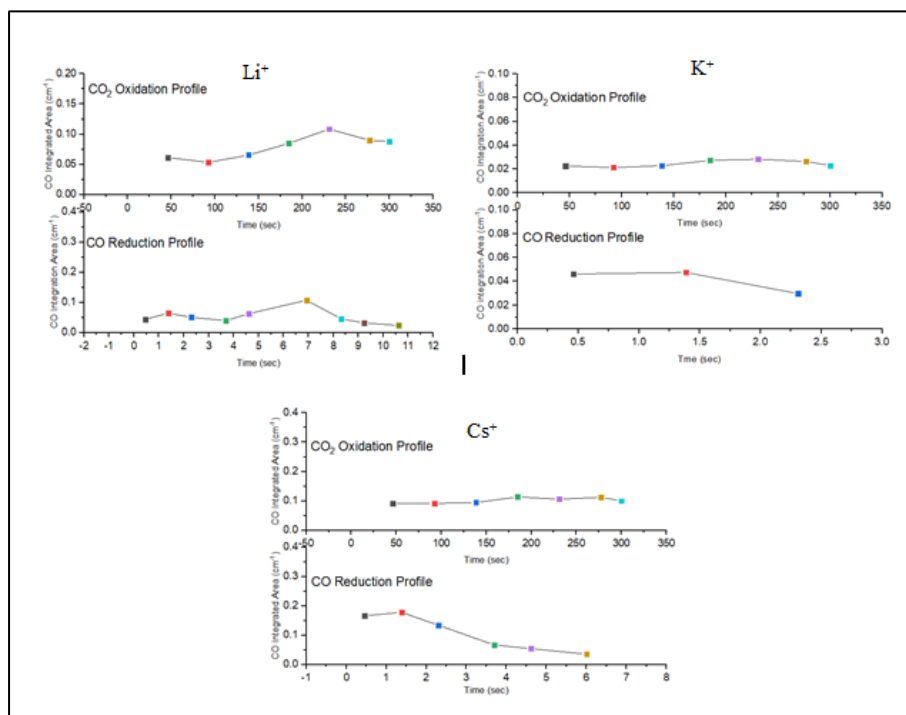


Appendix 9- The area profile observed during the CO<sub>2</sub> reduction and CO oxidation reaction during the dynamic CA study under the CO<sub>2</sub> saturated 0.1 M Li/Na/K/CsHCO<sub>3</sub> solution

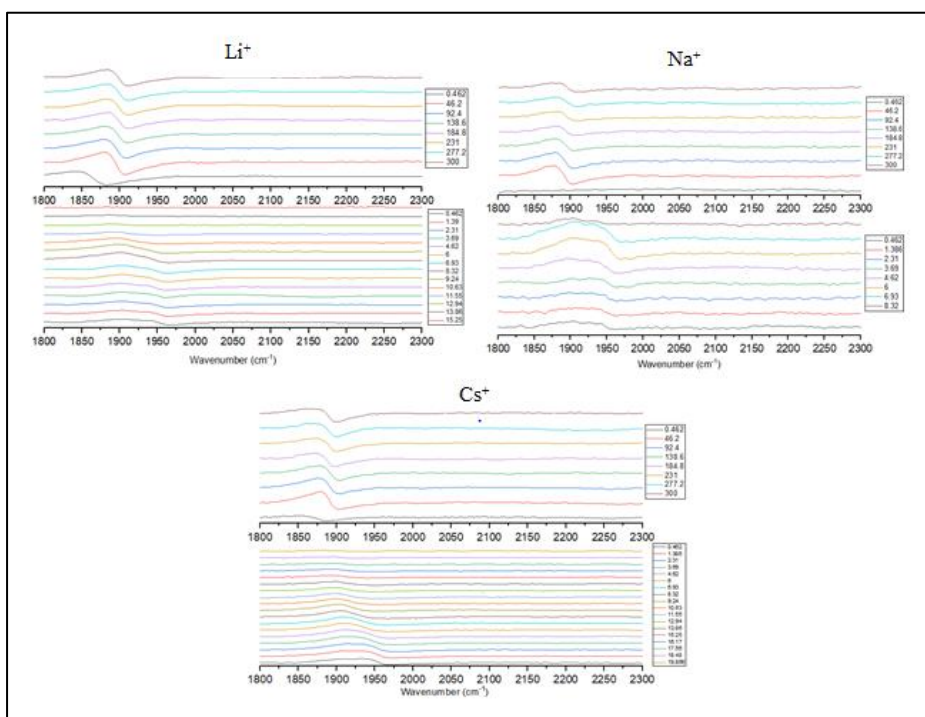


Appendix 10- The IR measurements between 1800 cm<sup>-1</sup> and 2300 cm<sup>-1</sup> observed during the CO<sub>2</sub> reduction (1) and CO oxidation(2) reaction during the -0.3 V CA study under the CO<sub>2</sub> saturated 0.1 M Li/Na/CsHCO<sub>3</sub> solution

# In-Situ Infrared Spectroscopic Studies Of Palladium Thin films during CO<sub>2</sub> Electro-Reduction

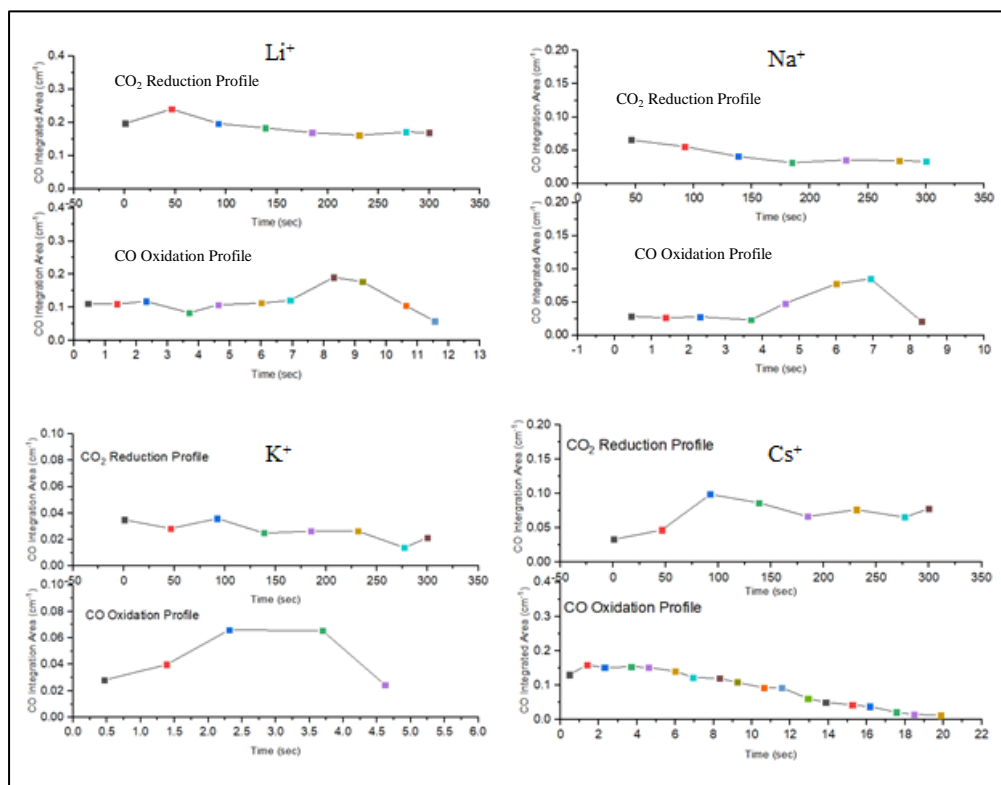


Appendix 11- The area profile observed during the CO<sub>2</sub> reduction and CO oxidation reaction during the -0.3 V CA study under the CO<sub>2</sub> saturated 0.1 M Li/Na/K/CsHCO<sub>3</sub> solution



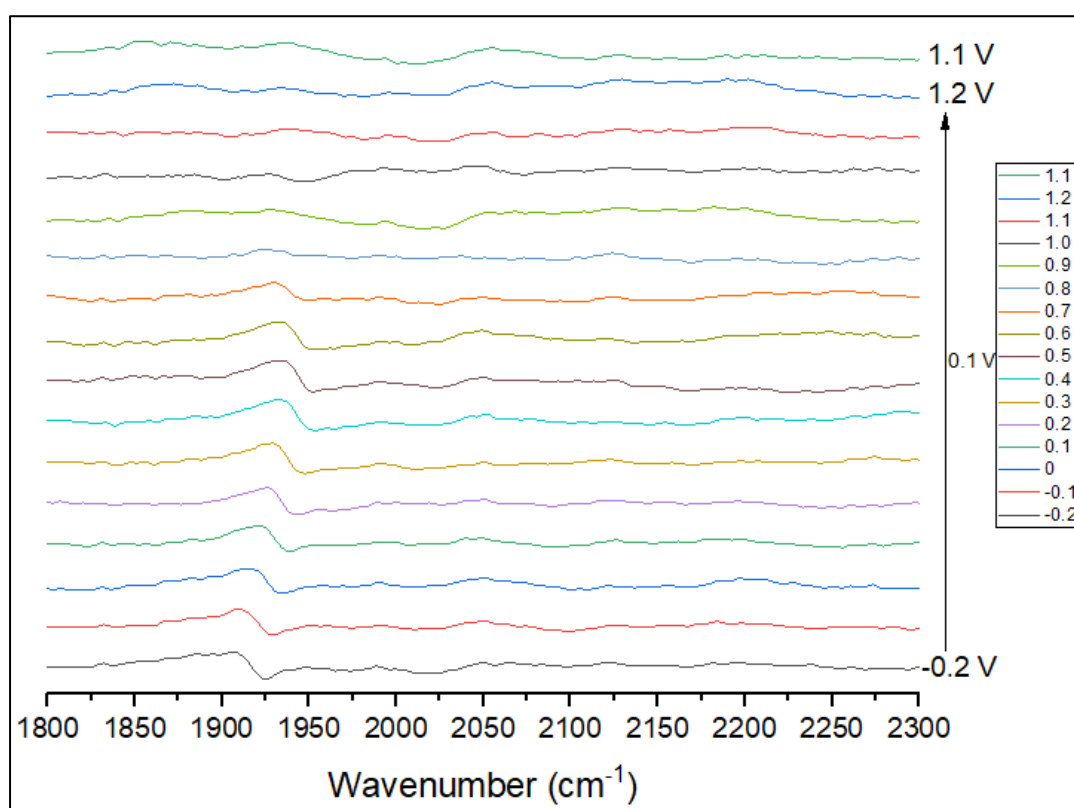
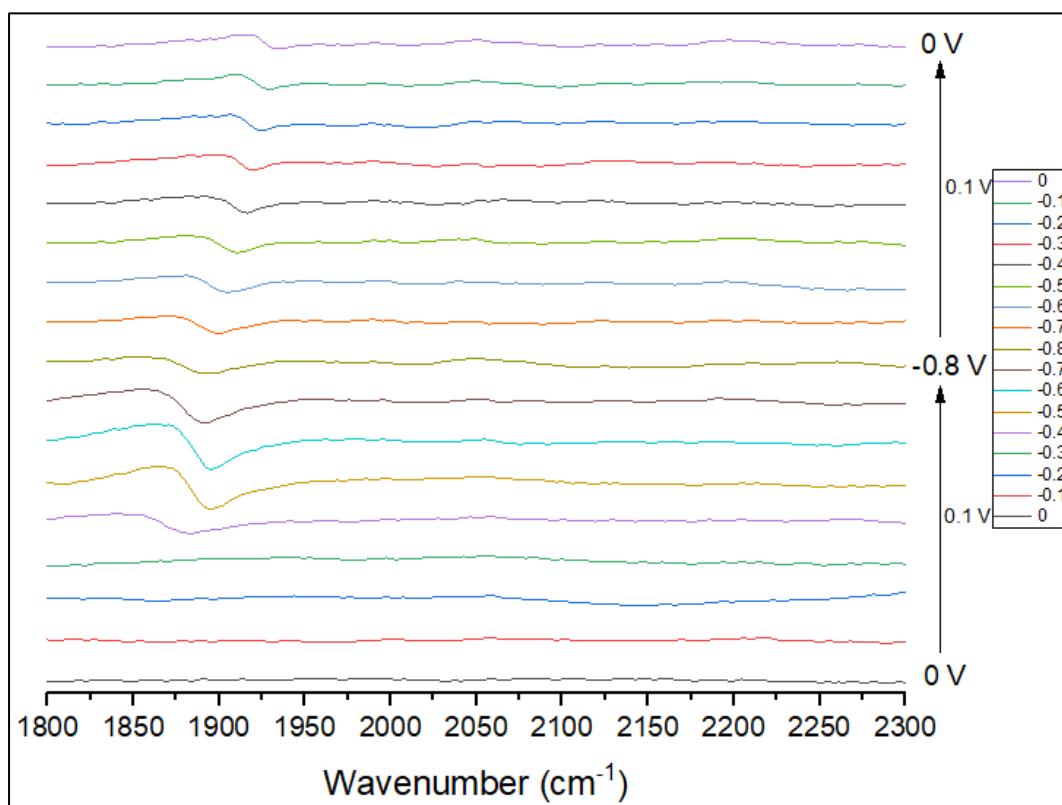
Appendix 12- The IR measurements between 1800 cm<sup>-1</sup> and 2300 cm<sup>-1</sup> observed during the CO<sub>2</sub> reduction (1) and CO oxidation(2) reaction during the -0.5 V CA study under the CO<sub>2</sub> saturated 0.1 M Li/Na/CsHCO<sub>3</sub> solution

## In-Situ Infrared Spectroscopic Studies Of Palladium Thin films during CO<sub>2</sub> Electro-Reduction



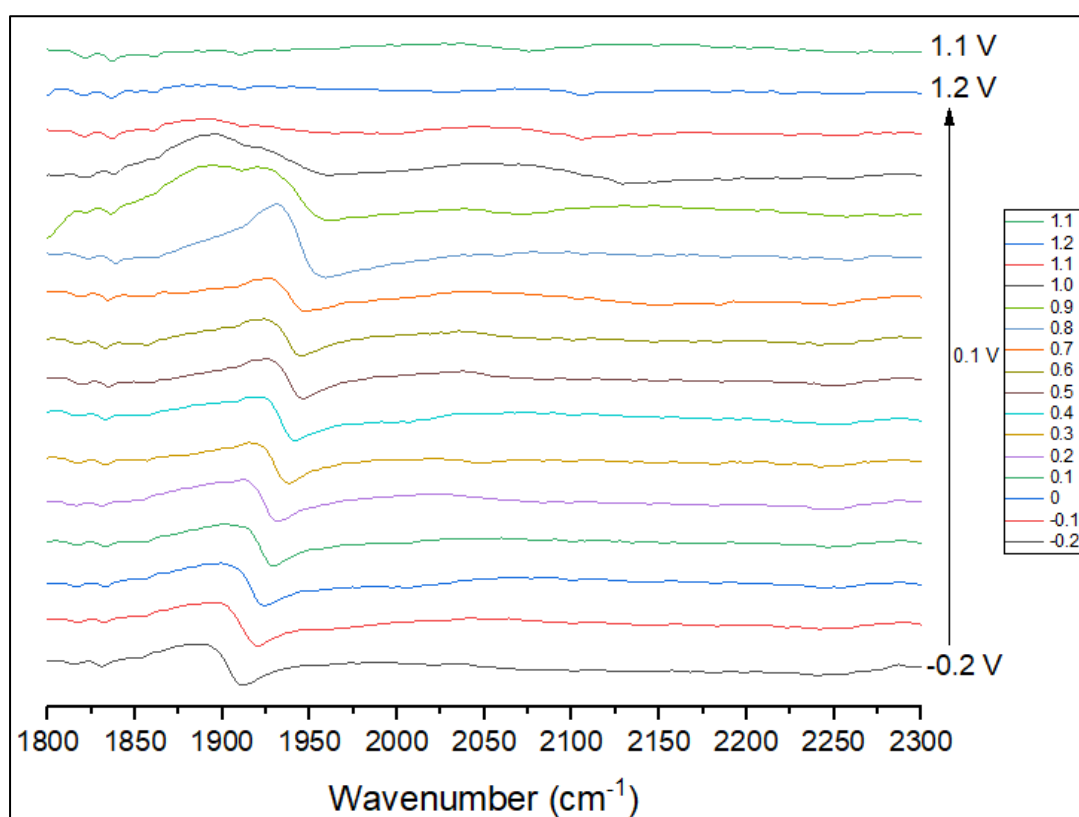
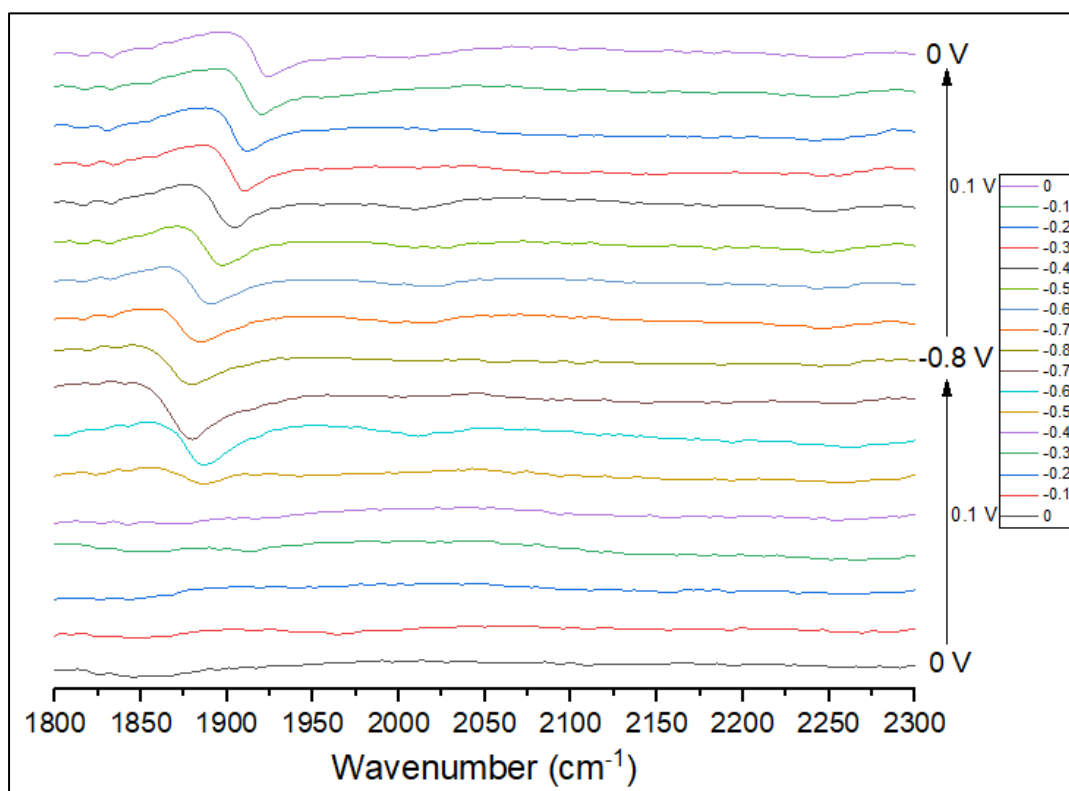
Appendix 13- The area profile observed during the CO<sub>2</sub> reduction and CO oxidation reaction during the -0.5 V CA study under the CO<sub>2</sub> saturated 0.1 M Li/Na/K/CsHCO<sub>3</sub> solution

## In-Situ Infrared Spectroscopic Studies Of Palladium Thin films during CO<sub>2</sub> Electro-Reduction



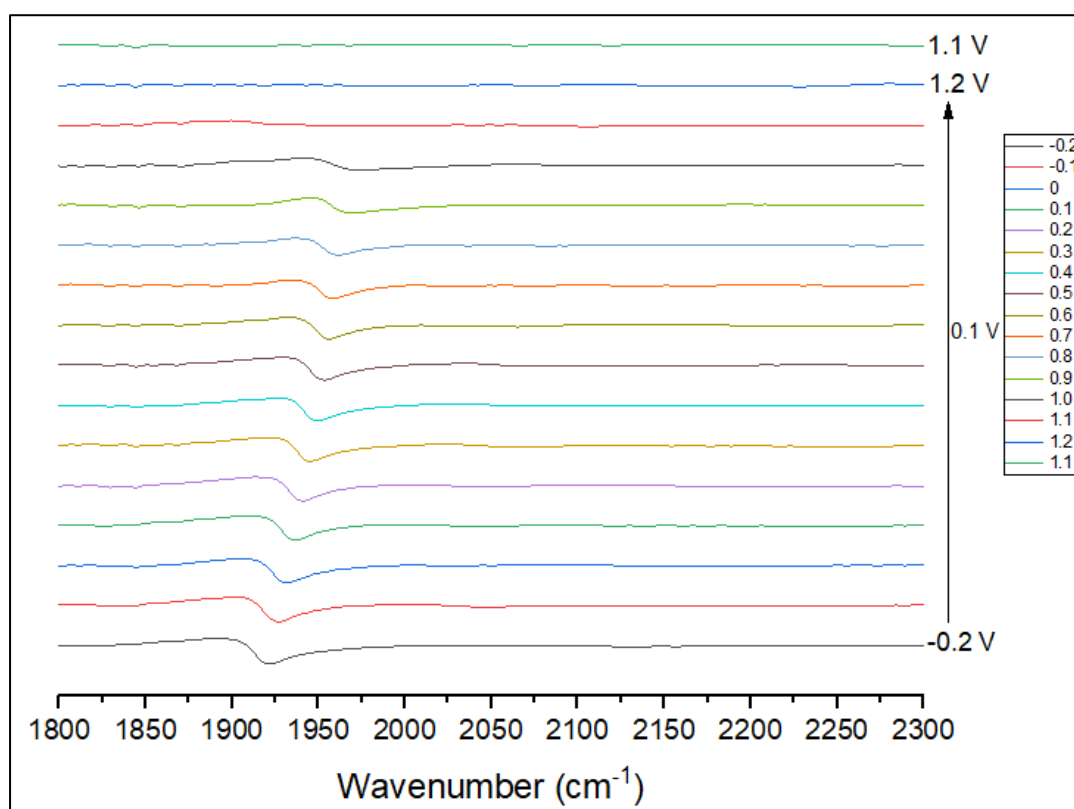
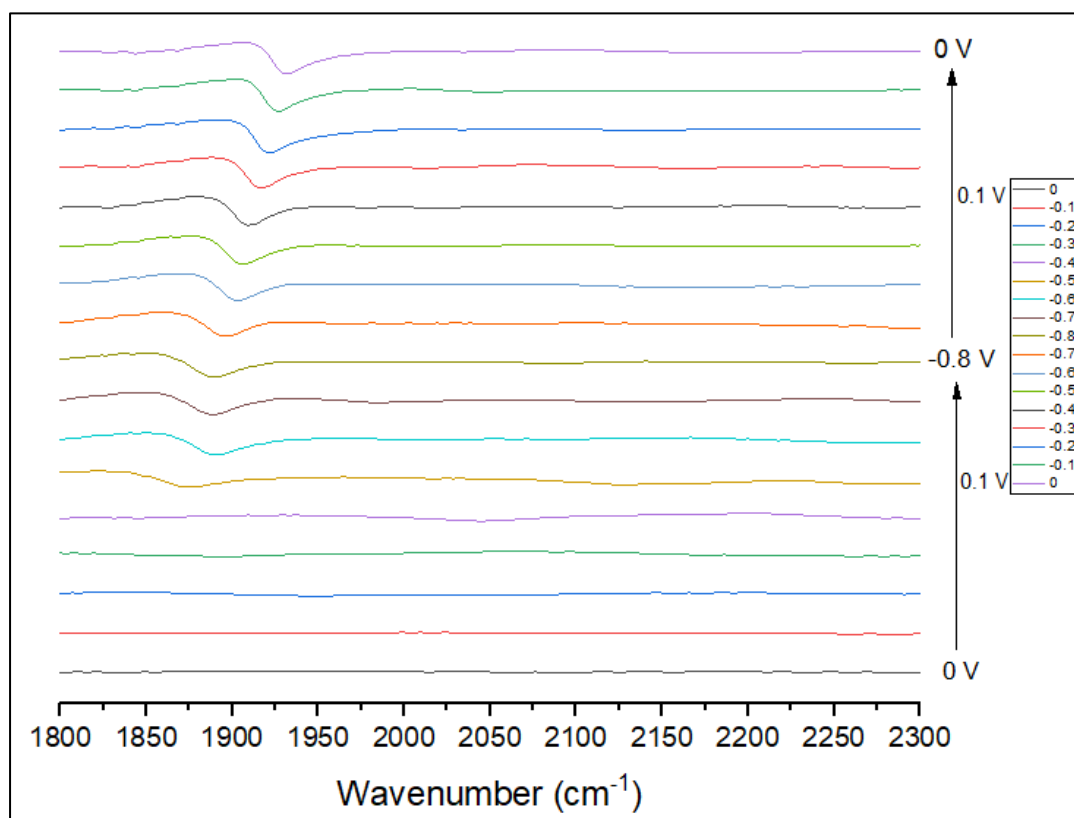
Appendix 14- The IR measurement between 1800 cm<sup>-1</sup> and 2300 cm<sup>-1</sup> observed during the CO<sub>2</sub> reduction reaction during the 10 mVpers study under the CO<sub>2</sub> saturated 0.1 M LiHCO<sub>3</sub> solution

## In-Situ Infrared Spectroscopic Studies Of Palladium Thin films during CO<sub>2</sub> Electro-Reduction



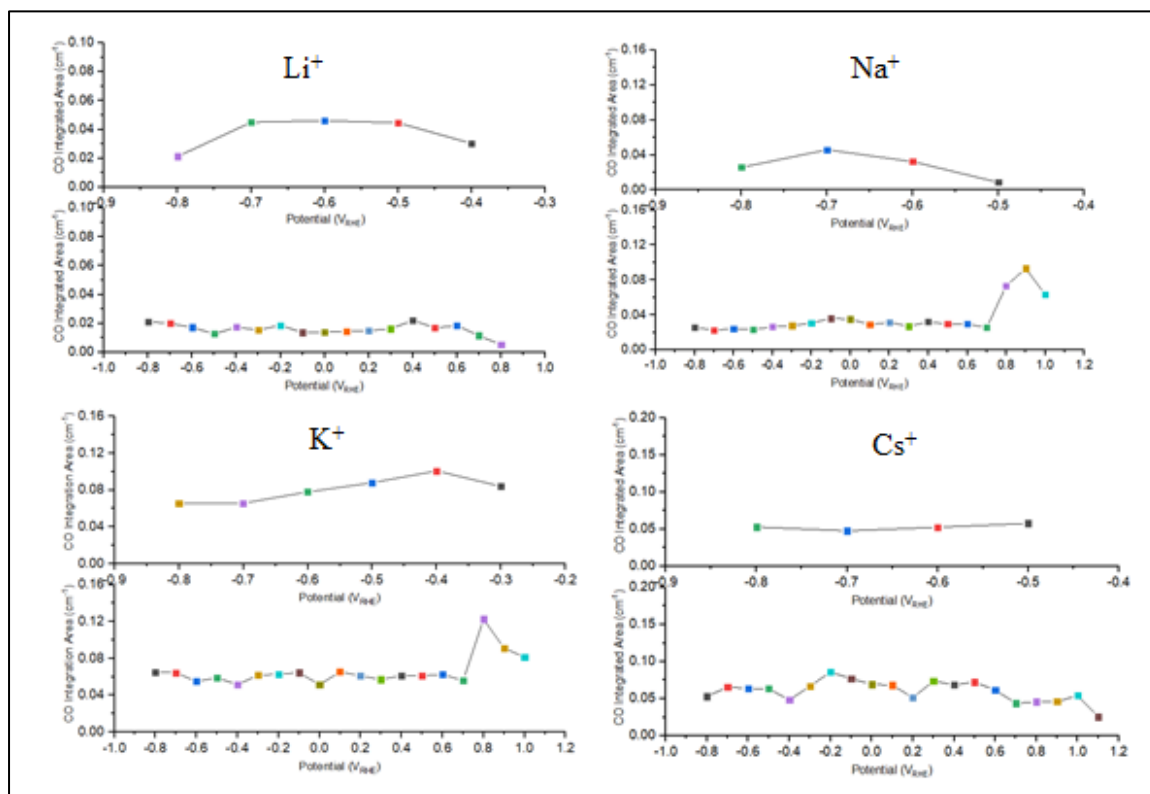
Appendix 15- The IR measurement between 1800 cm<sup>-1</sup> and 2300 cm<sup>-1</sup> observed during the CO<sub>2</sub> reduction reaction during the 10 mVpers study under the CO<sub>2</sub> saturated 0.1 M NaHCO<sub>3</sub> solution

## In-Situ Infrared Spectroscopic Studies Of Palladium Thin films during CO<sub>2</sub> Electro-Reduction



Appendix 16- The IR measurement between 1800 cm<sup>-1</sup> and 2300 cm<sup>-1</sup> observed during the CO<sub>2</sub> reduction reaction during the 10 mVpers study under the CO<sub>2</sub> saturated 0.1 M CsHCO<sub>3</sub> solution

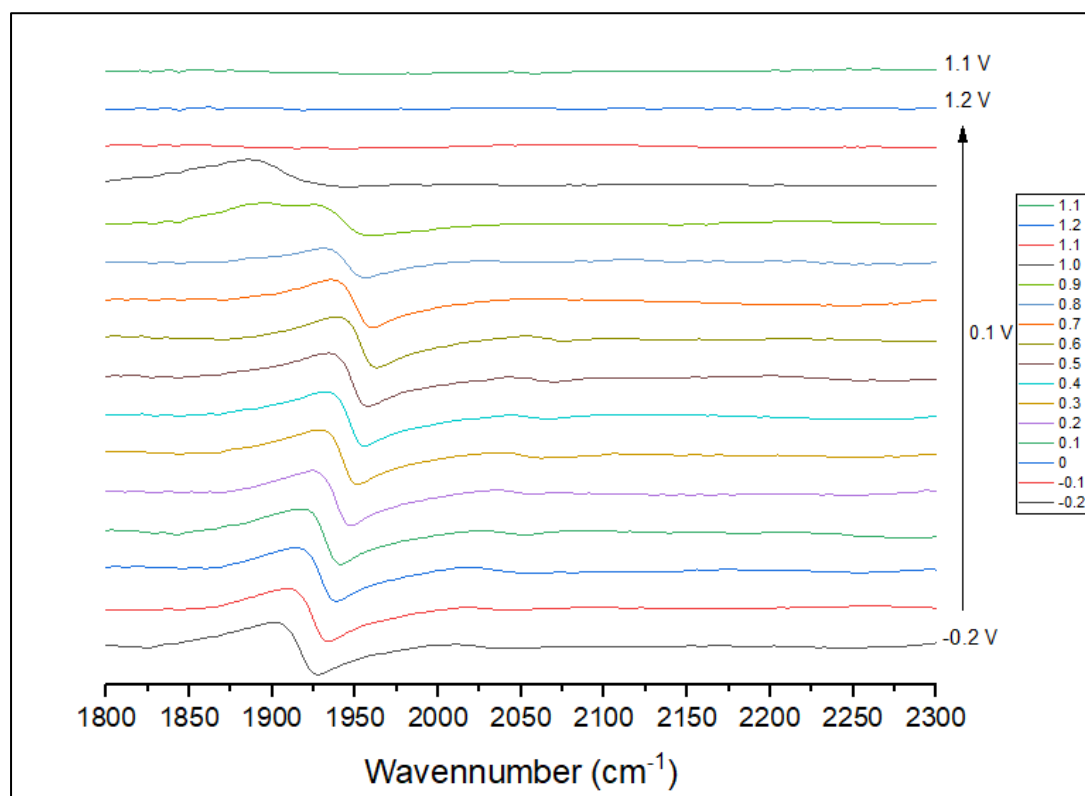
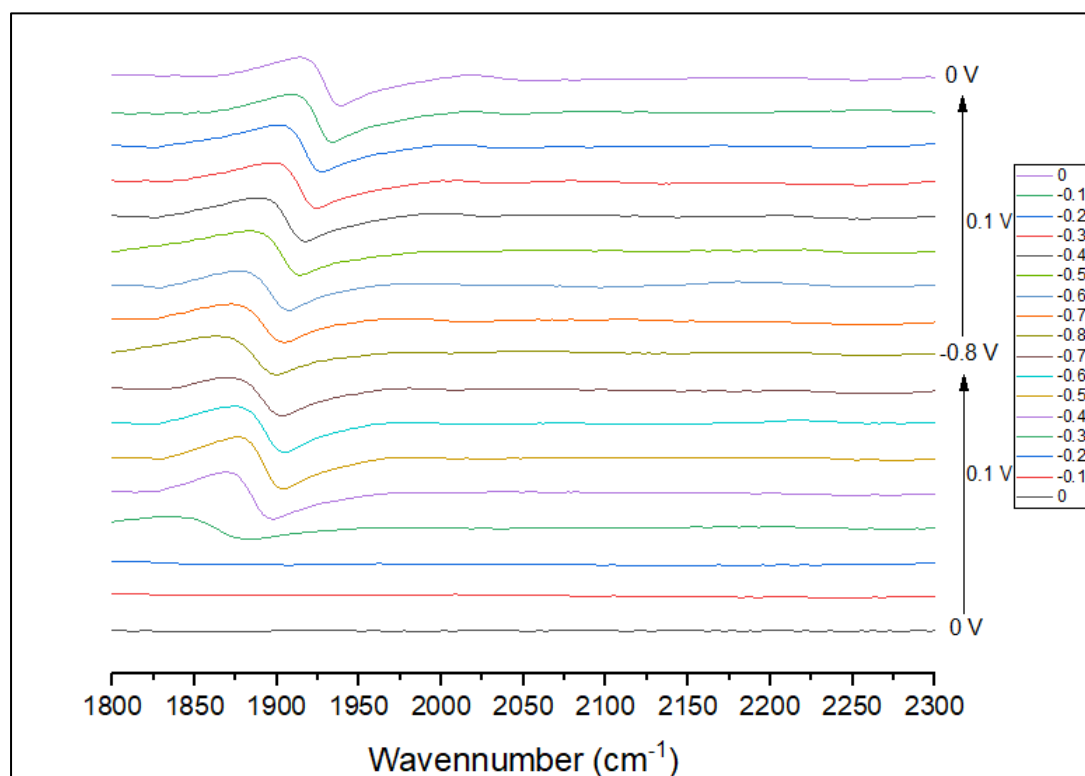
## In-Situ Infrared Spectroscopic Studies Of Palladium Thin films during CO<sub>2</sub> Electro-Reduction



Appendix 17- The area profile observed during the CO<sub>2</sub> reduction reaction during the 10 mVpers study under the CO<sub>2</sub> saturated 0.1 M Li/Na/K/CsHCO<sub>3</sub> solution

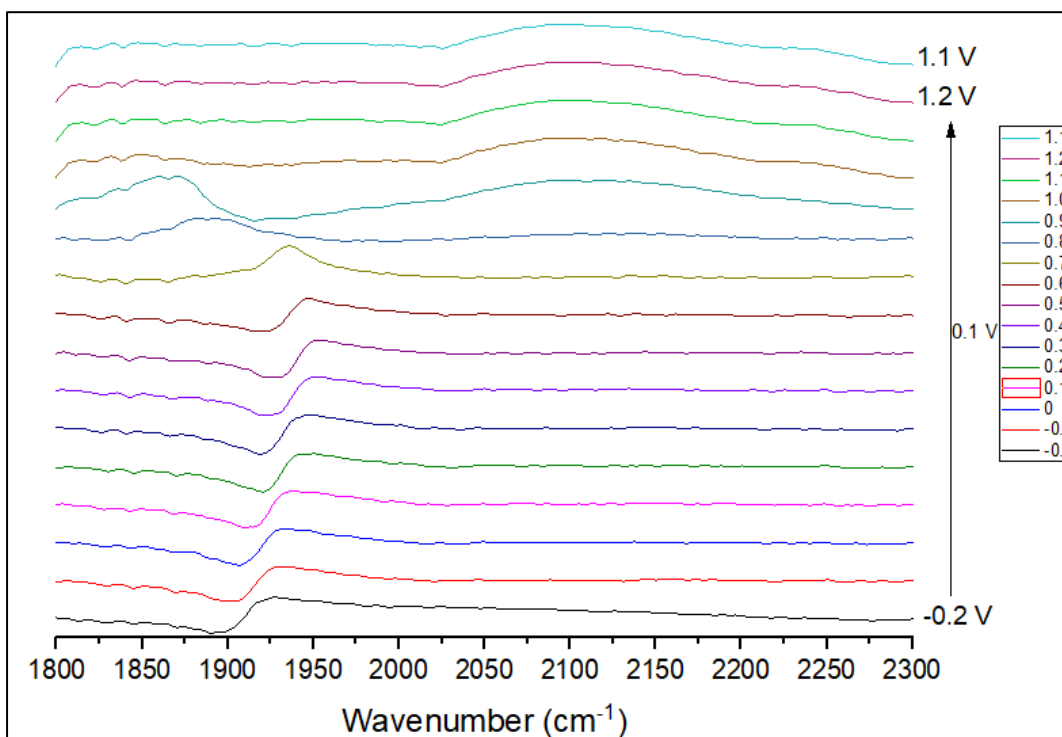
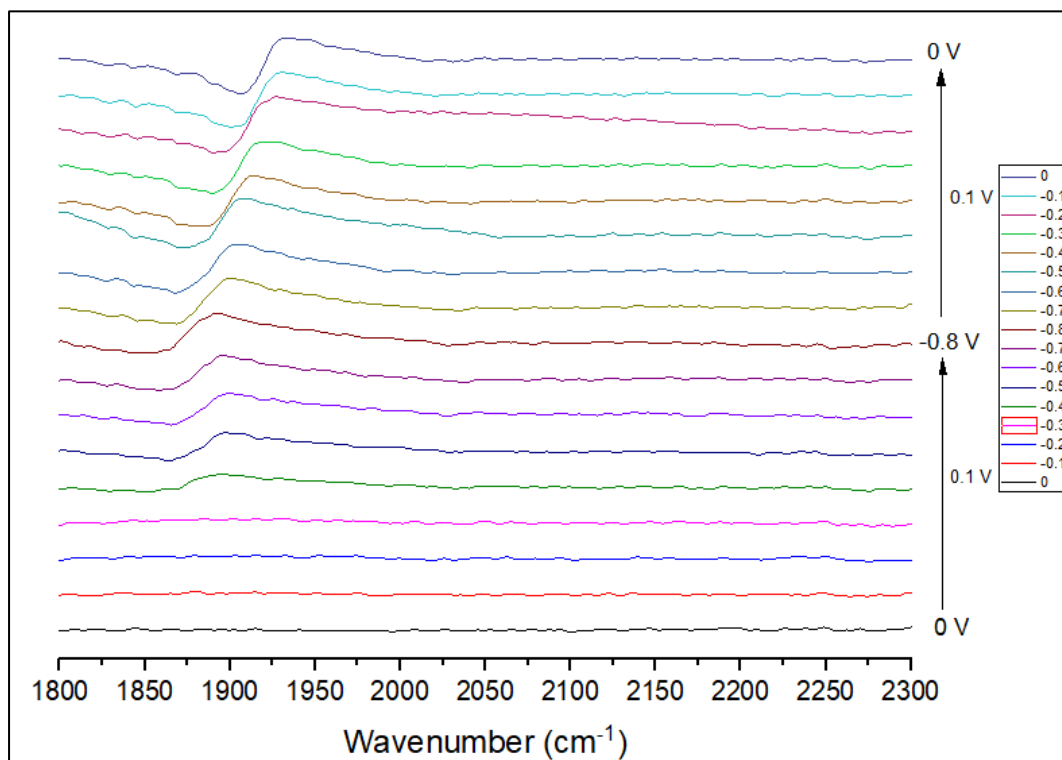


## In-Situ Infrared Spectroscopic Studies Of Palladium Thin films during CO<sub>2</sub> Electro-Reduction



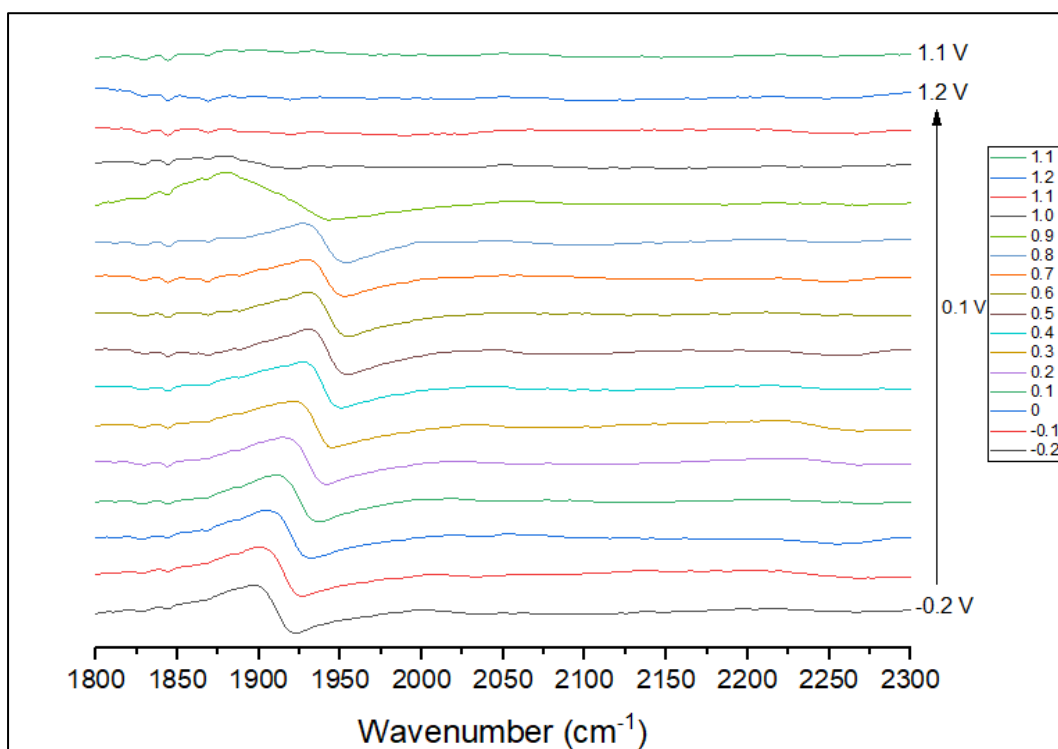
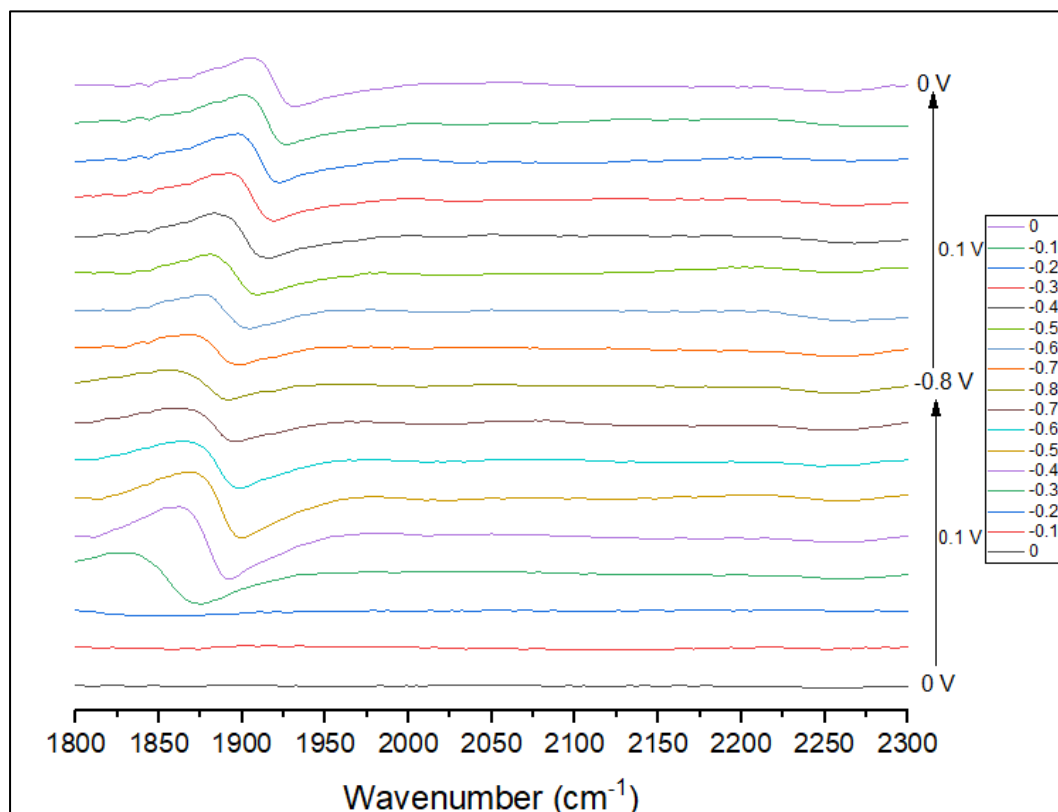
Appendix 18- The IR measurement between 1800 cm<sup>-1</sup> and 2300 cm<sup>-1</sup> observed during the CO<sub>2</sub> reduction reaction during the 2 mVpers study under the CO<sub>2</sub> saturated 0.1 M LiHCO<sub>3</sub> solution

## In-Situ Infrared Spectroscopic Studies Of Palladium Thin films during CO<sub>2</sub> Electro-Reduction



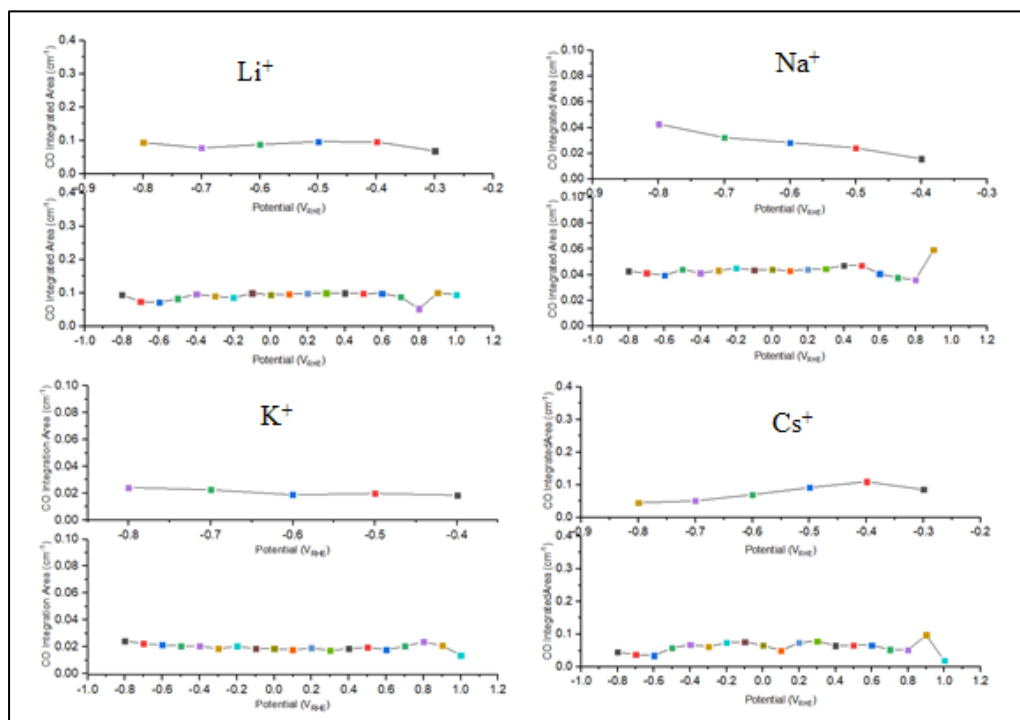
Appendix 19- The IR measurement between 1800 cm<sup>-1</sup> and 2300 cm<sup>-1</sup> observed during the CO<sub>2</sub> reduction reaction during the 2 mVpers study under the CO<sub>2</sub> saturated 0.1 M NaHCO<sub>3</sub> solution

## In-Situ Infrared Spectroscopic Studies Of Palladium Thin films during CO<sub>2</sub> Electro-Reduction

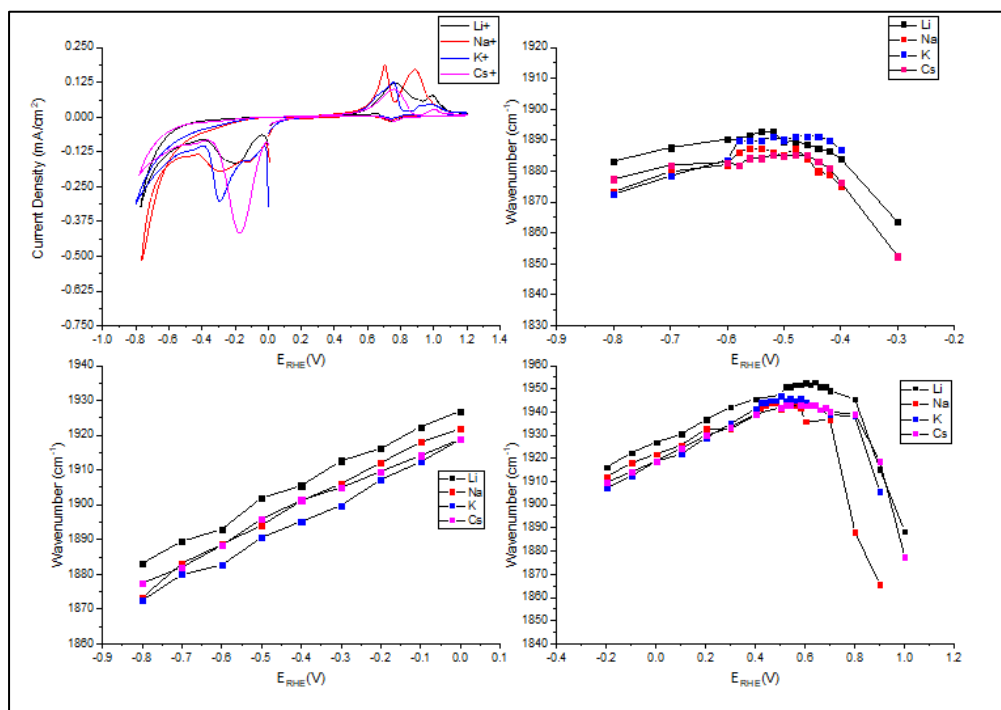


Appendix 20- The IR measurement between 1800 cm<sup>-1</sup> and 2300 cm<sup>-1</sup> observed during the CO<sub>2</sub> reduction reaction during the 10 mVpers study under the CO<sub>2</sub> saturated 0.1 M CsHCO<sub>3</sub> solution

## In-Situ Infrared Spectroscopic Studies Of Palladium Thin films during CO<sub>2</sub> Electro-Reduction



Appendix 21- The area profile observed during the CO<sub>2</sub> reduction reaction during the 2 mVpers study under the CO<sub>2</sub> saturated 0.1 M Li/Na/K/CsHCO<sub>3</sub> solution



Appendix 22- 2 mVpers CV study performed under CO<sub>2</sub> for Lithium, Sodium, Potassium and Cesium (1) Current density vs. E<sub>RHE</sub> (V), and Wavenumber (cm<sup>-1</sup>) vs. E<sub>RHE</sub> (V) between (2) -0.3/-0.4 V and -0.8 V, (3) -0.8 V and 0 V and (4) -0.2 V and 0.9/1.0 V